UNIVERSITÀ DEGLI STUDI DI NAPOLI FEDERICO II

DOTTORATO DI RICERCA
IN
INGEGNERIA CHIMICA, DEI MATERIALI E DELLA PRODUZIONE
XIX CICLO

SUPRAMOLECULAR ASSEMBLY AND MECHANICAL PROPERTIES OF DERMIS

Coordinatore
Ch.mo Prof. Nino Grizzuti

Candidato
Ing. Maurizio Ventre

Tutor
Ch.mo Prof. Paolo A. Netti

a mia nonna Carina

Contents

Preface

The present work is a part of a wider research project which aims at the in vitro tissues and biohybrid generation. The process of generating biological tissues requires benchmarks in order to define the optimal set of design and performance parameters for the tissue of interest. As a consequence of that, my efforts have been devoted to the study of natural tissue. In particular I have focused my attention to their composition, microstructure and macroscopic properties.

The first part of the thesis reviews recent studies concerning the assembly and spatial arrangement of some biological macromolecules of interest, which compose the extracellular matrix. The extracellular matrix is indeed largely responsible for the macroscopic physical properties of connective tissues.

Skin has been chosen as model of connective tissue to study. This choice is motivated by the fact that skin is a more general model rather then tendons, which are mainly subjected to uniaxal tension, and the osmosis-supported cartilage. An experimental campaign has been designed in order to gather information on dermal composition and structure, and how these characteristics can affect the macroscopic behaviour of the tissue. The results of this experimental campaign are shown in the second part of the work.

At last two constitutive equations are presented. Both of them are developed within the framework of continuum mechanics. The first one is a full three dimensional model able to capture the elastic behaviour of dermis at large deformations. The second model is able to predict the viscoelastic behaviour. Both model accounts for the anisotropy of the native tissue and are structural model, since they contain parameters on the underlying histology. The development of these models provide noteworthy information on the performance of tissue-engineered constructs whose properties have been designed *ab initio*. In particular, since the mechanical properties of biohybrids can be on-line monitored during culturing in bioreactors. Thus constitutive models can provide cues on the evolution of the mechanical properties, giving the chance to investigate on the complex relationship between mechanical stimulus and tissue remodelling.

Chapter 1

Collagen biosynthesis and assembly in the extracellular matrix

1. Introduction

In order to gain a better insight into the complex interplays between the supramolecular assembly of extracellular matrix proteins and the macroscopic mechanical response of connective tissues, it is crucial to have a clear picture of the basic mechanisms which govern, on a nano and micro scale, the biosynthetic events and the processes of molecular self-assembly. The aim of this chapter is to present the most advanced models and theories concerning the biosynthesis and assembly of the proteins of the extracellular matrix. In particular, great emphasis will be given to the superfamily of collagen proteins which are the main structural elements of connective tissues.

Usually the extracellular matrix (ECM) of connective tissues is schematized as a composite material, in which insoluble fibres are embedded in an aqueous matrix containing a wide variety of soluble macromolecules. The main characteristic of the ECM is to provide the tissue with specific physiological and biomechanical properties. These macroscopic properties are strictly related to the tissue composition and spatial arrangement of its microconstituents. Experiments performed *in vitro* have shown that several macromolecules possess themselves the "blue-prints" for the construction of the ECM building blocks. However *in vitro* self assembled structures are far from being considered functional tissues. Thus, there is growing evidence that cells play a non negligible role in modulating and controlling the ECM assembly, but the mechanisms of how cell regulates the synthesis and the turnover of various macromolecules and their accurate deposition in the extracellular environment is still poorly understood.

The most abundant proteins of the ECM of vertebrate body belong to the family of collagens. In particular, fibril forming collagens have been widely examined due to their property to form high ordered structure. Alongside collagens, some noteworthy features of elastin and proteoglycans will be presented in following sections.

2. Building molecules

The term "collagen" is generically used for those proteins forming a triple helix of three polypeptide chains. 26 genetically distinct collagen types have been described so far [1]. Collagen proteins are divided in three broad categories: fibril forming collagens (Type I, II, III, V and XI); fibril associated collagens with interrupted triple helices, or FACIT collagens (Type IX, XII, XIV, XVI); non-fibrillar collagens. Fibril forming collagens are widespread in almost all connective tissues. In particular collagen type I represents the principal fibrillar component of several tissues. Much of the discussion reported in the following, on collagen structure and biosynthesis, pertains to fibril forming collagens. It should be borne in mind that even though the general structure of other collagen types could be similar to the fibril forming collagen one, significant differences can occur in biosynthetic events and assembly.

Each of the three polypeptide chains in the molecule forms a left handed polyproline II-type helix (α-chain). Three α-chains are supercoiled about a common axis in a right-handed fashion to form the triple helix.
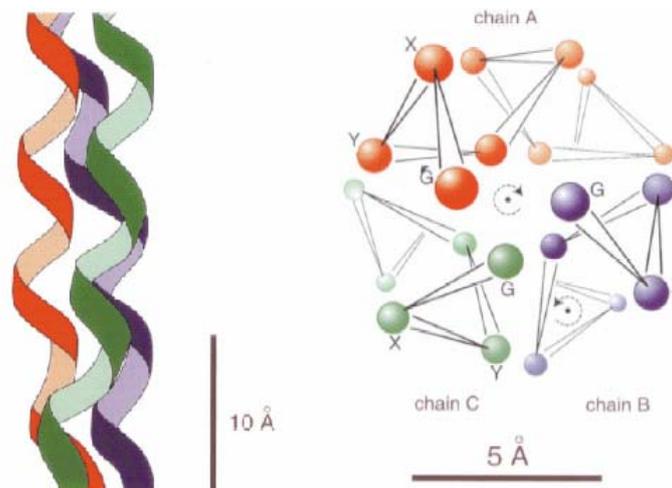
Fig. 1 Model for the structure of collagen triple helix. From Beck et al. [2]

Common feature of α-chains is the repeating sequence Gly-X-Y in the primary structure, where the X and Y position are often occupied by proline and hydroxyproline residues. α-chains wind around a common axis, in a way that the small Gly residue is positioned in the centre of the forming triple helix, while the side chains are projected outward (Fig. 1).

Collagen triple helix is a highly insoluble molecule and it is not synthesized by the cell as it is. Fibroblasts synthesize collagen in the form of its soluble precursor known as procollagen, whose structure is schematized in Fig. 2.
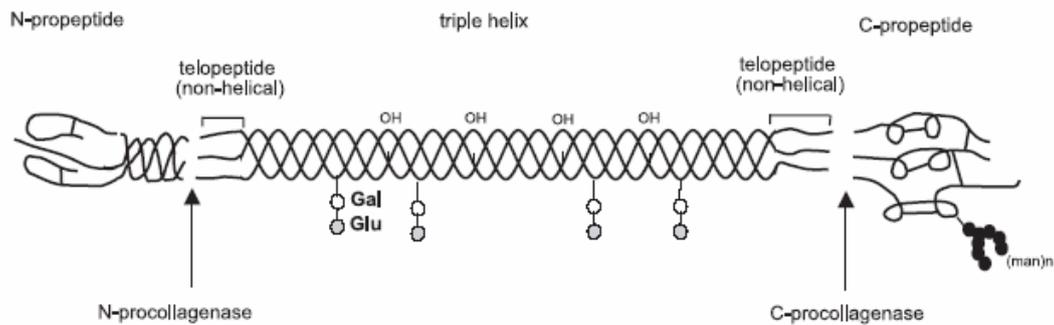
Fig. 2 Molecular structure of procollagen. From Gelse et al. [1]

Globular propeptides are attached to the central shaft via non-helical telopeptide regions. Collagen molecules can be formed by three identical chains (homotrimers, as in collagens type II, $[\alpha 1(II)]_3$, or type III, $[\alpha 1(III)]_3$) as well as two or three different chains (heterotrimers, as in type I, $[\alpha 1(I)]_2\alpha 2(I)$, or in type V, $\alpha 1(V)\,\alpha 2(V)\,\alpha 3(V)$). The formation of the triple helix occurs intacellularly in the endoplasmic reticulum (ER) and this process is assisted by molecular chaperones within the ER [3]. Newly synthesized procollagen α-chains associate into trimers via their C-propeptide. Folding process occurs from the C terminus to the N terminus following a zipper-like mechanism [4] as depicted in Fig. 3.
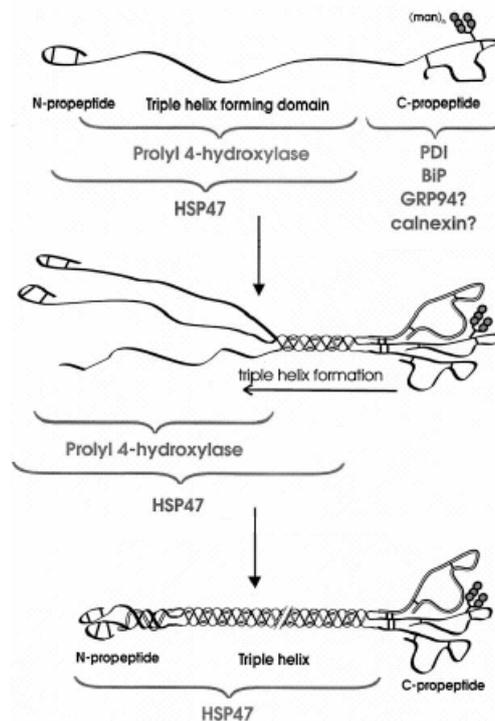
Fig. 3 Collagen triple helix formation. Molecular chaperons involved in chain folding. Based on Lamandé et al. [5]

A single fibroblast can produce several highly homologous but genetically distinct collagens. This leads to the question of how different types of collagen can be discriminated and how correct chain stoichiometry is ensured within the same ER. Lees *et al.* [6] proposed that procollagen self association is directed by a specific motif, 15 residues long, know as chain recognition sequence, which resides within the C-propeptide. The starting association between procollagen chains has been attributed to a series of non covalent interaction between C-propeptides. However it is still unclear whether the interactions which lead to the trimeric assembly are the same as those that allow chains destabilization. Lees et al. [6] have hypothesized that chain assembly occurs by default and the presence of an inappropriate chain recognition sequence matching prevents further chain folding. Structural data of C propeptide would locate the chain recognition sequence at the core of the structure, which should be a very suitable region to determine chain to chain interaction specificity (Fig. 4).
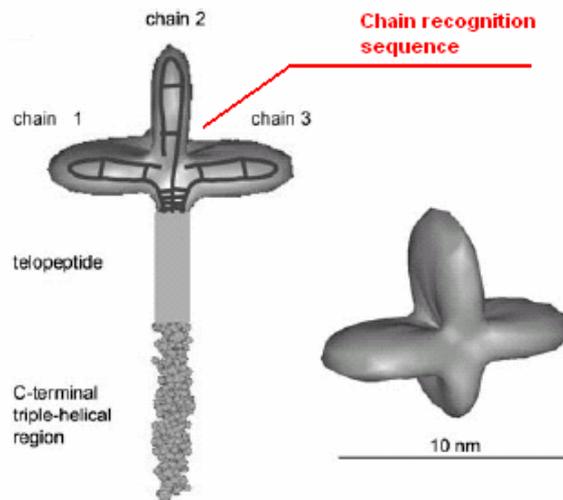
Fig. 4 3D reconstruction of procollagen III C propeptide. Based on Hulmes [7]

N propeptides have regulatory role for collagen packing and fibril formation. Telopeptides, even though they comprise 3% of the whole molecule, strongly affect collagen fibrillogenesis. The functions of both N propeptides and telopeptides will be explained in more details in the next section.

Procollagen chains undergo several post translational modifications. 50% of proline residues are hydroxylated, either in position 3 but more often in position 4, by two different enzymes prolyl 3-hydroxylase and prolyl 4-hydroxylase respectively. The presence of 4-hydroxyproline residues is essential for the stabilization of the triple helix [8]. Lysine is hydroxylated too, even if the extent of hydroxylation varies widely among different tissues. Hydroxylysine residues constitute the basis for the formation of intermolecular crosslinks [9]. Carbohydrates can be attached to specific hydroxylysine residues on individual procollagen chains. In particular, two enzymes catalyse the formation of hydroxylysine-linked carbohydrate groups on procollagen molecules. Hydroxylysil-galctosyltransferase catalyses the addition of galactose to hydroxylysine residues, while galctosylhydroxylysyl glucosyltransferase catalyses the addition of glucose to some galactosylhydroxylysine residues. Carbohydrates could be present in the form of monosaccharide galactose or disaccharide glucosylgalactose. The biochemical and biophysical functions of such carbohydrates on the triple helix surface are not thoroughly understood. Probably they may influence lateral packing of collagen molecules [10]. It is important to underline that once the chains are wound in the triple helix, no further post translational modification can occur, i.e. the available site for the enzymes are hindered. Thus all the above mentioned reactions occur *in vivo* on nascent chains [10 and references therein].

3. Building fibrils

Collagen fibril is the key structural element of connective tissues. It has a high tensile strength, especially in adult tissues, and it is flexible. Collagen fibrils can vary in composition and shape, depending on the tissue where they come from. However they are present in *all* connective tissues. Fibril inner structure is composed of an ordered array of collagen molecules. The process that leads to the formation of a fibril starting from collagen molecules is know as *fibrillogenesis*. It is an entropy driven process, owing to the loss of water molecules bound to the monomer as the polymerization occurs [11].

As stated in the previous section, fibrillar collagens are synthesized as soluble precursors, the procollagens. Amino and carboxyl propeptides are enzymatically cleaved by specific propeptide metalloproteinases. Without these enzymes, collagen fibrillogenesis would not occur. In particular, as long as the C-propeptide is attached to the molecule, collagen solubility remains high. Thus it is presumable that C-propeptide retention prevents fibril formation. N-propeptide retention, on the other hand, allows fibrillogenesis to occur. However, it strongly affect collagen lateral packing.

Electron micrographs of native collagen fibrils exhibit a characteristic banded pattern with a 64 nm period (also known as D-period) (Fig. 5).
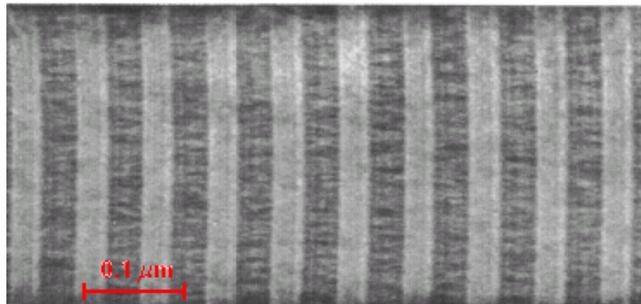

Fig. 5 Rat tail collagen fibril. Based on Cox et al. [12]

Since collagen molecule is approximately 300 nm long, it is clear that monomeric units are displaced longitudinally relative to one another by ¼ of the macromolecular length [13] as schematized in (Fig. 6).
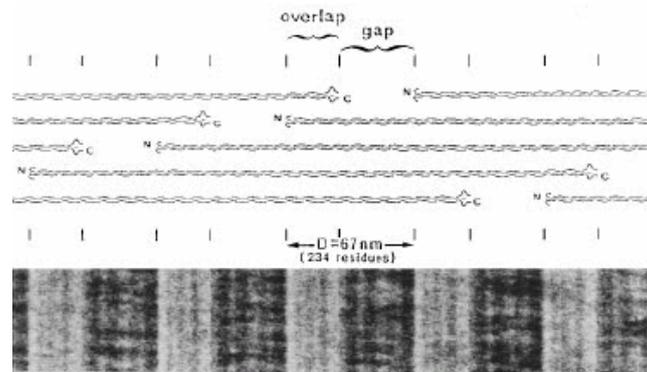
Fig. 6 Schematic representation of the packing arrangement of collagen molecules in a fibril. Based on [14].

Collagen fibrils are constituted by alternating *overlap* and *gap* zones staggered each other by 40 nm. The latter zone uptakes electron dense staining resulting in a dark band on the micrograph.

The quarter staggered structure is stabilized by intermolecular enzymatic crosslinks. Covalent crosslinking avoids the molecules to slip each other under mechanical stress, thus providing collagen fibrils with mechanical strength. When collagen molecules are aligned in the quarter staggered arrangement, the enzyme lysil oxydase can bind to the specific sequence Hyl-Gly-His-Arg in the triple helix. Once bound to the sequence, the enzyme oxidatively deaminates lysines in the N and C terminal telopeptides of adjacent molecules producing reactive lysine-aldheydes. Crosslinks then spontaneously form between the lysine-aldheyde and the hydroxylysine in the enzyme binding sequence. The nature of the crosslinks strictly depends on the extent of hydroxylation of the lysines in telopeptide region. As an example in immature skin the lysine is not significantly hydroxylated. The major crosslink is the dehydro-hydroxylysinonorleucine (deH-HLNL). Telopeptide lysines of cartilage and bone are in turn highly hydroxylated thus leading to the formation of dehydro-dihydroxylysinonorleucine (deH-DHLNL), which almost instantly transforms in hydroxylysino-keto-norleucine (HLKNL). Such divalent crosslinks decrease as the tissue matures, by spontaneous reaction with additional groups. The ability of divalent crosslinks to react further creating multivalent crosslinks relies on the groups of adjacent molecules being in register rather than quarter staggered (bonding between microfibrils). Several mature enzymatic crosslinks have been characterized so far. For detailed reviews of collagen intermolecular crosslinks the reader is referred to the excellent works of Bailey and colleagues [15, 16]. Another non enzymatic crosslinking mechanism accounts for fibril stabilization. This mechanism, known as glycation, involves the addition of glucose on the collagen triple helix. These glucose adducts can react further to form

7

crosslinks via complex oxidative reactions. This mechanism occurs predominantly in aged tissues and in pathological conditions [17].

Several in vitro models were developed in the past decades to study collagen fibril formation. It was indeed recognized that studying the fibrillogenesis *in vitro* could have provided some insights into the mechanisms which occur *in vivo*. Collagen fibrils can be reconstituted *in vitro* starting from enzyme treated procollagen solution [18], salt-extracted collagen [19] or acid-extracted collagen [20]. The first model is a cell-free system in which procollagen is sequentially cleaved with procollagen metalloproteinases The fibrils generated with this system display initially tapered tip and a blunt end. Fibril growth occurs first on the pointed tip. As the propagation carries on, the blunt end becomes tapered which allows the growth in the opposite direction. Another characteristic is that the two tips have all collagen molecules oriented in the same direction, in particular N termini are outward facing. These fibrils are usually named N-N bipolar. Closer inspection of bipolar fibrils reveals a switch region in which the molecules are arranged in an antiparallel fashion (Fig. 7).
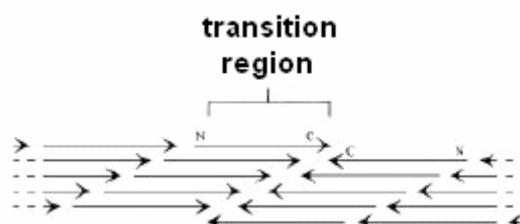
Fig. 7 Schematic of the transition region in N-N bipolar fibrils. Based on Kadler et al. [14].

It is possible to extract collagen from several tissues (tendons, ligaments, skin) into neutral salt or acidic solutions. Collagen is usually collected in the form of monomer, but it is possible to find in smaller quantities crosslinked dimmers, trimers and higher components. Acid soluble collagen can be precipitated under suitable condition (ph, temperature and ionic strength) producing D-periodic N-C unipolar fibrils. However, in the case of high collagen concentration (few mg / ml), the final outcome is a meshwork of very long fibrils in which ends are not observed. Usually the yield of an acid extraction is poor. In order to overcome this limitation, pepsin is involved during the extraction. This enzyme cleaves the non-helical telopeptides, which are the preferred loci for collagen crosslinking. Complete removal of both N and C telopeptides leads to the genesis of non banded fibrous aggregates.

Some noteworthy results concerning collagen fibrillogenesis *in vitro* have been shown so far. However reconstituted collagen fibrils display several morphological differences respect to the native fibrils. As an example, fibrils formed from acid soluble collagen are not cylindrical and posses a broad distribution of dimensions. This suggests that other molecules can participate during the process and cells can exert regulatory effect over fibrillogensis. Both *in vitro* reconstituted and native extracted fibrils can be either C-N unipolar on N-N bipolar. There is no experimental evidence of the existence of neither C-C bipolar fibrils nor multiple switch regions within the same fibril [14]. The Axial Mass Distribution (AMD) profiles of embryonic fibrils suggest that tip to tip fusion occurs *in vivo* and at least a C terminal is involved in fibril fusion [21]. Moreover native fibrils can be grouped into three different categories according to their AMD pattern. Thus Primary (P)-type fibrils are short fibrils (< 40 D-periods) with virtually no constant diameter central shaft, i.e. formed by just two adjacent tips. Limited Diameter (LD)-type fibrils present a longer constant diameter central shaft between two pointed tips. Fused Intermediate (FI)-type fibrils display one or, occasionally, more thinned regions (throats) in the central shaft, which suggest FI-type fibrils are the result of tip to tip fusion between two or more smaller fibril [21]. These results suggest that C-N unipolar fibrils can fuse C-tip N-tip giving a longer fibril, or side by side (provided that they are in axial register) giving a thicker fibril. Side by side fusion of two oppositely directed fibril has never been observed experimentally. Probably these constraints on fibril axial and lateral fusion is indicative of a self-controlling mechanism of both fibril length and diameter. In a mixed population of unipolar and bipolar fibrils, as the tip to tip fusion events occur, the fraction of bipolar increases, whose fibrils cannot fuse further [14] (see Fig. 8).
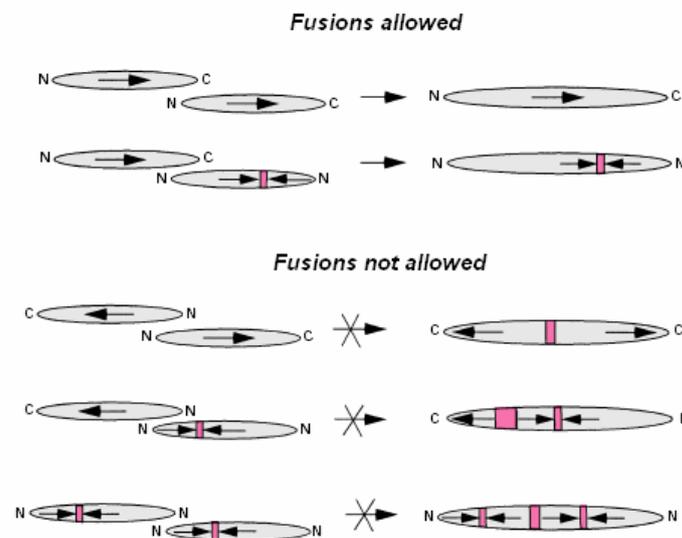

Fig. 8 Models of fibril fusion. Based on Kadler *et al.* [14]

Fibril polarity however is not the only mechanism which regulates and control lateral and axial assembly. It is indeed well recognized that other macromolecules and collagen intermediates (partially processed procollagens) can participate in collagen fibrillogenesis affecting both axial and lateral packing. Native collagen fibrils are heterotypic in nature, thus involving different type of collagen and collagen intermediates. As an example dermal collagen fibrils are hybrids of type I and III [22], thus dermal fibroblasts coexpress both type I and III collagen. Normally cleavage of type I N-propeptide is faster than type III N-propeptide. Delayed N-terminal processing leads to the stacking of partially processed procollagen, named pN-collagen (i.e. which retains N-propeptide). Immunolocalization experiments, performed on foetal skin, revealed that the larger fibrils were coated with type III pN-collagen but not type I pN-collagen [23]. These data suggest that probably large type III aminopropeptides could regulate fibril diameter by steric hindrance.

In order to understand the role of collagen intermediates in fibrillogenesis, it is here presented one of the most acknowledged model concerning collagen fibril structure, proposed by Hulmes *et al.* [24]. A key feature of this model is that it is in agreement with both X-ray diffraction data and electron microscope images. In particular, the model predicts the liquid-like disordered regions which are evident from x-ray diffraction patterns, admixed with three dimensional radial cristallinity.
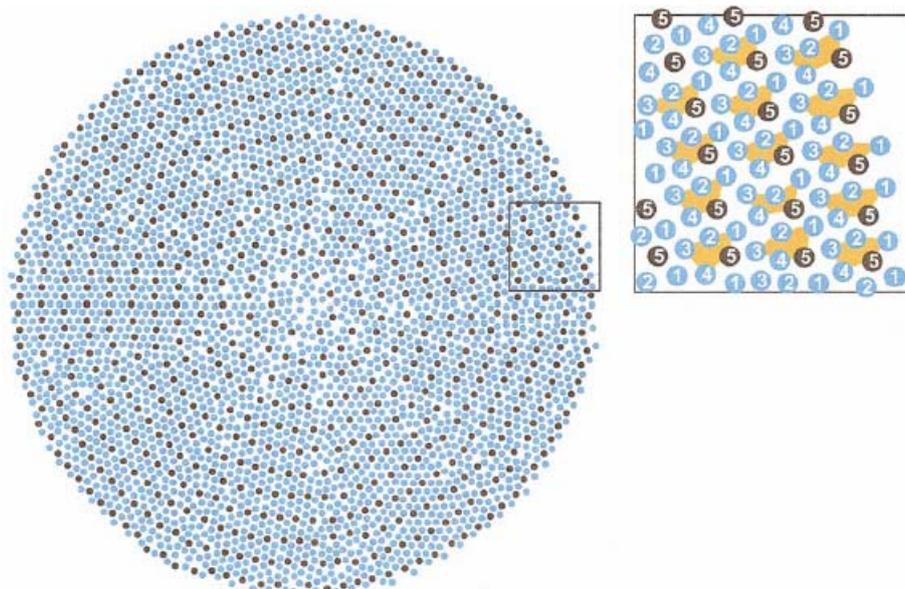

Fig. 9 Molecular packing in collagen fibril. Based on Hulmes [7]

Each molecule is divided in 5 segments (depicted with numbers 1 to 5 in the insert of Fig. 9). Molecular segments occupying the same axial position possess the same number

and are placed in concentric layers. Individual collagen molecule are arranged in a quasi-hexagonal packing (see insert of Fig. 9). Consecutive molecular segments are staggered by 1D period. Five molecules are grouped together in the form of *microfibrils* which wound in a left handed helix. This is consistent with the five strand model developed by Smith [25]. Another very intriguing feature is that the fibril surface is coated with molecular ends (segments 1; insert of Fig. 9). This particular prediction of the model could explain the effect of propeptide retention for fibril growth. For example, bulky propeptides, as the non cleaved type III N-propeptide or the partial processed type V and type XI N-propeptide, are forced outwards, hampering further incorporation of molecules on the fibril surface and then limiting diameter accretion. The stacking and subsequent cleavage of the N-propeptides could in part explain the almost discrete distribution of fibril diameters, i.e. mature tissues display fibrils with multimodal distribution of diameters with peaks at multiples of 11 nm. These predictions have been confirmed by *in vivo* observations [26], and seem to be the predominant mechanism controlling fibril assembly for corneal collagen. Birk and co-workers [26] proposed a simple model for the regulation of fibril growth, which is reported in Fig. 10.
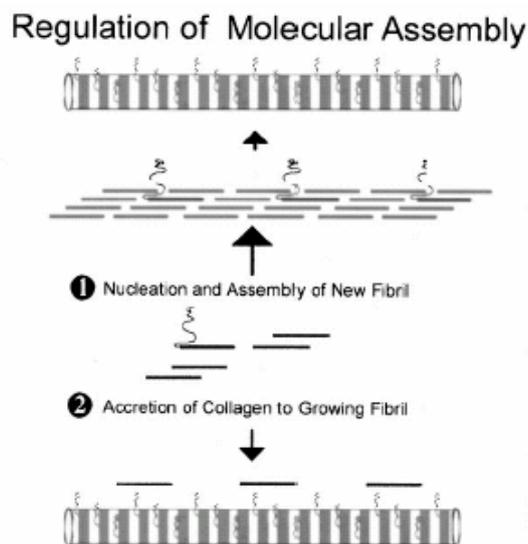
Fig. 10 Model for the heterotypic regulation in collagen fibrillogenesis. Based on Birk [26].

As soon as the type V amino terminals concentration reaches a *critical* level, the incorporation of new collagen molecules on the surface is less favoured (process 2 in Fig. 10) rather than the nucleation of new fibril (process 1 in Fig. 10). The hampering effect could be ascribed to steric hindrance, electrostatic repulsion via the presence of sulphate groups on tyrosines which are present in type V amino terminals, or by interaction with

other highly charged macromolecules such as small leucine-rich repeat proteoglycans (SLRPs). *In vitro* experiments seem to confirm the prediction of the model. Native collagen fibrils have the ability to fuse laterally, producing larger aggregates, provided that fibril-associated proteoglycans are digested [21, 27].
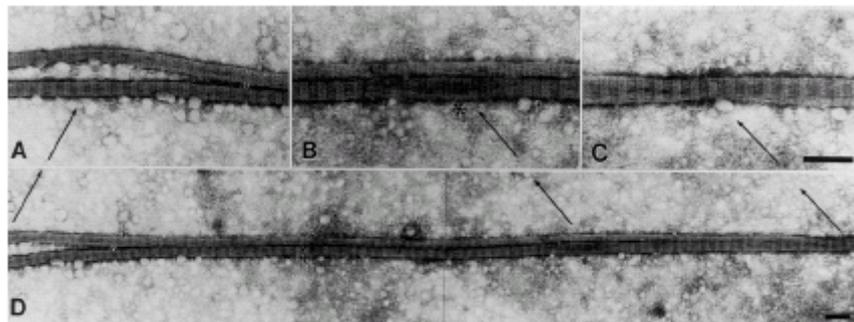
Fig. 11 Fibril fusion in the absence of fibril associated proteoglycans. Note the insert C. From Birk [26].

Graham and co-workers [21], have observed that proteoglycan concentration is not constant throughout fibril length. Proteoglycans are preferentially localised to the fibril central shaft, which would favour tip to tip fusion rather lateral aggregation. These results suggest that fibril-associated protoglycans form complexes with collagen prior fibril assembly rather than proteoglycans binding to an existing collagen fibril. Lateral fluidity of uncrosslinked fibrils allows the proteoglycans to remain on the surface during lateral growth, up to a critic concentration. Beyond this level, lateral fusion is prevented yet allowing tip to tip fusion (Fig. 12).
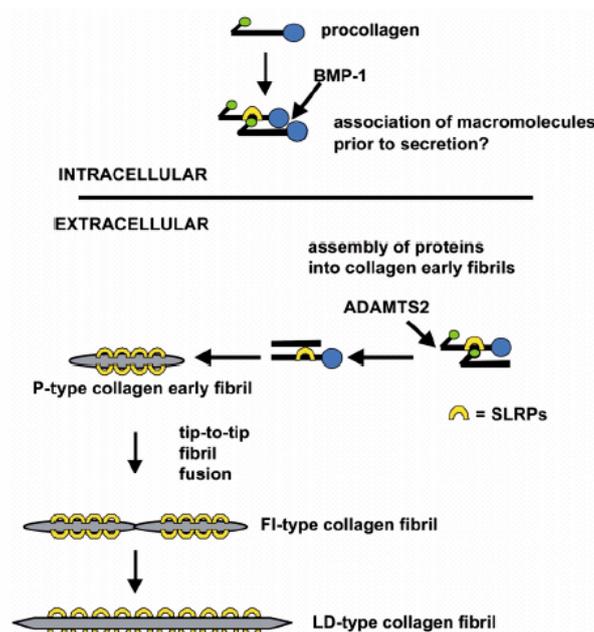

Fig. 12 Schematic representation of fibril assembly. From Canty et al. [29]

Other macromolecules which can affect fibril lateral assembly are the so called "Fibril-Associated Collagen with Interrupted Triple helices" (FACIT). This family of collagens consists of multiple collagenous domains separated by non-collagenous regions. Type XII and type XIV are probably the most characterized FACITs. They are colocalized with type I rich tissues, even though they are not chemically bound to type I collagen nor to each other. Their mechanism in regulating fibril assembly seems to be similar to that accomplished by SLRPs.

The existence of microfibrils within a fibril, however, is still a subject to debate [28 and references therein]. The development of new electron microscopy techniques seems to steer the debate towards the confirmation of the microfibrillar nature of collagen fibrils. Holmes and co-workers [30], using automated electron tomography were able to reconstruct the three dimensional structure of corneal collagen fibrils. The reconstruction showed microfibrils within the fibril, 4 nm wide and tilted approximately by 15° to the fibril axis. Moreover, the tilt angle is constant and irrespective of the microfibril radial position. These results suggest that microfibrils are arranged in coaxial layers.
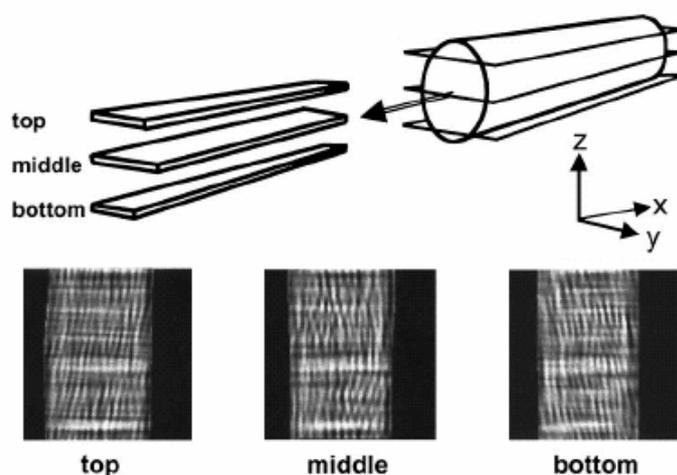
Fig. 13 Three dimensional reconstruction of a corneal collagen fibril. Modified from Holmes et al. [30].

Microfibrils seem to be wound in right handed helix around the fibril axis. Interestingly, this right handed pattern is the final step in alternating handedness in the hierarchy of structures which form the fibril: 1. left-handed polypeptide α-chain; 2. right handed coiled collagen triple helix; 3. left handed collagen molecules arrangement within the microfibril; 4. right handed microfibril helix around the fibril axis.

The helical pattern of collagen fibrils surface, has been widely documented using several ultrastructural techniques. Ottani *et al.* [28], noticed that collagen fibrils extracted from various tissues invariably showed one of two morphological aspects: 1. winding angle < 5° and plurimodal diameter distribution; 2. winding angle ~17° (value consistent with the one found by Holmes *et al.* [30]) uniform diameter distribution, variable from tissue to tissue, but locally consistent. In particular, fibrils of the first category, named T-type fibrils, come from load bearing tissues, such as tendons and ligaments. Fibrils of the latter class belong to looser and highly hydrated tissues like cornea, skin and nerves. For these fibrils the term C-type has been proposed. An exception to these broad categories is represented by cartilage fibrils. Cartilage, indeed, has a very peculiar structure, with very thin fibrils entrapped in a proteoglycan rich hydrated matrix. This fibrils however do not show any helical pattern.

4. Building tissues

Few basic mechanisms have been reported so far, which are believed can regulate collagen self assembly and fibril growth. Collagen spatial arrangement is certainly affected by copolymerization of different collagen types as well as different noncollagenous macromolecules, procollagen processing and fibril polarity. However these mechanisms are not the only responsible for the supramolecular organization of fibrils, which is of paramount importance in tissue construction. As an example it is not possible to reconstitute *in vitro* collagen gels at concentrations above 6-7 mg / ml, which is a value far below the collagen concentration found *in vivo*. These gels are formed by a continuous meshwork of thin fibrils with no supramolecular organization whatsoever. This clearly suggests that cells have a central role in regulating collagen fibrillogenesis and fibril assembly. However cells alone are not able to produce structures which resemble those found in vivo. Fibroblasts in culture do synthesize collagen, but this collagen is not assembled correctly. In conclusion, the homeostasis functional tissue seems to be maintained by a complex interplay between cells and extracellular matrix: cells synthesize and participate in the ECM assembly; the ECM, in turn, possesses information for the self assembly and exerts a regulatory role in promoting or maintaining cellular differentiation, owing to its specific composition [10].

One of the most intriguing problems of the Structural Biology concerns the understanding of the mechanisms involved during the morphogenesis and development of tissues. Several works in literature, besides obvious differences in methodology, have in common the study of embryonic tissues. It is indeed during the embryonic stages that the structure of the tissues develops and settles. Numerous models of collagen-rich embryonic tissues have been studied, as an example cornea [31], dermis [32], but mostly tendons [33, 34, 35], owing to their simple inner structure composed of parallel bundles of collagen fibres. Canty and colleagues showed [36] novel and interesting features of the morphogenesis of developing embryonic tendons. In the early stage of development (up to 13 days) tendons appear to be densely populated by apparently undifferentiated cells, with smooth and flat cytoplasmic membrane (Fig. 14A). Hollow channels among embryo fibroblasts frequently appear, which is an observation consistent with the results of Ploetz *et al.* [32]. At day 14 numerous collagen fibrils, suddenly become evident in the extracytoplasmic compartments (Fig. 14B).
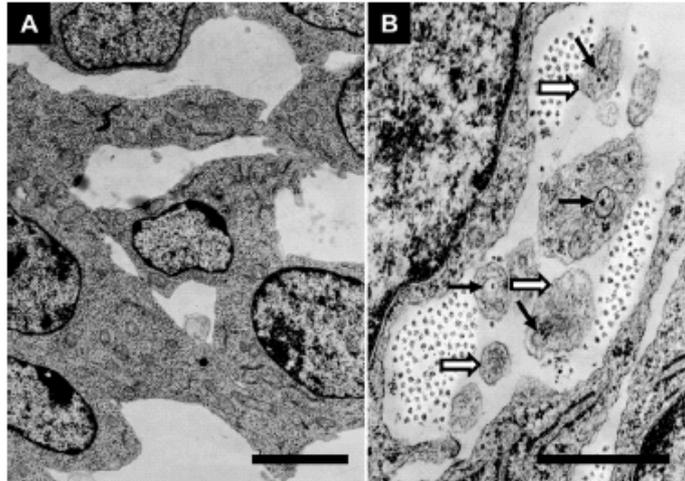
Fig. 14 Extracytoplasmic channels and fibril deposition in the early development of rat tail tendon. From Canty *et al.* [36].

Moreover, cell surface is more convoluted and cell projections extend out into the extracellular space (open arrow in Fig. 14B). Cylindrical vacuoles containing collagen fibrils are clearly visible (solid arrow in Fig. 14B). Serial section reconstruction, from longitudinal sections, revealed a very peculiar structure of these projections as schematically depicted in Fig. 15 (insert D).
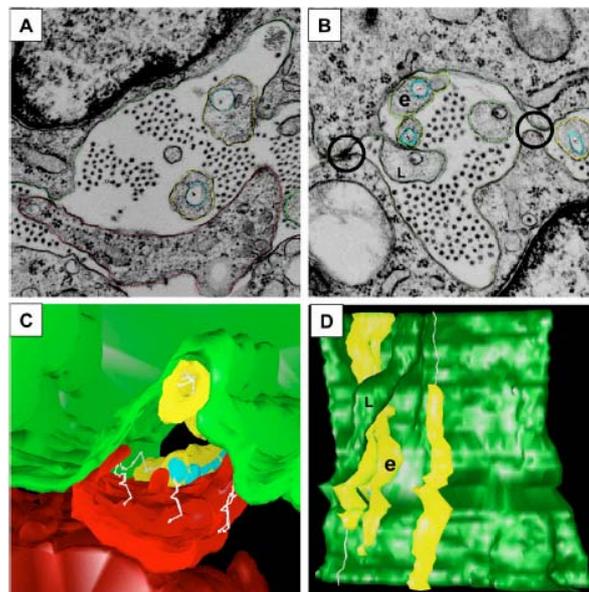
Fig. 15 Three dimensional reconstruction of membrane protrusions within extracellular compartments. From Canty et al. [36].

These images clearly show that fibroblasts are roughly cylindrical in shape, with their long axis parallel to tendon axis which is a very different morphology from the one observed in *in vitro* cultured embryo fibroblasts. Plasma membrane is convoluted and its

recesses form channels (compartments) with adjacent fibroblasts which are parallel to the tendon axis. These channels seems to be stabilized by specific points of contact between adjacent cells. This probably suggests the involvement of transmembrane receptors in the genesis of intercellular compartmens. The membrane protrusions run parallel to and within recesses of the plasma membrane. These projection are named *fibripositor* (fibril depositor) since they actually act as fibril deliver into the ECM, as reported in the following figure.
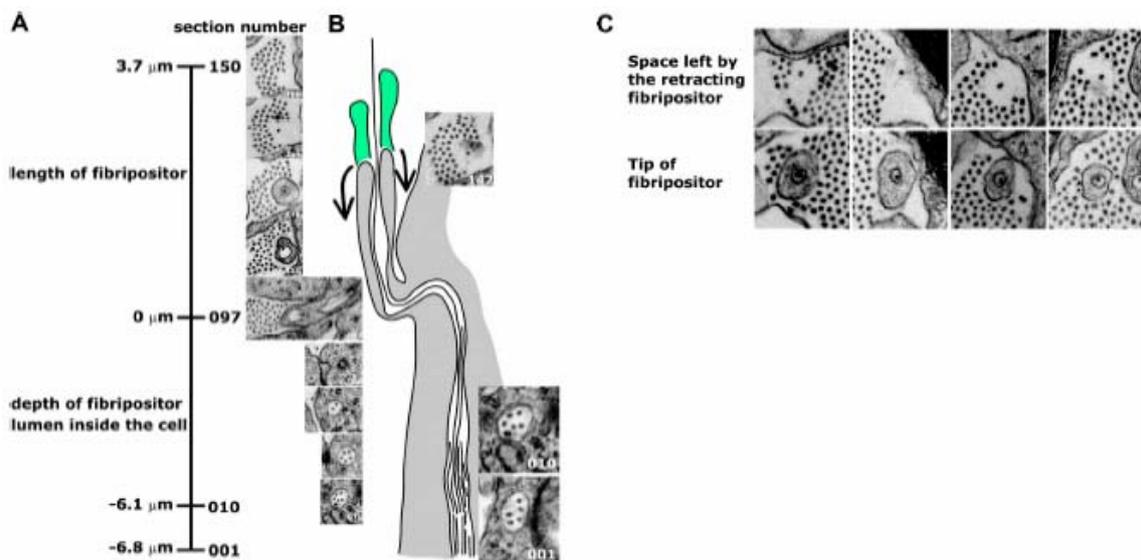
Fig. 16 Schematic showing the transverse reconstruction of a fibripositor. From Canty et al [36].

As it is shown in Fig. 16, collagen fibril extends from the fibril bundle, to deep within the cytoplasm. At the site of fibripositor-cell junction a S-shaped kink appears. Fibrils within the fibripositor and within the cell are parallel to the tendon axis. Several short collagen fibril whiskers are frequently present at the base of the fibripositor lumen. The mechanism of delivery is by retraction of the fibripositor tip, as depicted in the insert C in Fig. 16. Fibrils in the ECM seem to follow an hexagonal arrangement as depicted in detail in the following Fig. 17.
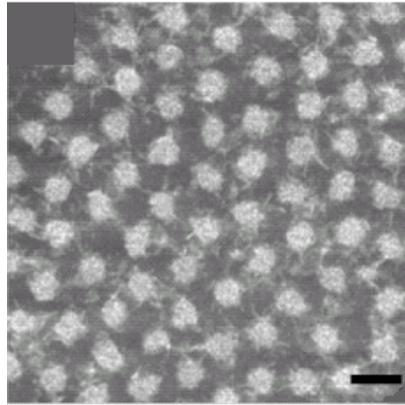
Fig. 17 Electron micrograph of a portion of tendon fibril bundle. Note the uniformity of diameter. Bar 50 nm. Modified from Canty et al. [36].

Moreover, interfibrillar matter seems to interconnect individual fibrils. This sort of connections among fibres has been reported also by Zhang *et al.* [37]. They suggest that fibril branching as well as interfibrillar matrix interaction would cause the connective structure to be mechanically stabilized.

These results lead Canty and coworkers to develop a novel model for the tendon morphogenesis process, reported in Fig. 18.
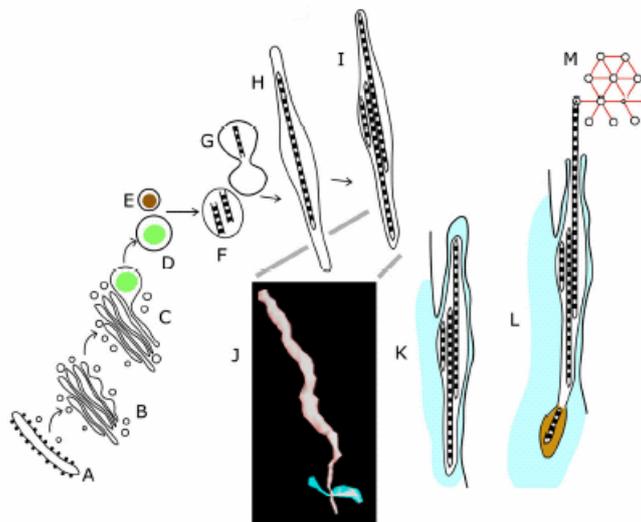
Fig. 18 Model of fibril delivery. Modified from Canty et al. [36].

Golgi vacuoles containing procollagen, fuse with vacuoles containing procollagen peptidases. The fibrillogenesis occurs intracellularly (as demonstrated by immunolocalization and pulse-chase experiments). Several fibril containing vacuoles fuse together and form longer Golgi to Plasma-Membrane Carrier Containing Fibrils (GPC^{+cf}). These GPC^{+cf} are targeted to the plasma membrane end extruded towards the extracellular space. The existence of short fibril fragments and vacuoles containing

procollagen and enzymes at the basis of open fibripositors suggests that this is the preferential region where nucleation and propagation occur. The latter mechanisms probably require the involvement of cytoskeletal components and transmembrane receptors. Fibripositor eventually secretes fibrils in the ECM, where they pack in a hexagonal arrangement. Such model presents two innovative features: 1. collagen fibrillogenesis occurs intracellularly; 2. collagen fibrils are delivered in the ECM by membrane projections (fibripositors).

The existence of collagen fibrils confined within the plasma membrane has been already reported. As an example Ploetz and co-workers [32] clearly individuated fibripositors, but they were not able to render a three dimensional reconstruction, starting from individual micrographs. They had to assume that structure as extracellular recesses running deep inside the plasma membrane, rather than vacuoles containing fibrils. However they suggested that extracytoplasmic compartments provide a confined environment for the supramolecular organization of collagen fibrils and that these channels are always associated with a high density of microtubules and microfilaments on the cytoplasmic surface, indicating a high activity of the cytoskeleton in orchestrating matrix supramolecular assembly. These features are in agreement with Canty's model.

Still few data are available on the length distribution of the fibrils delivered by the fibripositors. Certainly they seem shorter than the structures they build. These fibrils, by shape and dimensions, could be identified with the *fibril intermediates* already observed by Birk *et al.* [34] in chick embryo tendon. In the early stages of maturation (<14 days), fibril intermediates display tapered ends. They could be either unipolar or bipolar, having a broad length distribution which spans from 10 up to 30 μm. As the tendon development carries on (between day 16 and 18) a rapid increase in fibril dimension is observed, which suggests that linear and lateral fusion of fibril intermediates occur [35]. Even at this more mature stage of development however, fibril tips are still present in the tendon which indicates that fibrils are not all continuous, from tendon origin to its insertion. These data support a post-depositional maturation of fibril intermediates yielding longer and larger fibrils. Such post-depositional events would involve linear and lateral fibril fusion, as schematically shown in the model below.
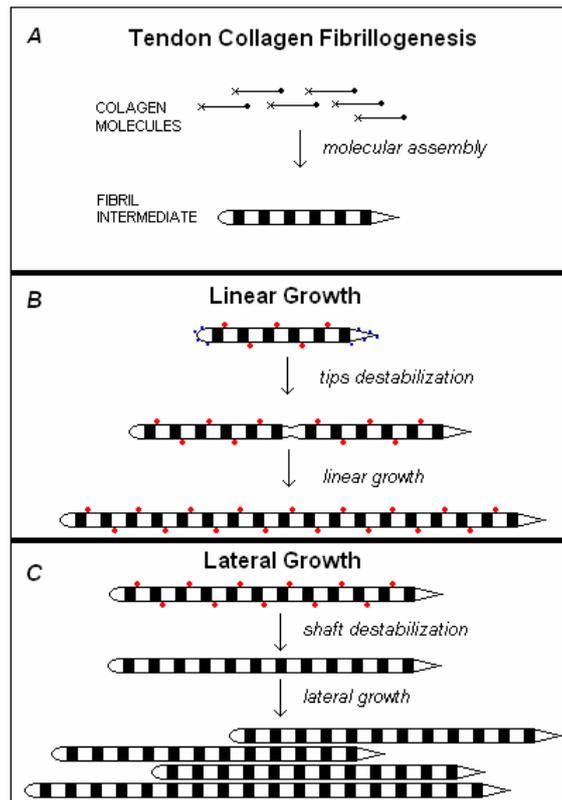
Fig. 19 Fibril lateral and linear growth. A assembly of heterotypic fibrils; B alterations in tip to tip interaction (SLRPs in blue) initiate and control linear growth; C alterations in interactions mediated by FACITs and propeptides (in red) allow lateral fusion. Modified from Zhang *et al.* [37].

The model requires molecular rearrangements in order to guarantee the cylindrical shape of the fibrils. These rearrangements are coherent with the liquid-crystal properties of uncrosslinked collagen fibrils [38].

Fibril fusion is prevented in the early stages of development owing to a shielding effect caused by other interfibrillar macromolecules (SLRPs, FACITs). The rapid increase in fibril length and diameter which is observed around day 17 indicates that there is a trigger which promotes fusion of fibril intermediates. A significant decrease in fibril associated decorin and removal of collagen XIV (a member of the FACIT family) has been reported over this time period [29 and references therein].

An enormous increase in matrix to cell ratio is observed prior birth [33]. 6 weeks old rat tail tendon fibroblasts morphology changes dramatically.
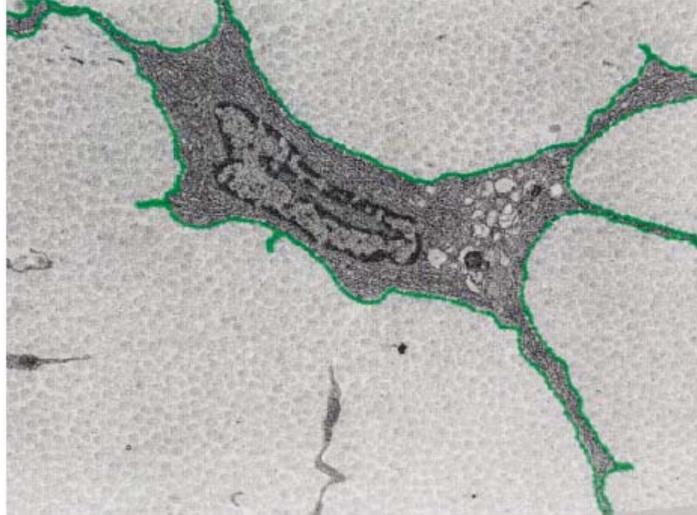
Fig. 20 Fibroblast in 6 weeks old rat tail tendon. Note the morphological differences from embryonic fibroblas in Fig. 14B. From Kadler [39].

The thin fibrils arranged in a rather ordered hexagonal packing seen in embryonic tissue are now characterized by a significantly larger diameter with a broad distribution. The spatial arrangement is completely lost presumably owing to the broad distribution of diameters. Fibripositors disappear and no GPC^{+cf} are observed at this stage. Collagen delivery seem to follow the traditional pathway of collagen molecules and proteolytic enzymes exocytosis in the extracellular matrix [36].

Experimental data seem to suggest a "seeding and feeding" mechanism which regulates embryo tendon development. Nucleation occurs intracellularly in GPC and at the basis of fibripositors, while the propagation seems to occur via collagen adhesion to existing fibrils in open fibripositor or via appending collagen fragments to existing fibrils at the basis of fibripositors. These hypotheses are justified by the evidence that 10 μm long fibril (i.e. longer than a fibripositor) can be traced from bundles in the ECM, to the lumen of a fibripositor, deep within the cytoplasm. As the development continues larger bundle aggregates are formed via retraction of the cell walls which wrap the compartments around [34] (Fig. 21).
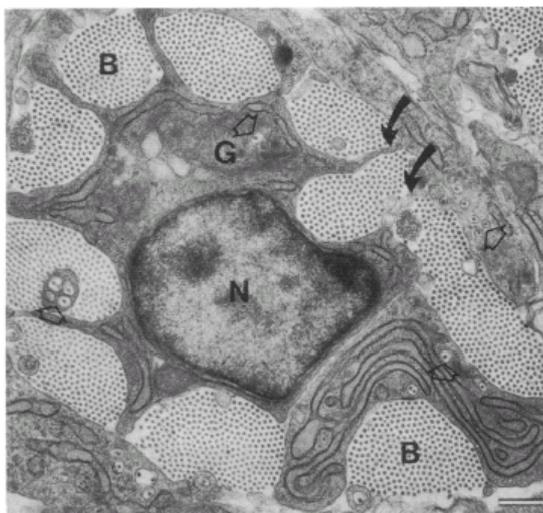
Fig. 21 Extracellular compartmentalization. Fibril forming channels (fibripositors) (open arrows); fibril bundles (**B**). Macroaggregates are formed as cell processes retract between compartments (solid arrows). From Birk et al. [34].

Once the structure has been seeded, fibril undergo a series of post depostional events that make them larger and longer. These events include tip to tip fusion, lateral aggregation and collagen incorporation on existing fibrils. Fibripositors and GPC^{+cf} eventually disappear in stages immediately before birth.

Structure seeding via fibripositor retraction has been observed in several collagen rich tissues like tendon, cornea and dermis. It seems to be a general mechanism for their morphogenesis. However there is no evidence that embryo cartilage displays fibripositors or GPC^{+cf}.

The fibripositor model certainly provides a better comprehension on ECM seeding and development an a supramolecular scale. However several questions still remain unanswered. For example, how can cells create hollow parallel compartments in the early stage of development? What cues regulate collagen deposition along specific, preferential directions? What are the signals that switch the fibripositor activity off in favour of a collagen delivery via simple exocytosis? What is the role of the cytoskeleton in orchestrating collagen assembly?

It is unlike that just a single model can predict the great complexity of the numerous cellular mechanisms involved in tissue morphogenesis, it would be rather the case that different processes occur concomitantly or sequentially over different length scales. The fibripositor model provides snapshots on what happens during tissue morphogenesis but, as all snapshots do, it describes a static scenario. However this model is consistent with the experimental evidence that extensive cell rearrangements and migrations occurs even in the foetal stage [40]. Probably the direction of collagen seeding would be the

preferential direction of cell migration, and in turn fibre orientation would guide other cells in their migration in an "autocatalytic" fashion.

The mechanism controlling cell migration must provide signals for starting, polarity and cessation of the movement. Polarity is believed to arise from a combination of phenomena which include contact inhibition of locomotion, chemotaxis, adhesion gradients and structural and mechanical anisotropies of the extracellular environment [41]. In particular adhering cells probe the mechanical properties of the environment which surrounds them, and use the resulting information to attach, spread, position and orient themselves. A growing body of evidence suggest that focal adhesion based on transmembrane receptors from the integrins family act as mechanosensors that actively participates into cell regulation [42]. Of course cytoskeleton is believed to have great importance in cell migration and in exerting forces on the surroundings. However its role in the mechanism of contact guidance remains still unclear. Contact guidance, besides morphogenesis, is involved in several homeostatic and pathological processes like angiogenesis, inflammation, metastasis and wound healing [43, 44]. Recent studies have revealed significant analogies between how tissues development in the embryo stages and how they are repaired during wound healing [45]. Once an adult tissue is settled it is homeostatically maintained through a dynamic equilibrium of cell death and replacement, synthesis and degradation. Almost all tissues remain in this constant turnover for the entire life of the organism. This equilibrium is however thrown off balance whenever the organism is wounded. In this case a cascade of intracellular and extracellular events, which closely resemble those of embryonic development, occur in order to replace the missing tissue and restore its functionality. There exists a crossover between the signals that guide the directed migrations and subsequent behaviours of inflammatory cells at wound site, and those signals that guide various migrating cells during normal development.

5. Microfibrillar elements and other microconstituents of the dermal matrix

An experimental campaign has been designed in order to gain a better insight into composition, spatial arrangement of the micro-constituents and macroscopic mechanical properties of dermis, whose details will be presented in the next chapters. Dermis has been chosen as preferential tissue to study since its loose three dimensional and complex structure would serve as a general model for connective tissues. Aim of the present section is to provide a brief outline of the extracellular matrix of the skin. In particular, great attention will be paid on those proteins which play a structural, load bearing role, namely, collagen, elastin and fibril attached proteoglycans.

The most relevant features concerning biosynthesis and assembly of fibrillar collagens, as well as their interaction with other ECM macromolecules, have been presented so far. However, besides fibrillar collagens, other collagen types reside in dermis.

Type IV collagen is a major component of the basement membrane in the dermal-epidermal junction (DEJ). The primary structure of type IV collagen presents several interruptions in the repeating Gly-X-Y sequence, providing the molecule with increased flexibility. This allow the assembly of type IV collagen in the form of a planar meskwork-like structure, rather than the ordered axisymmetric fibres formed by fibrillar collagens. The supramolecular structures formed by the assembly of type IV collagen is believed to interact with other DEJ macromolecules like heparin sulfate proteoglycans and laminin. Moreover, it acts as a scaffold for the attachment of basal keratinocytes. This interaction contributes for the mechanical stability of the epidermal layer.

Type VI collagen has a short triple helical domain and very large terminal globular domains. It assembles intracellularly in the form of tetramers which, in the extracellular space aggregate to form filaments. These filaments form extensive networks. In skin, the type VI network permeates the dermis in a highly branched manner, which concentrates around the endothelial basement membrane and wraps collagen bundles around [46].

Type XII and XIV collagens belong to the family of the Fibril-Associated Collagens with interrupted Triple helices. In skin type XII and XIV collagens have been localized along the surface of fibrils. The non helical domain of theses macromolecules is believed to mediate the interaction between and other ECM molecules, which could be a key feature in regulating spatial arrangement of the collagen network.

Elastic fibres consist of two biochemically and structural distinct components: elastin and elastin-associated microfibrils. Mature elastin is an highly hydrophobic and insoluble

protein. the degree of hydrophobicity confer elastin with rubber-like elastic properties. The genesis of elastic fibres involves the deposition of tropoelastin (the soluble form of elastin) on a preformed microfibrils template rich in fibrillin [47]. Fibrillins are indeed the major microstructural components of the microfibrils. They aggregate to form beaded microfibrils of 56 nm periodicity. The relative amount of elastin and microfibril is tissue dependent. Usually large elastic fibres possess a bulky core of amorphous elastin surrounded by a thin shell of microfibrils. However it is possible to localize thin elastic fibres practically devoid of elastin. Structural integrity of elastic fibres is provided by extensive covalent crosslinking. In particular the enzyme lysyl oxidase catalyzes the reaction between lysine residues. This leads to the formation of unique crosslinks, namely desmosine and isodesmosine. The elastin is not uniformly distributed in skin. Thinner fibrils are present in papillary dermis and increasingly thicker fibrils are present in reticular dermis. A three dimensional network rich in microfibrils course through the papillary layer up toward the basement membrane. Regular elastic trunks transverse the reticular dermis without an evident branching [46].

The dominant proteoglycan of the dermis is decorin, which belongs to the small leucine rich family of proteoglycans. It consist of a core protein of 30 kDa to which are attached 2 or 3 oligosaccharides and a single glycosamminoglycan chain, usually dermatan sulphate (DS). The core protein binds to type I collagen molecules, projecting the GAG chain out in the gap region of the fibril. Derims also contains another SLRP, the biglycan. The core protein of this proteoglycan is similar to the one in decorin, although it is genetically distinct. Biglycan usually displays two DS GAG chains and it does not seem to interact with collagen. Decorin is abundant in the whole dermal layer and it is more present in the papillary dermis. Biglycan has been found only at the DEJ. The pattern distribution of decorin is consistent with the hypothesis that it exerts a role in regulating collagen fibre diameter.

6. Conclusions

Tissue morphogenesis and homeostasis is the result of two factors: self assembly and cellular recognition. *In vitro* experiments have shown that some ECM components possess enough information to drive a self assembling process, but the structure they build is far from being considered a functional tissue. There is growing evidence that cells seem to exercise exquisite control over ECM proteins assembly. However cells in culture do not faithfully replicate the synthesis of ECM macromolecules that is observed *in vivo*. Thus, in native tissues there a cross-talk between cells and ECM which governs the continuous processes of remodelling and turnover. A very large number of macromolecules are involved in settlement and development of the ECM. Future studies have to be directed at understanding the complex interactions between cells themselves and cell-EMC; the signals that trigger biosynthetic events and the development of a new model for *in vitro* studies which closely mimics the early stages of tissue morphogenesis.

7. References

1. Gelse K., Pöschl E. and Aigner T.: "Collagens-structure, function, and biosynthesis". Advanced Drug Delivery Reviews **55**, 1531-1546, 2003.

2. Beck K., Brodsky B.: "Supercoiled Protein Motifs: The Collagen Triple-Helix and the α-Helical Coiled Coil". Journal of Structural Biology **122**, 17-29, 1998.

3. Tasab M., Batten MR., Bulleid N.J.: "Hsp47: a molecular chaperone that interacts with and stabilizes correctly-folded procollagen". EMBO Journal **19**, 2204-2211, 2000.

4. Engel J., Prockop D.J.: "The zipper-like folding of collagen triple helices and the effects of mutations that disrupt the zipper". Annual review of biophysics and biophysical chemistry **20**, 137-152, 1991.

5. Lamandé S.R., Bateman J.F.: "Procollagen folding and assembly: the role of endoplasmic reticulum enzymes and molecular chaperones". Seminars in cell & developmental biology **10**, 455-464, 1999.

6. Lees J.F., Tasab M., Bulleid N.J.: "Identification of the molecular recognition sequence which determines the type-specific assembly of procollagen". EMBO Journal **16**, 908-916, 1997.

7. Hulmes D.J.S: "Building collagen molecules, fibrils, and suprafibrillar structures". Journal of Structural Biology **137**, 2-10, 2002.

8. Vitagliano L., Berisio R., Mazzarella L., Zagari A.: "Structural bases of collagen stabilization induced by proline hydroxylation". Biopolymers **58**, 459-464, 2001.

9. Bailey A.J., Paul R.G., Knott L.: "Mechanisms of maturation and ageing of collagen". Mechanisms of Ageing and Develpment **106**, 1-56, 1998.

10. Bateman J.F., Lamandé S.R., Ramshaw J.A.M.: "Collagen Superfamily". In Extracellular Matrix Volume **2** Molecular Components and Interaction. Comper W.D. Ed. Harwood Academic Publishers 1996.

11. Kadler K.E., Hojima Y., Prockop D.J.: "Assembly of collagen fibrils *de novo* by cleavage of the type I pC-collagen with procollagen C-proteinase. Assay of critical concentration demonstrates that collagen self-assembly is a classical example of an entropy-driven process". The Journal of Biolgical Chemistry **262**, 15696-15701, 1987.

12. Cox R.W., Grant R.A., Kent C.M.: "The interpretation of electron micrographs of negatively stained native collagen". Journal of Cell Science **10**, 547-554, 1972.

13. Hodge A.J, Schmitt F.O.: "The charge profile of the tropocollagen macromolecule and the packing arrangement in native-type collagen fibrils". Proceedings of the National Academy of Sciences of the United States of America **46**, 186-197, 1960.

14. Kadler K.E., Holmes D.F., Trotter J.A., Chapman J.A.: "Collagen fibril formation". The Biochemical Journal **316**, 1-11, 1996.

15. Bailey A.J., Paul R.G.: "The mechanisms and consequences of the maturation of a collagen". Proceedings of the Indian Academy of Sciences (Chemical Sciences) **111**, 57 – 69, 1999.

16. Bailey A.J., Paul R.G., Knott L.: "Mechanisms of maturation and ageing of collagen". Mechanisms of Ageing and Development **106**, 1 – 56, 1998.

17. Paul R.G., Bailey A.J.: "Glycation of collagen: the basis of its central role in the late complications of ageing and diabetes". The international journal of biochemistry & cell biology **28**, 1297-1310, 1996.

18. Miyahara M., Hayashi K., Berger J., Tanzawa K., Njieha F.K., Trelstad R.L., Prockop D.J.: "Formation of collagen fibrils by enzymic cleavage of precursors of type I collagen in vitro". The Journal of biological chemistry **259**, 9891-9898, 1984.

19. Gross J., Highberger J.H., Schmitt F.O.: "Extraction of collagen from connective tissue by neutral salt solutions". Proceedings of the National Academy of Sciences of the United States of America **41**, 1-7, 1955.

20. Wood G.C., Keech M.K.: "The formation of fibrils from collagen solutions. 1. The effect of experimental conditions: kinetic and electron-microscope studies". The Biochemical Journal **75**, 588-598, 1960.

21. Graham H.K., Holmes D.F., Watson R.B., Kadler K.E.: "Identification of collagen fibril fusion during vertebrate tendon morphogenesis. The process relies on unipolar fibrils and is regulated by collagen-proteoglycan interaction". Journal of Molecular Biology **295**, 891-902, 2000.

22. Fleischmajer R., MacDonald E.D., Perlish J.S., Burgeson R.E., Fisher L.W.: "Dermal collagen fibrils are hybrids of type I and type III collagen molecules". Journal of Structural Biology **105**, 162-169, 1990.

23. Fleischmajer R., Perlish J.S., Burgeson R.E., Shaikh-Bahai F., Timpl R.: "Type I and type III collagen interactions during fibrillogenesis". Annals of the New York Academy of Sciences **580**, 161-175, 1990.

24. Hulmes D.J., Wess T.J., Prockop D.J., Fratzl P.: "Radial packing, order, and disorder in collagen fibrils". Biophyscal Journal **68**, 1661-1670, 1995.

25. Smith J.W.: "Molecular Pattern in Native Collagen". Nature **219**, 157 - 158, 1968.

26. Birk D.E.: "Type V collagen: heterotypic type I/V collagen interactions in the regulation of fibril assembly". Micron **32**, 223-237, 2001.

27. Birk D.E., Hahn R.A., Linsenmayer C.Y., Zycband E.I.: "Characterization of collagen fibril segments from chicken embryo cornea, dermis and tendon". Matrix Biology **15**, 111-118, 1996.

28. Ottani V., Raspanti M., Ruggeri A.: "Collagen structure and functional implications". Micron **32**, 251 – 260, 2001.

29. Canty E.G., Kadler K.E.: "Collagen fibril biosynthesis in tendon: a review and recent insights". Comparative Biochemistry and Physiology. Part A, Molecular & Integrative Physiology. **133**, 979 - 985, 2002.

30. Holmes D.F., Gilpin C.J., Baldock C., Ziese U., Koster A.J., Kadler K.E.: "Corneal collagen fibril structure in three dimensions: Structural insights into fibril assembly, mechanical properties, and tissue organization". Proceedings of the National Academy of Sciences of the United States of America **98**, 7307 - 7312, 2001

31. Linsenmayer T.F., Fitch J.M., Gordon M.K., Cai C.X., Igoe F., Marchant J.K., Birk D.E.: "Development and roles of collagenous matrices in the embryonic avian cornea". Progress in retinal and eye research **17**, 231 - 265, 1998.

32. Ploetz C., Zycband E.I., Birk D.E.: "Collagen fibril assembly and deposition in the developing dermis: segmental deposition in extracellular compartments". Journal of Structural Biology **106**, 73 - 81, 1991.

33. Birk D.E., Trelstad R.L.: "Extracellular compartments in tendon morphogenesis: collagen fibril, bundle, and macroaggregate formation". Journal of Cell Biology **103**, 231 - 240, 1986.

34. Birk D.E., Zycband E.I., Winkelmann D.A., Trelstad R.L.: "Collagen fibrillogenesis in situ: fibril segments are intermediates in matrix assembly". Proceedings of the National Academy of Sciences of the United States of America **86**, 4549 - 4553, 1989.

35. Birk D.E., Zycband E.I., Woodruff S., Winkelmann D.A, Trelstad R.L.: "Collagen fibrillogenesis in situ: fibril segments become long fibrils as the developing tendon matures". Developmental Dynamics **208**, 291 - 298, 1997.

36. Canty E.G., Lu Y., Meadows R.S., Shaw M.K., Holmes D.F., Kadler K.E.: "Coalignment of plasma membrane channels and protrusions (fibripositors) specifies the parallelism of tendon". The Journal of Cell Biology **165**, 553 - 563, 2004.

37. Zhang G., Young B.B., Ezura Y., Favata M., Soslowsky L.J., Chakravarti S., Birk D.E.: "Development of tendon structure and function: regulation of collagen fibrillogenesis". Journal of Musculoskelet and Neuronal Interactions **5**, 5 - 21, 2005.

38. Chapman J.A.: "The regulation of size and form in the assembly of collagen fibrils in vivo". Biopolymers **28**, 1367 - 1382, 1989.

39. Kadler K.E.: "Matrix loading: assembly of extracellular matrix collagen fibrils during embryogenesis". Birth Defects Research (Part C) **72**, 1 - 11, 2004.

40. Lecaudey V., Gilmour D.: "Organizing moving groups during morphogenesis". *Current Opinion in Cell Biology* **18**, 102-107, 2006.

41. Sanders E.J., Hu N., Prasad S.: "Guidance of filopodial extension by fibronectin-rich extracellular matrix fibrils during avian gastrulation. A study using confocal microscopy". *International Journal of Developmental Biology* **38**, 701-707, 1994.

42. Bischofs I.B., Schwarz U.S.: "Cell organization in soft media due to active mechanosensing". *Proceedings of the National Acadademy of Sciences of the United States of America* **100**, 9274-9279, 2003.

43. Dubey N., Letourneau P.C., Tranquillo R.T: "Guided Neurite Elongation and Schwann Cell Invasion into Magnetically Aligned Collagen in Simulated Peripheral Nerve Regeneration". *Experimental Neurology* **158**, 338–350, 1999.

44. Enever P.A., Shreiber D.I., Tranquillo R.T.: "A Novel Implantable Collagen Gel Assay for Fibroblast Traction and Proliferation during Wound Healing". Journal of Surgical Research **105**, 160-172, 2002.

45. Martin P., Parkhurst S.M.: "Parallels between tissue repair and embryo morphogenesis". *Development* **131**, 3021-3034, 2004.

46. Keene D.R., Marinkovich M.P., Sakai L.Y.: "Immunodissection of the connective tissue matrix in human skin". *Microscoscopy Research and Technique* **38**, 394 - 406, 1997.

47. Kielty C.M., Sherratt M.J., Shuttleworth C.A.: "Elastic fibres". Journal of Cell Science 115, 2817-2828, 2002.

Chapter 2
Experimental characterization of bovine dermis and goat skin

1. Introduction

In collagen rich soft biological tissues there exists a correlation between their inner microstructure and their macroscopic mechanical properties. The interest in the mechanical and rheological behaviour of connective tissues involves several disciplines of biological and clinical research. As examples in plastic [1], orthopaedic [2, 3] and cardiovascular surgery [4], transplantations [5], incision design [6], wound healing process [7], etc.

A general approach for the quantitative description of connective tissues mechanical properties is difficult to achieve. Connectives possess very different microstructures, despite having quite similar composition. One of the simplest model, in terms of spatial configuration of its microconstituents, is the tendon. Tendons are mainly subjected to uniaxial tension and collagen fibres are close packed in parallel bundles. Skin structure is more complex. It is considered as an entangled mass of fibrous elements, although the predominant fibre directions lie parallel to the epidermal surface. Dermal components are arranged in a way that cause the skin to resist to biaxial stresses. In the present work, skin has been chosen as a more general model to study connective tissue macroscopic properties.

Skin is a multilayered material. The superficial epidermis is populated by keratinocytes and the intracellular hydrophobic keratin is the main constituent. The role of the epidermal layer in affecting mechanical properties is negligible in a full thickness skin sample. The dermis lies beneath the epidermis, which is poorly cellularized and mainly consisting of a dense arrangement of extracellular matrix components. Collagen makes up over 75% of its dry wet (fat free) weight. Collagen is assembled in fibre bundles which form a three dimensional network. Interwoven within collagen bundles is the elastic network. Proteoglycans, hyaluronic acid and other soluble proteins form the so called "ground substance". The dermis itself can be divided in a papillary layer (closer to the epidermis) and the deep reticular dermis. The former comprises about 20% of full dermal thickness. In human papillary dermis, collagen fibres are packed in thin bundles of less than 10 μm diameter. Reticular dermis is constituted by larger bundles (more than 50 μm) which form

a loose entangled mass [8 and references therein]. It should be borne in mind that there does not exist a proper "border" layer between the two strata: collagen fibres rather change in shape and dimension in a continuous and gradual manner.

The mechanical response of skin is non linear, anisotropic and time dependent. The non linear and anisotropic aspects of skin mechanical properties have been widely examined. The source of such peculiar properties has been associated to weaving and spatial arrangement of collagen fibres. Time dependence is manifested by viscoelasticity and preconditioning. Even though these phenomena are well characterized from an experimental viewpoint, their macromolecular origin has not yet been unravelled. There is growing evidence that non collagenous macromolecules possess relevant characteristics which affect both skin static and time dependent properties. Ageing is another key factor in determining the mechanical response of a tissue. Skin shows dramatic changes in mechanical and viscoelastic properties during the early stages of development. These changes are caused by substantial maturation and remodelling of the extracellular matrix [9]. Collagen fibrils fuse laterally to form large bundles and an extensive collagen crosslinking occurs over this time period, despite total collagen content remains roughly unaltered. Moreover elastin network is enriched of amorphous elastin [10] in a highly localized manner.

This chapter presents the results of a experimental campaign designed in order to have a better insight into bovine skin macroscopic mechanical properties and how these properties can be affected by microstructure and composition. Mechanical tests, both "static" and dynamic have been performed in order to gain an exhaustive description of skin mechanical behaviour. Differential Scanninig Calorimetry (DSC) and Hydrothermal Isometric Tension (HIT) have been included in the experimental set up since they are quick and reliable tests which provide useful information on collage crosslinking and spatial assembly. Scanning and Transmission Electron microscopy, as well as histological optic examinations, showed morphological details over a wide scale of magnifications, i.e. from a whole dermal cross section down to individual collagen fibrils.

2. Materials and methods

2.1 Mechanical tests

Traction tests – foetal skin and leather

Traction tests have been carried out on samples taken from nine foetal skins (named C, I, M, N, Q, R, T, U and Z). Mechanical tests have been undertaken on both soaked and chrome tanned samples. Tanning process details are reported in the **Annex I**. The specimens have been taken away according to the official sampling area, provided by the ISO2419 standard, both along the backbone direction and in the orthogonal direction. Shape and dimensions of the specimens are shown in the following scheme:
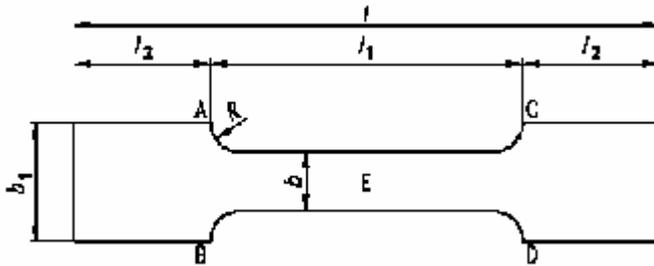
Designation	Measure [mm]
l	40
l_1	20
L_2	10
b	4
b_1	9.3

fig. 1 Specimen shape   **tab. 1** Specimen dimensions

Tests have been carried out using a Stable Micro Systems testing machine at crosshead speed of 40 mm/min.

Foetal calf skin samples have been soaked in distilled water for 24 hours at 4°C prior testing.

Chrome tanned leather have been stored in the conditioning room (60% humidity and 23°C) for at least 24 hours prior testing.

Traction tests – bovine skin

Traction tests have been carried out on specimens cut from one adult (> 18 months old) bovine hide (named bov). The specimens have been taken away according to the official sampling area, provided by the ISO2419 standard, both along the backbone direction and in the orthogonal direction. Specimen dimensions are reported in the following table:

Designation	Measure [mm]
l	110
l_1	50
l_2	30
b	10
b_1	25

tab. 2 Specimen dimensions

Designations refer to fig. 1. Tests have been carried out using a Stable Micro Systems testing machine at crosshead speed of 100 mm/min.

2.2 Dynamic mechanical tests

Oscillatory shear and relaxation tests – Sample preparation

One large skin stripe has been removed from the ventral section of a 24 month old female bovine. The stripe has been manually unhaired and defleshed with a surgical blade and frozen at -80°C within three hours after slaughtering. Fourteen 15 mm disks have been punched from the skin stripe while it was partially frozen. The uppremost layer has been cut away in order to eliminate the influence of the hair follicules, sweat glands and keratins on the mechanical tests. Each sample has been splitted in two layers, approximately 2 mm thick. In the following the terms **grain** and **corium** refer to the upper and lower dermis strata respectively as depicted in fig. 2.
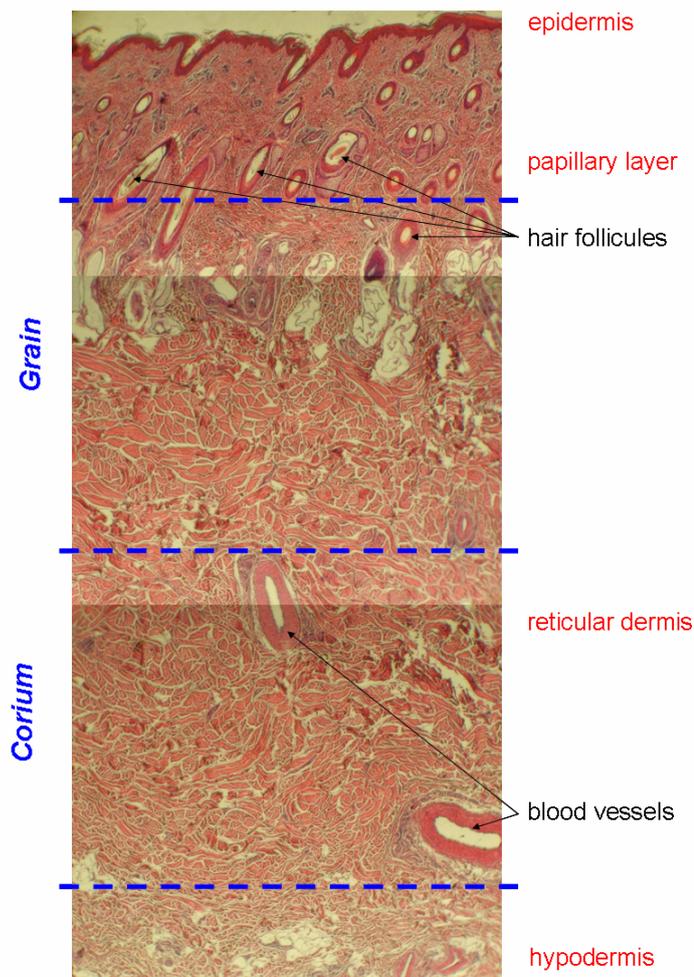
fig. 2 Cross section of bovine skin. Hematoxylin and eosin. Optical micrograph 4X.

Oscillatory shear and relaxation tests – Treatment with trypsin

Trypsin is supposed to digest fibril associated proteoglycans, FACITs and other interfibrillar proteins which are sensitive to serine proteases attack. Trypsin treatment leaves fibrillar collagen and elastin fibres intact [12].

The enzyme solution consisted of a 10mM phosphate buffer, pH 7.1, with 150 mM NaCl, 1 mM $CaCl_2$ containing 1 mg/ml of enzyme (Trypsin T8003, Sigma-Aldrich). Four corium disks have been impregnated in the enzyme solution on a 10 ml per gram of skin (wet weight) basis for 72 hours at 4°C to allow uniform distribution of the enzyme throughout the sample thickness. Two hours incubation at 37°C followed the impregnation step.

Oscillatory shear and relaxation tests – Treatment with Chondroitinase ABC

Chondroitinase enzyme (C2905 Sigma-Aldrich) degrades dermatan sulphate, chondroitin sulphate and hyaluronic acid. The enzyme has been reconstituted in 0.01%

bovine serum albumin solution prior impregnation. Dilution has been made in 50 mM TRIS buffer (pH 7.4), 150 mM NaCl, 20 mM sodium EDTA, 1mM PMSF, 2 mM NEM. All chemicals have been purchased from the Sigma-Aldrich Company. Five corium disks have been impregnated in 5 ml/sample buffer solution containing 0.5 enzyme units for 72 hours at 4°C to allow uniform distribution of the enzyme. Five hours incubation at 37°C followed the impregnation step.

Oscillatory shear and relaxation tests – Treatment with Elastase

The elastase (E7885 Sigma-Aldrich) has been used in order to break the elastin network down. Since elastic network is assumed to be a minor component of the reticular dermis [13], the enzyme treatment has been performed exclusively on grain specimens. The enzyme solution consisted of TRIS buffer (pH adjusted at 8.5). Five samples have been impregnated in 5 ml of solution with 0.5 mg of enzyme for 72 hours at 4°C to allow uniform distribution of the enzyme within the tissue. Samples have been incubated at 37°C for 5 hours prior testing.

Oscillatory shear and relaxation tests – Experimental set up

Skin samples have been tested in *oscillatory shear* using a Gemini Rheometer (Bohlin) in the strain-controlled mode with serrated parallel plates (15 mm) geometry. More in details, storage (**G'**) and loss (**G"**) moduli have been recorded as function of the frequency of the applied strain. An amplitude sweep has been performed on each sample prior testing, in order to ensure that the strain applied falls within the linear region. For all the tested samples the value of 0.1% strain has been chosen. Both G' and G" have been monitored in the 0.01 – 10 Hz frequency range. Stress relaxation experiments have been performed alongside oscillation tests. Such technique consists in monitoring modulus variations with time after the application of a step strain.

In order to avoid the intrinsic tissue variability which could mask the effect of enzymatic treatments, each disk has been used both as control and treated sample. In particular each specimen has been soaked in the same buffer solution of the intended treatment, but without the enzyme for 24 hours. The test of these specimens have been considered as the control. After testing, the samples have been treated with one of the methodology described above and tested once again.

In the stress relaxation experiments, the samples have been subjected to a step strain shear of 0.1% amplitude in 10 ms. The deformation has been kept constant for 1000s, while monitoring the relaxation modulus.

All tests have been performed in humidity chamber at 80% relative humidity and at 37°C.

Dynamic traction tests – Trypsin treatment

Six dumbbell shape skin samples have been punched from a kid skin (< 12 months). The specimens have been carefully unhaired and defleshed with a surgical scalpel. A subset of three specimens have been treated with trypsin (supplied by Novozymes). The treatment has been performed in an analogous manner as previously described. The enzyme solution consisted of a TRIS buffer, pH 8.5, with 150 mM NaCl, 1 mM $CaCl_2$ containing 1 mg/ml of enzyme. Three skin specimens have been impregnated in the enzyme solution on a 10 ml per gram of skin (wet weight) basis for 24 hours at 4°C to allow uniform distribution of the enzyme within the tissue. Two hours incubation at 37°C in an orbital shaker followed the impregnation step. Control samples have been treated in the same solution but without the enzyme.

Dynamic traction tests – Elastase treatment

Six skin samples have been punched from a kid skin (< 12 months). The specimens have been carefully unhaired and defleshed with a surgical scalpel. A subset of three specimens have been treated with elastase (E7885 Sigma-Aldrich). The enzyme solution consisted of TRIS buffer, pH 8.5. Three skin specimens have been impregnated in the enzyme solution on a 10 ml per gram of skin (wet weight) basis with 2 mg of enzyme powder. Samples have been kept for 24 hours at 4°C to allow uniform distribution of the enzyme within the tissue. Five hours incubation at 37°C in an orbital shaker followed the impregnation step. Control samples have been treated in the same solution but without the enzyme.

Dynamic traction tests – Measurement

Trypsin treated samples (and control) have been subjected to 5 cycles of loading and unloading in the strain range of 0 – 17.5% at constant speed of 0.17 mm/s.

Elastase treated samples (and control) have been subjected to 5 cycles of loading and unloading in the strain range of 0 – 20% at constant speed of 0.17 mm/s.

Specimens have been tested in wet state at 23°C using a Stable Micro Systems testing machine with a 10N load cell.

2.3 Thermal analyses

Differential Scanning Calorimetry

Eight foetal calf skins (Samples C, I, M, N, Q, T, U and Z) and one (sample bov) bovine skin samples have been unhaired and unfleshed with a surgical scalpel. Each sample has been soaked in bidistilled water for 48h at 4°C. Water has been changed every 12h. Surface water has been removed prior testing.

Nine foetal calf chrome tanned leathers have been stored in a conditioning room (60% humidity and 23°C) for at least 24 hours prior testing. DSC analysis was performed with a Metler-Toledo model DSC822e.

The temperature program consisted in a ramp to – 40°C up to 80°C at a heating rate of 10 °Cmin^{-1}. Each experiment has been carried out in triplicate

Hydrothermal Isometric Tension

Samples have been taken from seven foetal calf skins (Sample C, I, Q, R, T, U and Z) and one (Sample bov) bovine skin according to the official sampling ISO2419 standard and shaped as shown in fig 1. One Foetal calf sample (Sample R) has been treated with NaBH$_4$ (borate buffer pH 9 at 0°C for 90 min). The HIT test consists in monitoring the stress produced by collagenous tissue while it is heated above its shrinkage temperature. Each sample has been equilibrated in distilled water at room temperature for 30 min prior testing and then it has been positioned between the jaws, with an preload of 50g. The bath has been heated up to 85°C (heating rate 2°Cmin^{-1}) and then the temperature has been kept constant for 2 hours. Each experiment has been carried out in triplicate.

Stepwise HIT test

Six specimens have been cut from one foetal calf skin (Sample R). A subset of three specimens have been processed with NaBH$_4$ (borate buffer pH 9 at 0°C for 90 min). The rationale of the test is analogous to the HIT test. The only difference is that the heating is a step function with 5°C amplitude increase and 75 min intervals. The starting and final temperatures have been set on 60°C and 85°C respectively.

2.4 Morphological and histological examinations

Scanning Electron Microscopy

SEM examinations have been carried out using a Hitachi S-3000N SEM. Dry specimens have been gold sputtered prior examination

Transmission Electron Microscopy

Transmission electron micrographs have been kindly performed by Dr. Hannah Koon at the Department of Biology of the University of York, UK.

Histological Stains

Foetal calf skin cross section for histological examination have been cut with a Leica cryo-microtome and mounted on a glass slide. Sections have been stained with orcein red for elatic fibres following a conventional process.

Adult (>12 moths) bovine skin cross section have been paraffin embedded and cut with a microtome and mounted on a glass slide. Sections have been stained with Haematoxylin and Eosin following a conventional staining process.

Total Collagen determination

The total collagen content in the tissue has been determined by following a spectrophotometric procedure developed and reported by Jamall et al. [14]. 400mg of unhaired fresh foetal calf skin were placed in a digest tube with 5ml of HCl 37% and left overnight in oven at 100°C. After complete digestion the solution was neutralised with concentrate NaOH and the volume made up to 10ml.

0.55ml of this solution were added to a solution of 1.27ml of diluent (2-propanol: water, 2:1) and Choramine T and then were left to react at room temperature for 10 min. After the reaction, 2.3 ml of Ehrlichs reagent (0.6 M DMAB in 50ml of 2-propanol and 9ml $HClO_4$) were added and the solution was left to react for 10 min at 70°C. Spectrophotometric readings were taken at 555nm using a Perkin Elmer spectrophotometer and the unknown concentration was extrapolate from a standard curve obtained using a standard solution (0.100g/L) of L-hydroxyproline at different concentration.

Elastin determination

Elastin from foetal calf, adult bovine and goat skin samples has been extracted using the Fastin Elastin Assay provided by Biocolor Ltd. Approximately 1 g of skin sample has been solubilised in ethanolic potassium hydroxide (1M KOH in 80% ethanol) at 37°C for 12h. Elastin has been subsequently recovered from the solution and stained using the chemicals provided by the assay.

Spectrophotometric readings were taken at 513nm using a Perkin Elmer spectrophotometer and the unknown concentration was extrapolated from the standard curve obtained using a standard solution (1mg/ml) of elastin at different concentration.

Glycosamminoglycan determination

Glycosamminoglycans from kid skin have been extracted using the Blyscan Glycosamminoglycan Assay provided by Biocolor Ltd. The extraction procedure consist of both salt extraction (4M Guanidine-HCl) and papain extraction. GAGs have been extracted from approximately 1 g of skin sample. GAGs have been recovered from the solution and stained using the chemicals provided by the assay.

Spectrophotometric readings were taken at 656nm using a Perkin Elmer spectrophotometer and the unknown concentration was extrapolated from the standard curve obtained using a standard solution (0.1mg/ml) of GAGs at different concentration.

2.5 Statistical analysis

One-way analysis of variance has been performed with Microsoft Excel 2003 software.

3. Results

Collagen content

Collagen content of foetal and adult skin samples is reported in tab. 3. Data are normalized respect to the sample wet weight.

Skin samples	mg of collagen /gram of skin	% collagen
foetal skin s	206	20.6
foetal skin p	244	24.4
foetal skin d	170	17.0
foetal skin f	270	27.0
Adult bovine 1	207	20.7
Adult bovine 2	216	21.6

tab. 3 Collagen concentration in wet tissues

Elastin content

Elastin content, provided by the *Fastin© Assay* of both foetal and mature skin samples is reported in the table below.

Skin samples	mg/g of wet skin	% for 1g of wet skin
foetal skin s	1.36	0.14
foetal skin p	1.66	0.17
foetal skin d	0.56	0.06
foetal skin f	1.57	0.16
Adult bovine 1	9.68	1
Adult bovine 2	9.51	1

tab. 4 Elastin concentration in wet tissues

Static traction testing

Typical stress-strain diagram for both soaked skin and leather is reported in fig. 3.
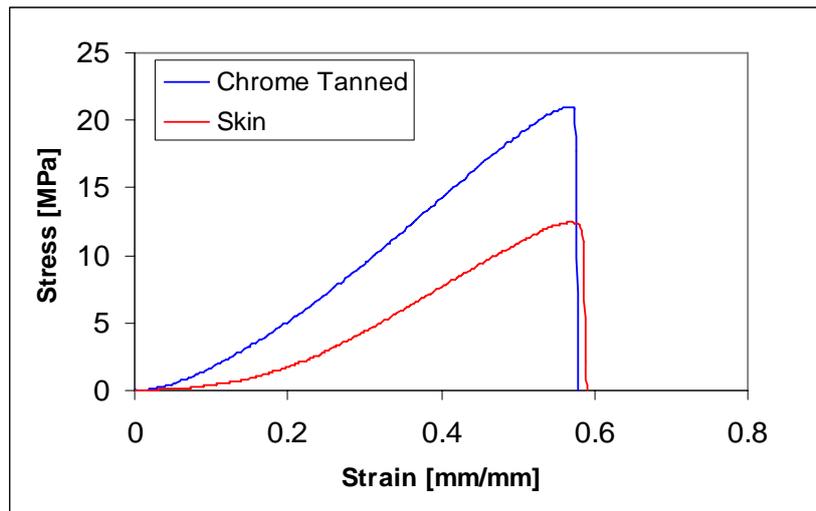
fig. 3 Sample N stress-strain plot for skin and leather

Tangent in the origin will be referred as starting modulus in the following, while the slope of the linear region is the linear modulus. The part of the diagram before the linear region is usually referred as the *toe region*.

In the following tab. 5 and tab. 6 are summarized the values of elongation at break, ultimate tensile strength, linear modulus, for soaked skin and leather respectively.

Sample	Elongation at break [%]		Ultimate tensile strenght [MPa]		Modulus	
	AVG	ST. DEV.	AVG	ST. DEV.	AVG	ST. DEV.
C	62.47	5.54	16.45	0.39	47.88	4.33
I	55.87	3.83	20.55	0.72	59.69	6.52
M	49.07	1.50	16.74	0.19	51.86	0.97
N	63.88	6.62	12.89	0.30	33.65	5.67
Q	57.76	4.15	16.60	1.22	47.54	3.64
T	54.94	1.46	17.70	0.43	50.84	2.27
U	66.37	5.69	16.84	1.40	51.13	7.51
Z	62.00	5.75	20.61	3.04	58.29	6.72

tab. 5 Skin mechanical properties

Sample	Elongation at break [%]		Ultimate tensile strenght [MPa]		Modulus	
	AVG	ST. DEV.	AVG	ST. DEV.	AVG	ST. DEV.
C	53.29	2.45	38.42	3.65	88.07	12.09
I	61.32	0.90	33.91	0.86	79.85	2.95
M	55.55	2.39	40.71	3.00	75.10	10.83
N	62.96	4.00	29.94	2.24	61.50	5.92
Q	43.03	2.67	46.86	2.81	107.04	16.38
T	71.34	2.27	30.51	1.36	73.03	3.00
U	46.00	3.44	31.23	3.13	95.71	6.96
Z	50.22	2.67	33.51	1.66	96.53	4.26

tab. 6 Leather mechanical properties

Rheological experiments

Logaritmic plots of G' and G" against frequency of untreated grain and corium specimens are reported in fig. 4 and fig. 5. Grain dynamic moduli are higher than the corium ones of about a factor ten. Moreover, the loss modulus, for both grain and corium, is always smaller than the storage modulus all over the frequency range scanned. The tanδ, i.e. the ratio of loss modulus to storage modulus is reported in fig. 6. Unfortunately, owing to the compliance of the samples tested, especially for the corium specimens, the data acquired at frequencies above 3 Hz are affected by some noise. Such data scattering is of course enormously amplified in the tanδ plot.
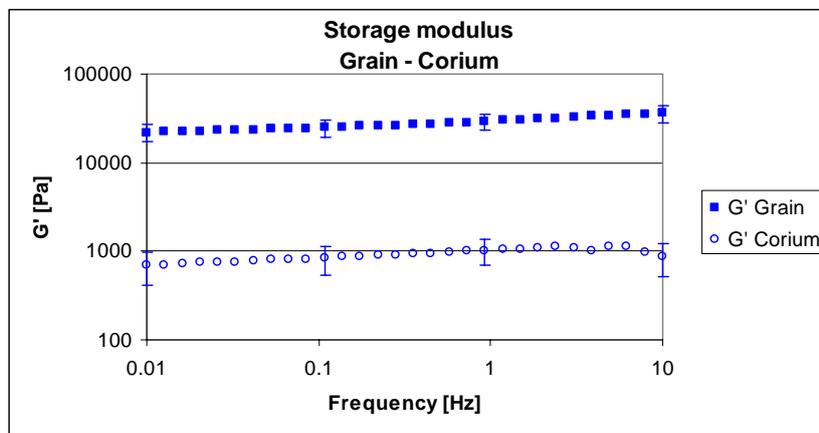
fig. 4 Grain and corium storage modulus. Untreated samples.
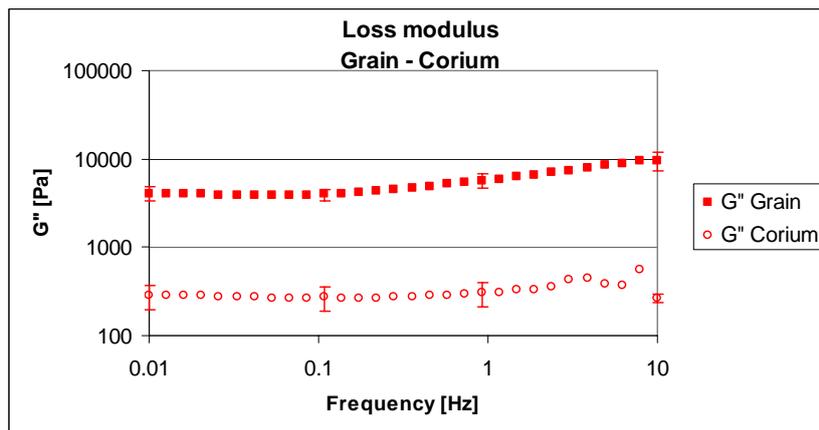
fig. 5 Grain and corium loss modulus. Untreated samples.
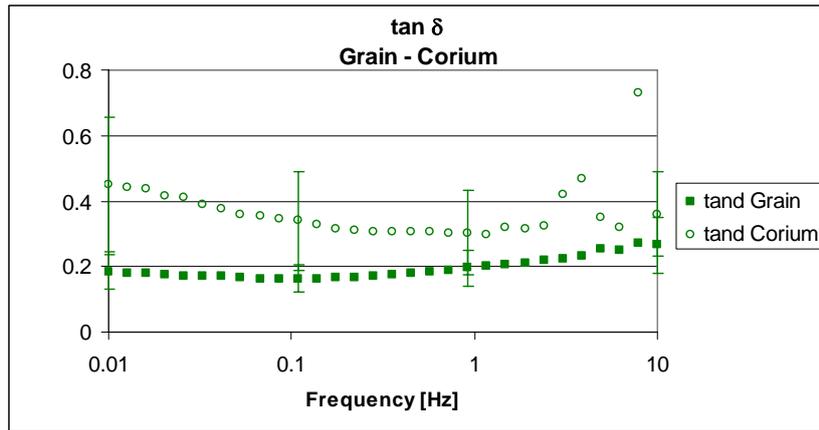
fig. 6 Grain and corium tanδ. Untreated samples.

The G' and G" spectra of both trypsin treated corium (hollow circles) and corium control (solid dot) are depicted in the following diagram
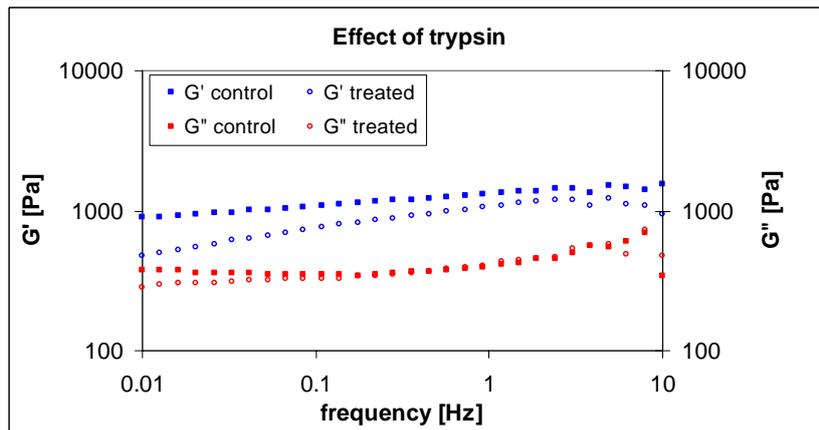

fig. 7 G' and G" curves of trypsin treated corium samples and corium control.

A decrease in the storage modulus is evident for treated samples at low frequencies (below 0.1 Hz). In particular storage modulus evaluated at 0.01 Hz is 47% lower after enzymatic treatment. ANOVA test applied to all the G' values collected from treated and untreated samples shows that at 0.01 Hz the moduli are significantly different ($p < 0.09$). However the "through-the-samples" variance is still a considerable part of the total variance. No significant differences are observed for the G" data.

The stress relaxation moduli of two corium samples are reported in fig. 8. These samples display very different relaxation behaviour. The relaxation of Sample 1 approaches a limiting value (barely above 1 kPa) but no further relaxation phenomena are observed in the monitored time interval. Sample 2, in turn, relaxes quickly and its relaxation modulus does not display any limiting value. Beside this broad variation of the

relaxation curves, it seems that trypsin treatment does not induce any effect on the relaxation modulus since the two curves are practically overlapped.
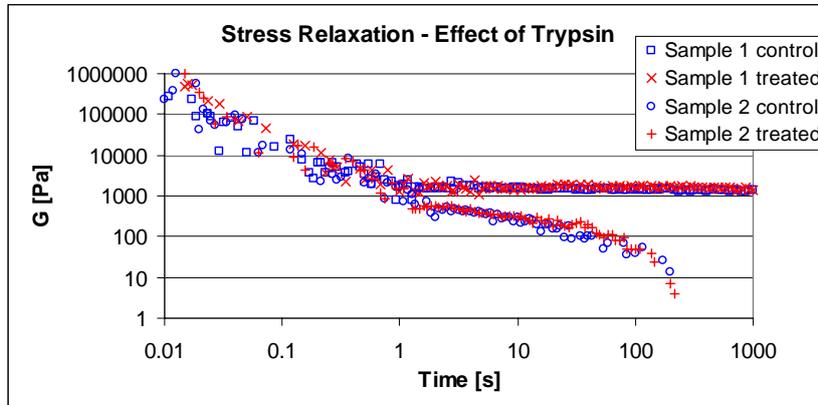

fig. 8 Stress relaxation modulus of trypsin treated and control samples.

The digestion of the elastic network produces a decrease in the mechanical behaviour of grain samples. Both G' and G" plots undergo a downward shift after treatment with elastase as depicted in fig. 9.
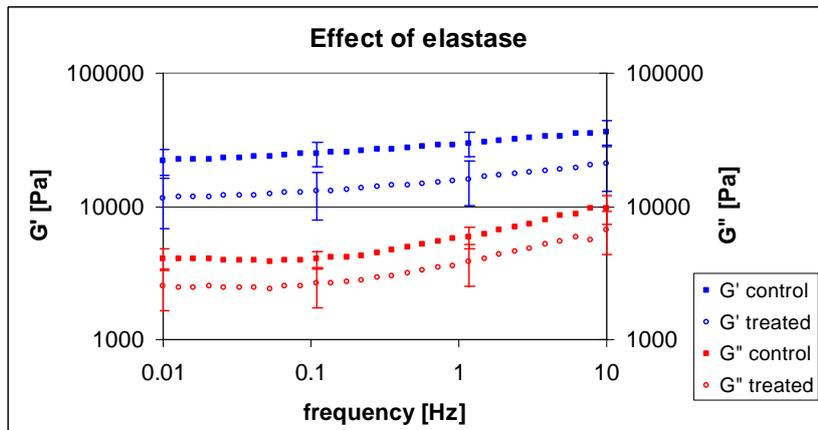

fig. 9 G' and G" curves of elastase treated grain samples and grain control.

However the changes in loss modulus are lower than the changes in G'. Thus elastase treated samples tanδ is always larger than the control all along the frequency range. The average plots of tanδ of treated and untreated samples are reported below.
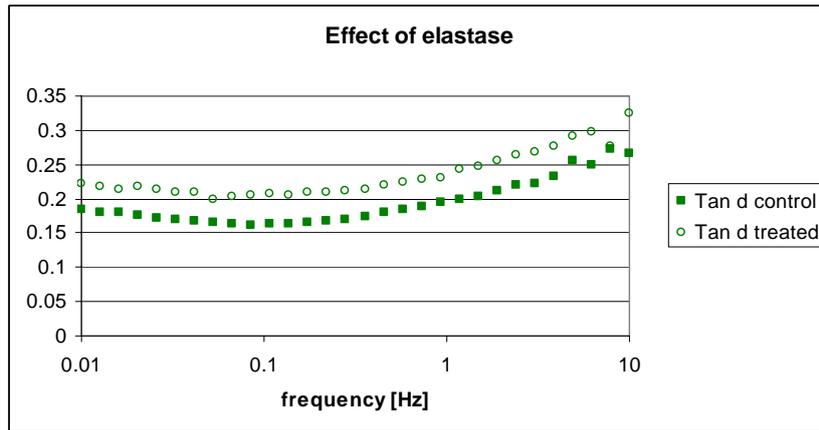
fig. 10 Grain tanδ. Treated and untreated samples.

Treatment with elastase deeply affect relaxation behaviour of grain samples. Treated samples display a relaxation time of 131 ± 96 s while grain control samples do not display any relaxation in the explored time window.
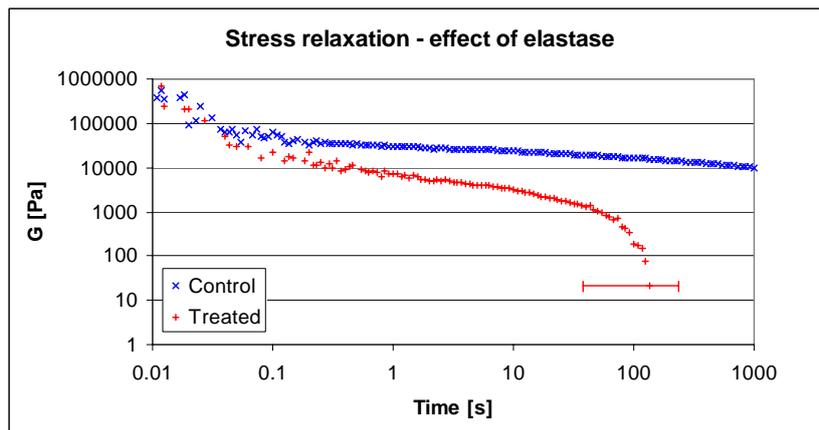

fig. 11 Relaxation modulus of elastase treated and control samples.

Chondroitinase treatment does not seem to produce dramatic changes in viscoelastic moduli, except a small decrease in loss modulus.
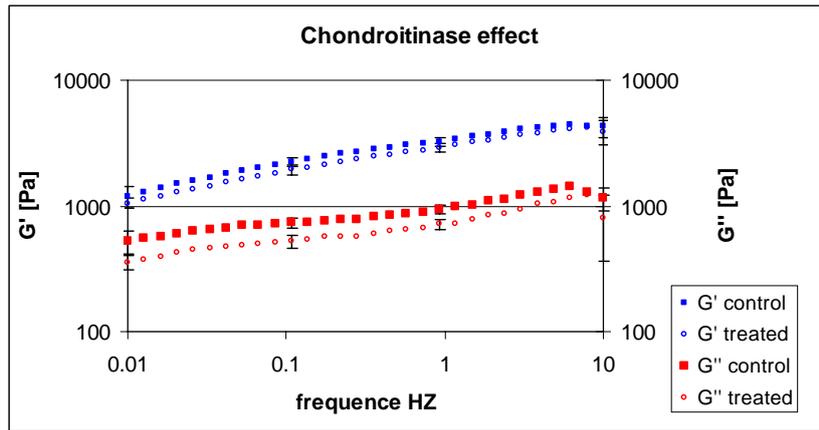
fig. 12 G' and G" plots of chondroitinase ABC treated samples and control.

Dynamic traction tests – Trypsin treatment

Selected stress-strain responses under dynamic cyclic deformation of control skin and trypsin treated sample are reported in fig. 13 and fig. 14 respectively.
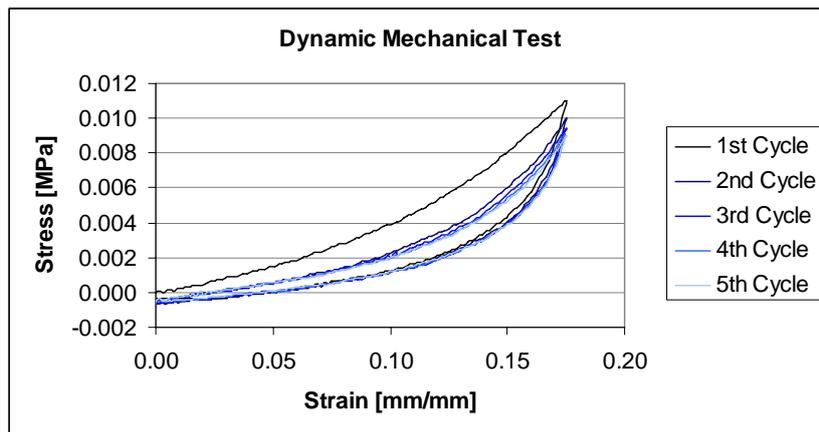

**fig. 13** Dynamic stress-strain plot of kid skin
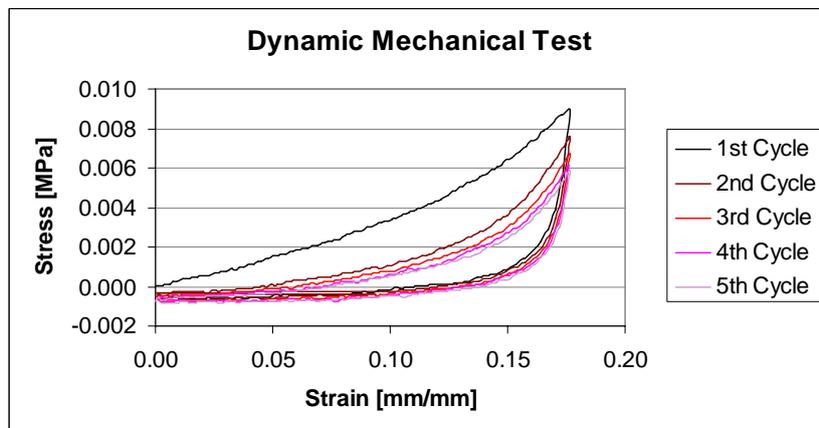
fig. 14 Dynamic stress-strain plot of trypsin treated kid skin

The effect of preconditioning (i.e. the adaptation of the tissue on the external applied stress) is evident. The maximum stress achieved at each cycle decreases with cycle

47

number up to a steady state. Preconditioning effect is enhanced in treated samples. The evolution of the stress-strain response could be conveniently described by the following parameters:

- Starting modulus (E_i), defined as the slope of the linear interpolation of the loading curve in the 0 – 5% strain range.
- Recoil modulus (E_b), defined as the slope of the linear interpolation of the unloading curve in the 16.5 – 17.5% strain range.
- Permanent set (ε_p) is the strain at zero stress in the unloading curve.
- Peak stress (σ_M) is the maximum positive (traction) stress attained at each cycle.
- Hysteresis is the area between loading and unloading curves.

These parameters vary with the loading-unloading cycles, as depicted in following bar diagrams.
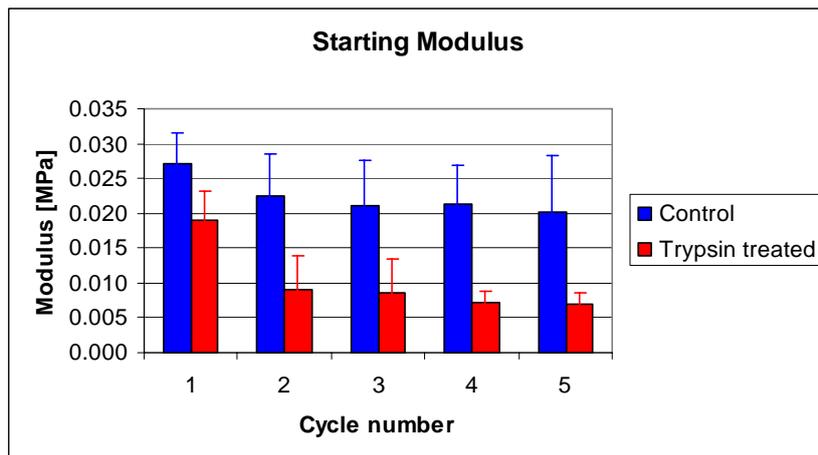

fig. 15 Goat skin starting modulus before and after trypsin treatment.

The starting modulus of control samples is always higher than treated samples one. The difference between treated and control moduli is enhanced after the first cycle. On an average basis, control E_i is 30% higher in cycle 1 and 60% in the following. Starting modulus reaches a constant value after cycle 1 for both control and treated samples.
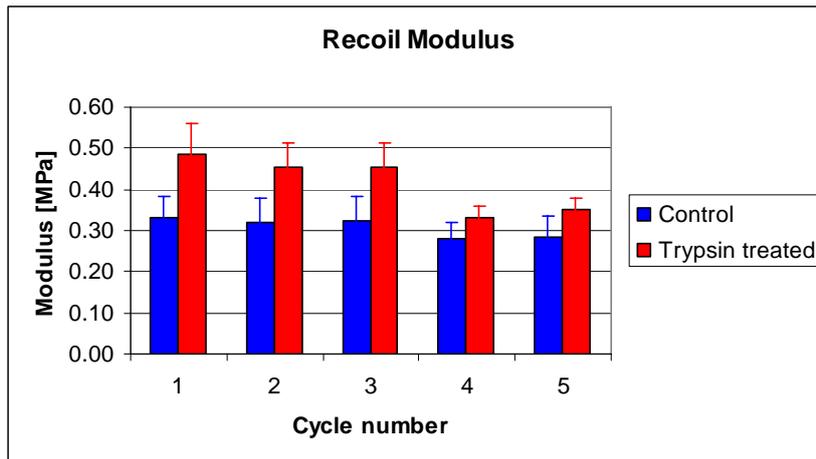
fig. 16 Goat skin recoil modulus before and after trypsin treatment.

Recoil modulus of treated samples is always higher than the control. This means that the stress-strain response of treated samples returns to a zero stress state more quickly. Recoil modulus of control samples is roughly constant with deformation cycles, while for treated sample it attains a higher value in the first three cycles.
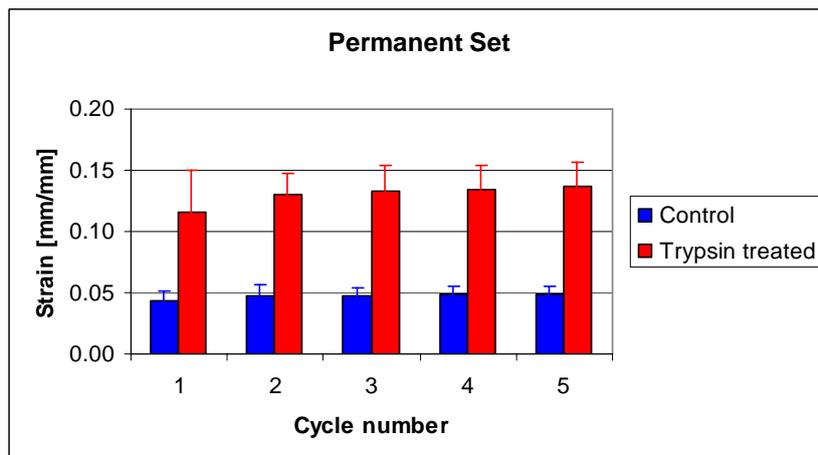

fig. 17 Goat permanent set before and after trypsin treatment.

The residual permanent deformation of treated samples is always significantly higher than the control. The span between the two typologies remains constant with deformation cycles.
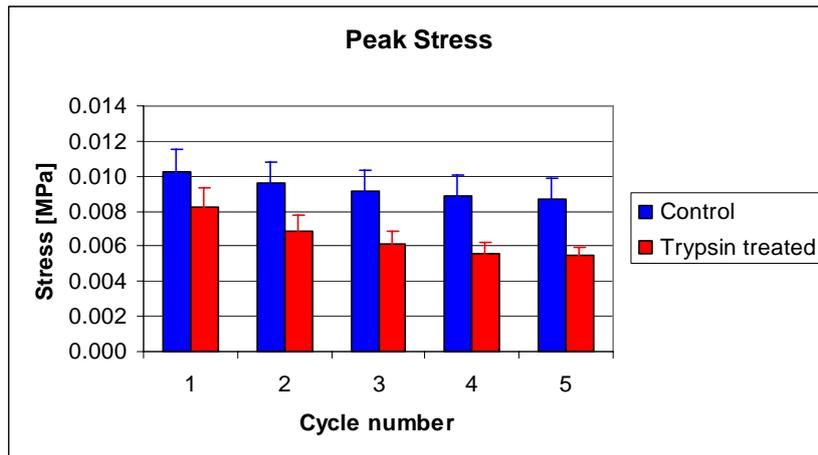
fig. 18 Goat skin peak stress before and after trypsin treatment.

Control peak stress is always higher than that displayed by the treated samples. The difference between control and treated peak stress increases with cycle number, i.e. 25% in cycle 1 and 60% in cycle 5, on an average basis.
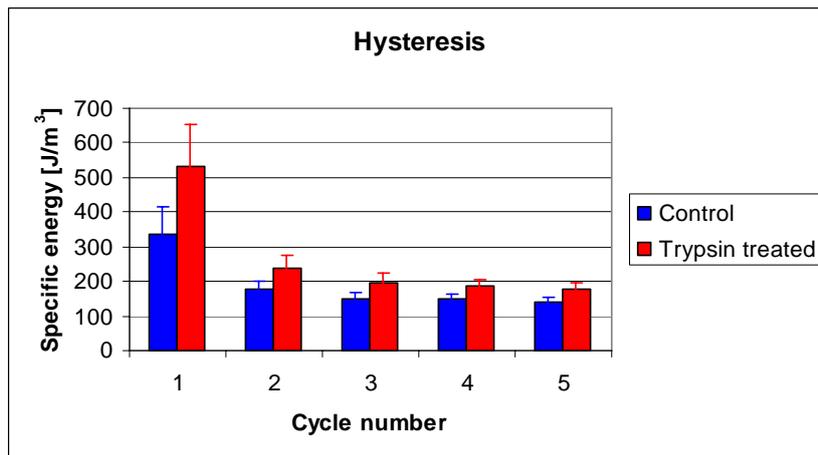

fig. 19 Energy loss before and after trypsin treatment.

As stated earlier, hysteresis represents the specific energy absorbed in a complete cycle of loading and unloading and is represented by the closed loop of the stress-strain curves during a loading-unloading cycle. The hysteresis experiences a dramatic drop after the first cycle and then it reaches a constant value, for both control and treated sample. In particular, the accomplishment of the first deformation cycle for trypsin treated samples damps a considerably higher energy content than for the control.

The enzymatic treatment has extracted about the 45% of the total GAGs detected by the Blyscan[©] assay as schematically shown in the following br diagram.
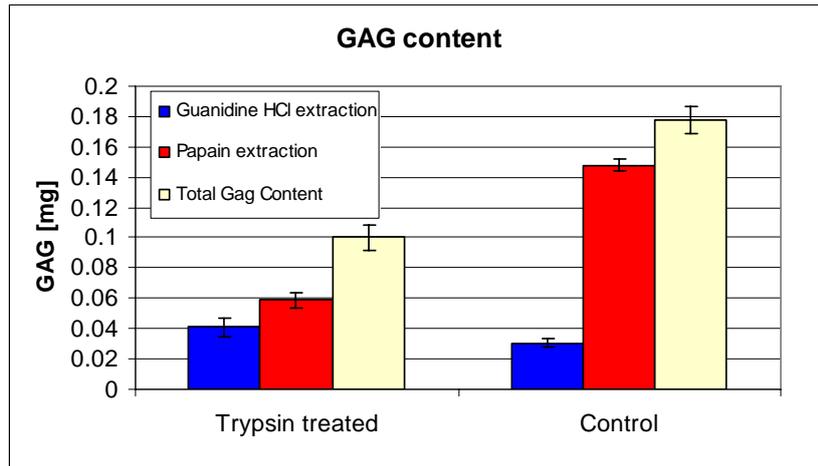
**fig. 20** Kid skin GAG content before and after enzymatic treatment.

Dynamic traction tests – Elastase treatment

Selected stress-strain responses under dynamic cyclic deformation of control skin and elastase treated sample are reported in fig. 21 and fig. 22 respectively.
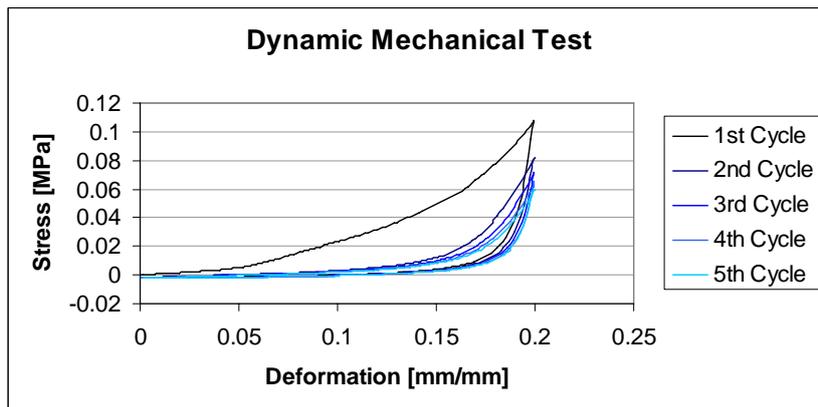

**fig. 21** Dynamic stress-strain plot of kid skin
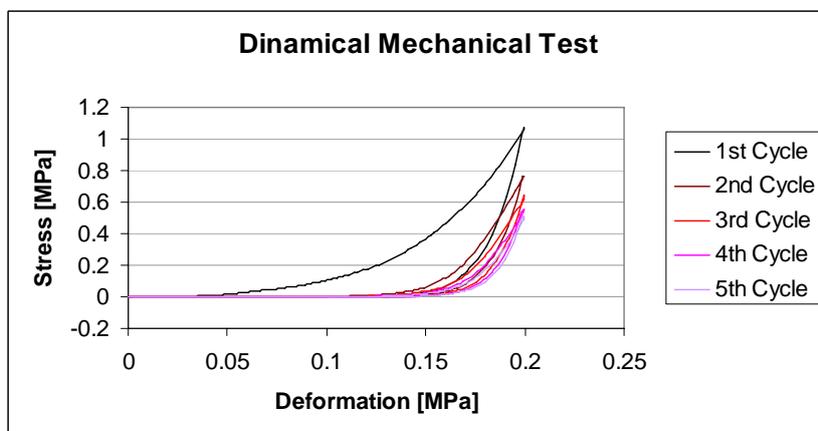
fig. 22 Dynamic stress-strain plot of elastase treated kid skin

The evolution of the mechanical response with the loading cycles will be described with set of parameters already defined in the case of trypsine treated samples, namely starting modulus, recoil modulus, permanent set, peak stress and hysteresis.

These parameters vary with the loading-unloading cycle, as depicted in following bar diagrams.
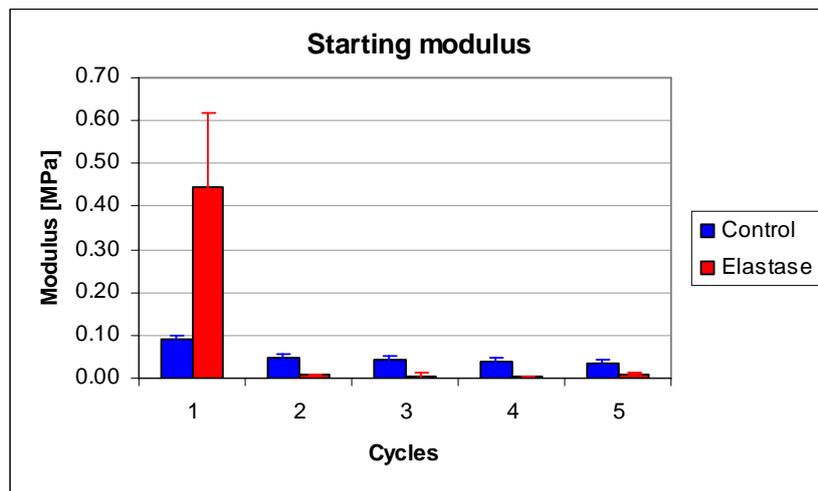
fig. 23 Goat skin starting modulus before and after elastase treatment.

The starting modulus of treated samples is (on an average basis) 5 times higher than the control one in the first loading ramp. From cycle 2 up to cycle 5 the starting modulus of treated samples is significantly below the control.
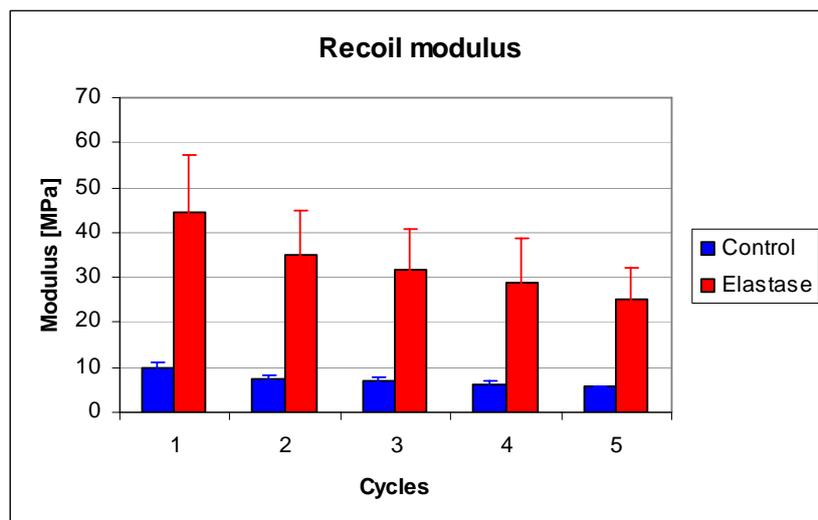
fig. 24 Goat skin recoil modulus before and after elastase treatment.

Recoil modulus of treated samples is always higher than the control. The average value of E_b decreases with loading cycles, for both control and treated samples. However

the rate of decay of E_b is almost the same for both control and treated samples, being the recoil modulus of treated sample constantly 4.5 times higher than the control.
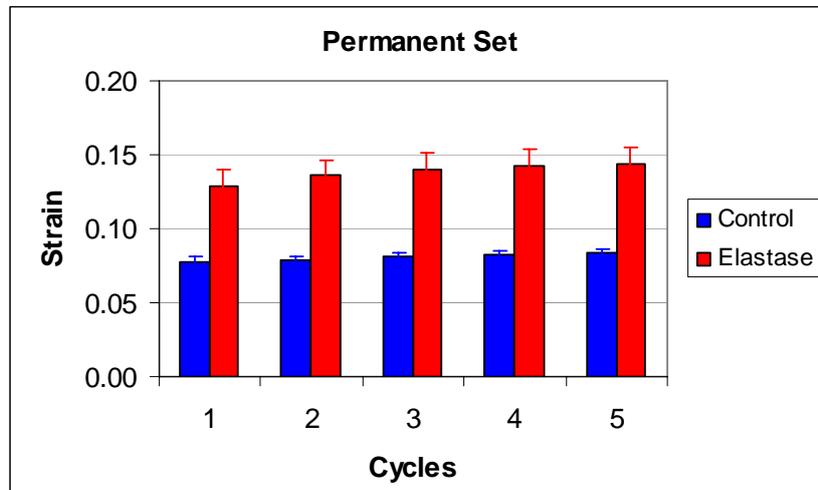
fig. 25 Permanent set before and after elastase treatment.

Residual permanent deformation of treated samples is always significantly higher than the control. The average value of ε_p remains constant throughout loading cycles, either for control and treated samples.
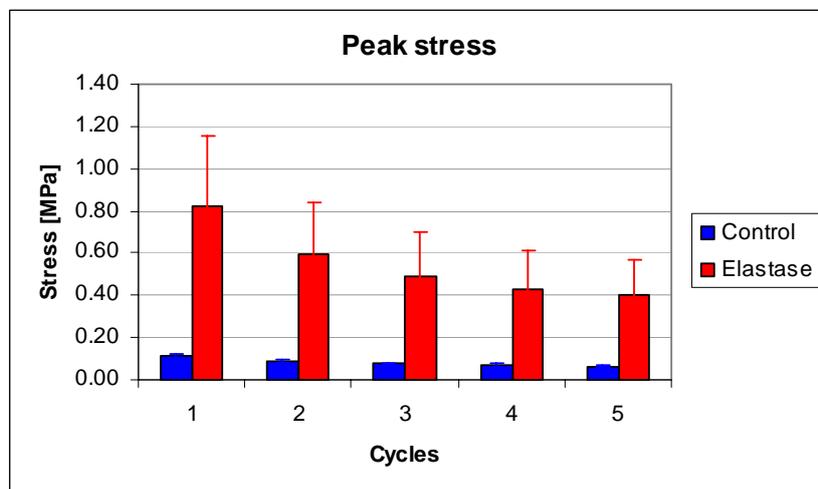
fig. 26 Goat skin peak stress before and after elastase treatment.

The evolution of peak stress displays a similar behaviour to the recoil modulus one, i.e. peak stress of treated samples is always significantly higher than the control.
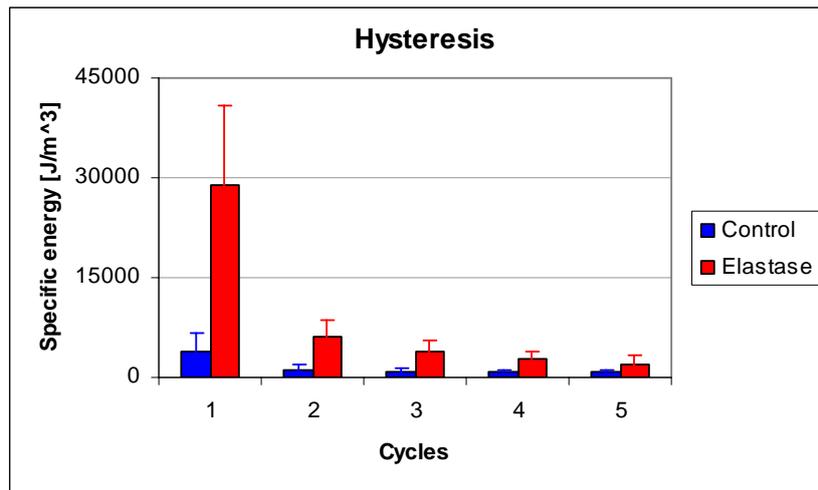
fig. 27 Energy loss before and after trypsin treatment.

Treated samples dissipate a significant larger amount of energy than control in the first four cycles first cycle of deformation ($p<0.05$). No significant differences are observed in cycle 5 ($p>0.05$).

The biochemical assay detects a 20% decrease of the k-elastin content after enzymatic treatment. However a considerable amount of elastin has not been dissolved, which suggests that the elastin is entrapped within the tissue.
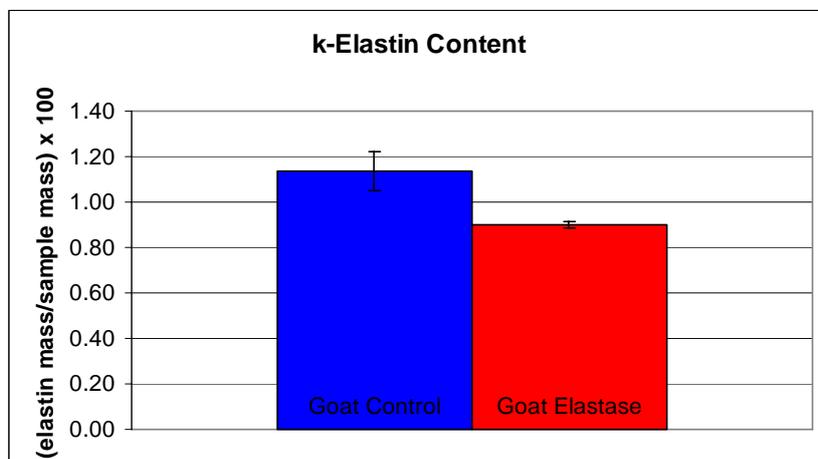
fig. 28 Kid skin elastin content before and after enzymatic treatment.

Differential scanning calorimetry

Selected thermograms (sample C, U, Z and bov) are reported in the fig. 29. The numerical values of onset temperature and peak temperature are shown in tab. 7.
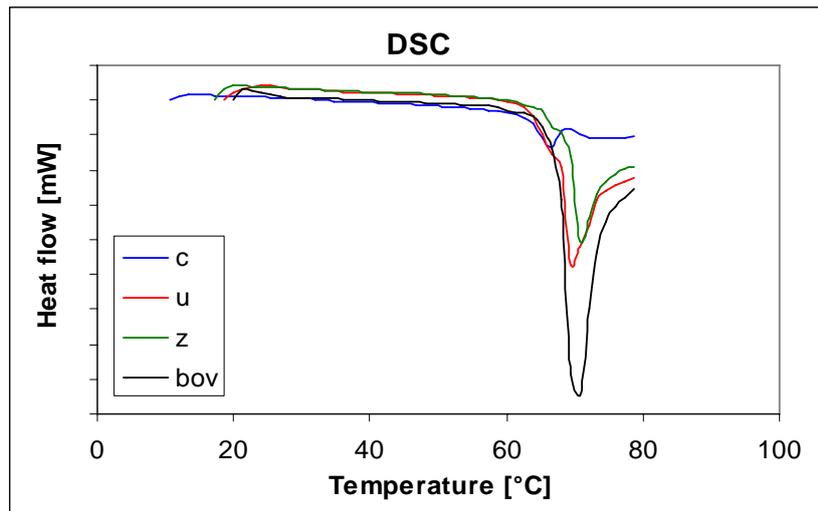
fig. 29 Sample C, U, Z and mature skin average DSC thermograms

|	Peak [°C]		Onset [°C]	
	AVG.	ST. DEV.	AVG.	ST. DEV.
C	66.06	0.09	63.46	0.14
I	67.34	0.47	64.08	0.22
M	66.66	0.44	63.48	0.19
N	67.00	0.13	63.79	0.56
Q	65.47	1.08	63.19	1.63
T	65.80	0.03	63.30	0.80
U	68.57	0.30	64.00	0.15
Z	69.83	0.40	65.18	0.46
bovine	69.22	0.04	67.03	0.20

tab. 7 Skin thermal properties evaluated with DSC experiments

Large endothermic peaks are present around 60 - 70°C which are indicatives of collagen thermal denaturation. The energy involved during the denaturation process, i.e. the area between the baseline and the peak, is much higher for adult tissue rather than for foetal one. Moreover the thermogram of the aldult specimen is more symmetric and regularly defined. Foetal thermograms usually display an early shoulder.

Hydrothermal Isometric Tension

Typical HIT diagram is shown in the figure below.
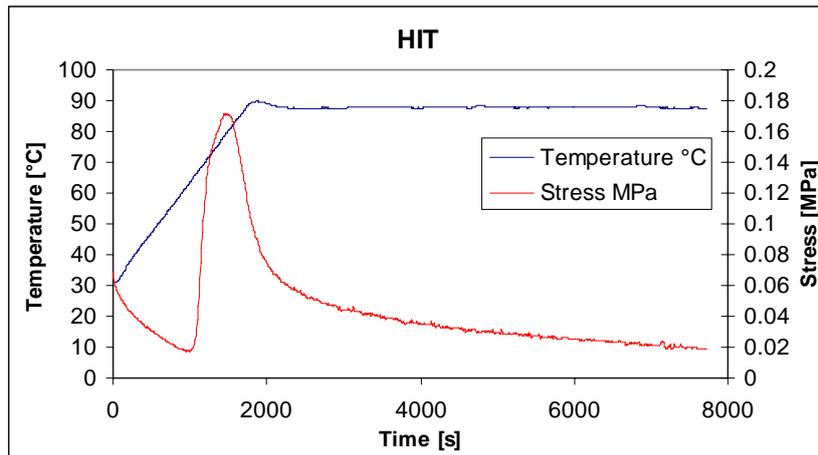
fig. 30 Sample U HIT profile

Stress and temperature are linked by the variable time. It is therefore more convenient to plot stress as a function of temperature.
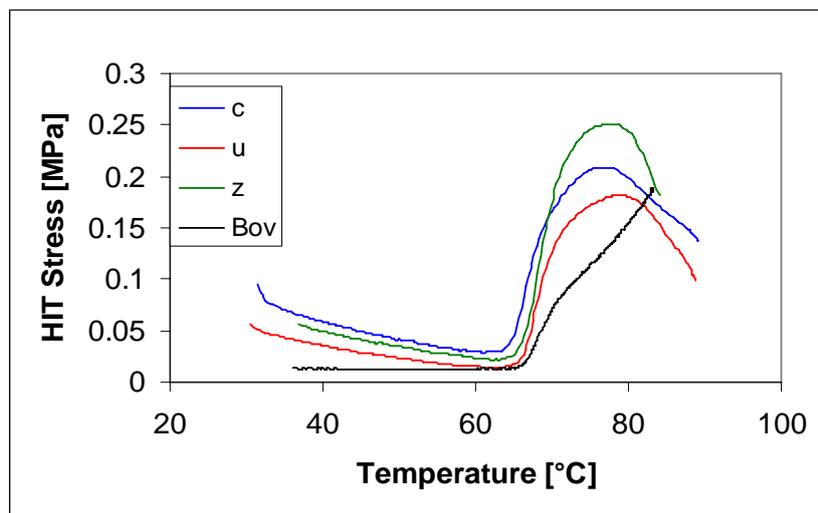
fig. 31 Sample C, U, Z and mature skin stress-temperature plot

A rapid increase in the stress follows the collagen denatuation. Foetal thermograms invariably show a maximum after denaturation. Mature skin thermogram in turn does not display any stress relaxation as the temperature increases.

4. Discussion

The mechanical behaviour in uniaxial tension of both skin and chrome tanned leather is non linear. At small strains (i.e. low stress) the slope of the curve is shallow. For larger deformations, the stress strain relationship becomes nearly linear. The early mechanical response is mainly governed by the ground substance and elastin properties. Collagen fibres begin to uncrimp in the toe region, thus increasing their ability to withstand tensile load. This mechanism is usually referred to as fibres recruitment. The recruitment process is affected by the spatial arrangement of collagen fibres: higher fibre dispersion around load axis causes extensive recruitment and then a larger toe region. At large deformations, almost all fibres are fully stretched and oriented towards the applied load. The linear part of the stress-strain diagram reflects the mechanical properties of fibres.

Several collagenous tissues display a non-affine deformation mechanism under specific testing condition [15]. In particular, the non-affine motion of collagen fibres in pig skin under compression has been attributed to non-affine relationship between fibres and the ground substance [16]. However leather is not a truly composite material since almost all the non-structural proteins are removed during the tanning process. For such material affine deformation hypothesis could be still applied [17]. The deformation mechanism of leather at low strain values has been studied by Wright *et al.* [18]. They have suggested that, on a microscopic scale, the dominant mode of deformation is fibril flexure rather than individual fibril stretching.

If the data depicted in fig. 3 are plotted in terms of displacement and load, it appears that the natural tissue is the strongest (fig. 32).
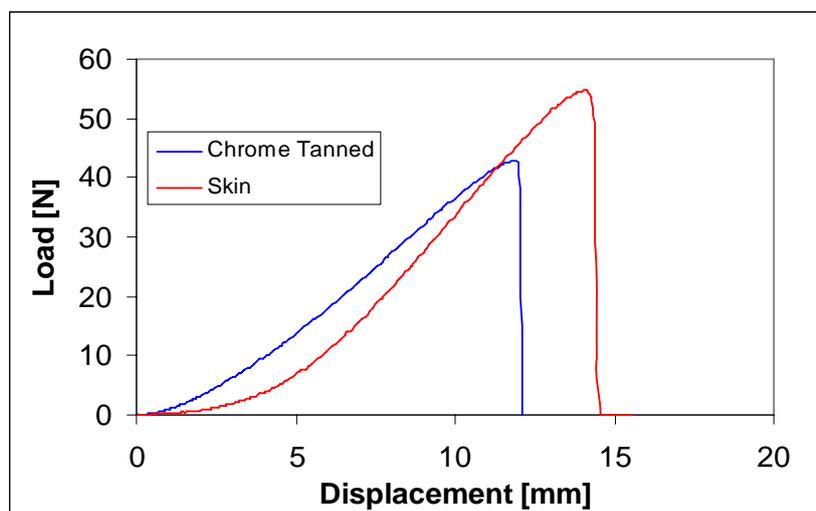

fig. 32 Sample N load-displacement plot

The differences in the two figures mainly arise from the difference in the cross sectional area of the two materials. The swollen skin cross sectional area is greater than the leather one. The load bearing fibres concentration is then decreased in the natural tissue in a water swollen state, i.e. a smaller value of the tensile stress, in terms of MPa, is attained dividing the load by a larger cross section. The presence of a liquid phase among collagen fibres also affects the mechanical properties in the toe region: aqueous solution could push the fibres apart increasing the so called "angle of weave" and therefore the recruitment process is delayed; moreover its lubricant action could decrease the load transfer. During the tanning process the natural tissue is damaged up to a certain extent, especially during liming and pickling. In these process steps, skin is exposed to extreme values of pH, ranging from 12.5 down to 3.5 which can cause a certain extent of hydrolysis. Such weakening effect it is not balanced by the action of chromium, which does not act as a mechanical crosslink [19].

Skin, as well as leather, is an anisotropic material. Mechanical properties are strongly dependent on the sampling position and the direction of applied load, as it shown in fig. 33, where the stress-strain response of the one foetal leather in two mutually orthogonal direction of applied load is reported.
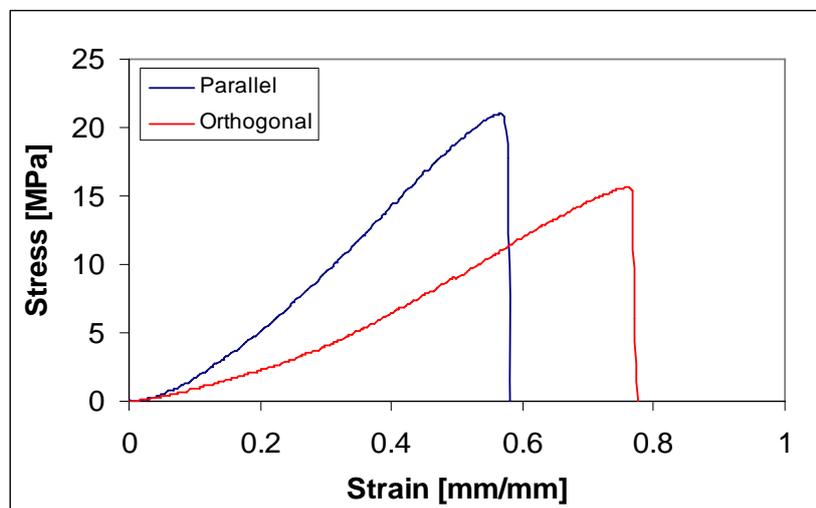

fig. 33 Sample N stress-strain plot in two mutually orthogonal direction of applied load

The recruitment phase is delayed, suggesting that the collagen bundles have been seeded, even in the foetal stage, in a preferential direction. Linear modulus is significantly different which states that different amount of fibre bundles are involved during the deformation mechanism.

Mechanical behaviour is dramatically affected by the sampling position. Foetal calf skins are small (less than 1m^2) and physical properties between two adjacent parts can be significantly different. Results of mechanical tests are always a compromise between two competitive factors: 1. having a statistically significant number of specimen to test; 2. the test itself should refer to comparable materials, since leather is locally non-uniform to a considerable degree [20]. As an example, samples taken away from different zones of Chrome tanned foetal calf leather Sample H have been tested, in the same way as described above. Details on the sampling position are shown in fig. 34 and tab. 8.
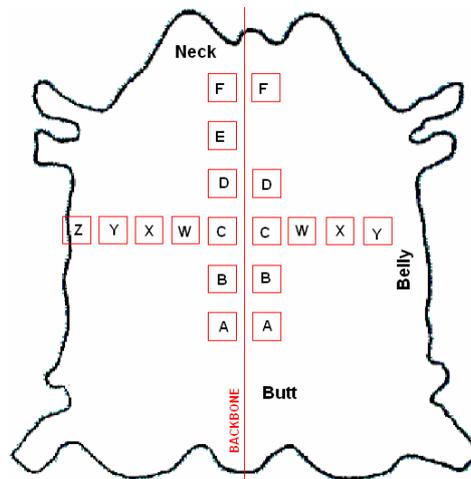
fig. 34 Sample H sampling position schematic

Position	Left hand side		Right hand side	
	Distance from the neck [cm]	Distance from the backbone axis [cm]	Distance from the neck [cm]	Distance from the backbone axis [cm]
A	60	3.5	60	4
B	50	4	50	5
C	40	5	40	5.5
D	30	4.5	30	5.5
E	20	5	-	-
F	10	5	10	6
W	40	11.5	40	12
X	40	17	40	18
Y	40	22	40	23
Z	40	28	-	-

tab. 8 Sample H sampling position distances

The values of the modulus in both the directions parallel and perpendicular to the backbone, are shown in the following bar diagrams.
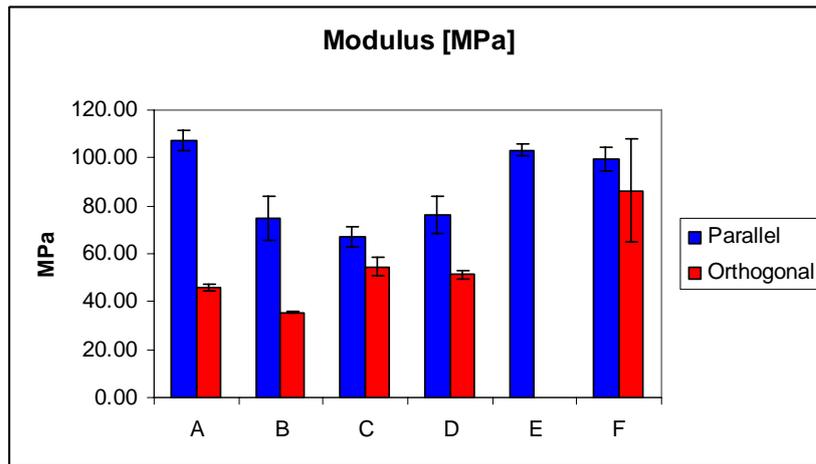
fig. 35 Sample H linear modulus along the backbone
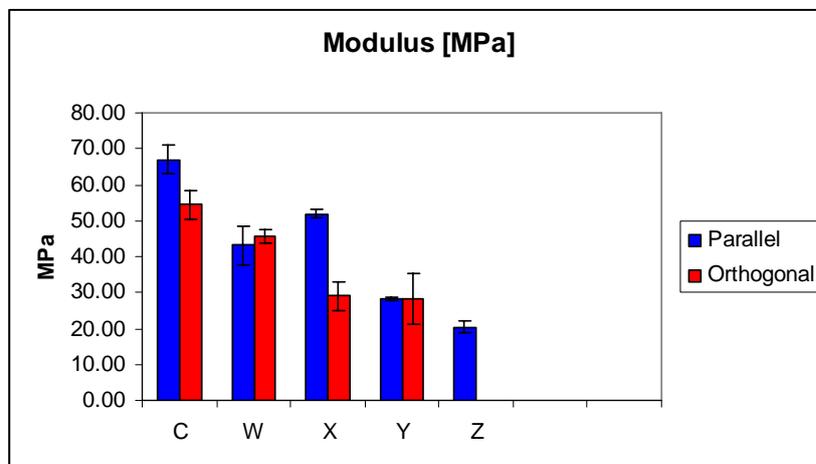
fig. 36 Sample H linear modulus across the backbone

The top diagram suggest that, following the backbone length, the collagen fibres in position A and E posses higher modulus; and those fibres are in proximity of the pelvic and thoracic girdle respectively. Osaki suggests that collagen fibres in skin are mostly aligned in the direction parallel to the back bone and limbs. These direction corresponds to the direction "perpendicular to that of skin motions accompanied with muscular motions in the abdomen and hindlimbs due to eating and walking, and that the degree of orientation was large in the parts where the skin motions are marked" [20]. Moving away from the back bone (bottom diagram) linear modulus becomes smaller. Samples with comparable values of both moduli (positions F, W and Y) probably are made: 1. of fibers prevalently aligned in a direction tilted of 45° respect the backbone axis; 2. the material itself is planar isotropic.

These results pertain the anisotropic behaviour in the plane of skin. The anisotropy arises from a preferential spatial arrangement of the fibres within the structure, i.e. there exists a population of fibre bundles oriented with respect to the same direction. However,

electron micrographs clearly show that the skin (as well as leather) cross section possesses structural heterogeneities as shown in fig. 37.
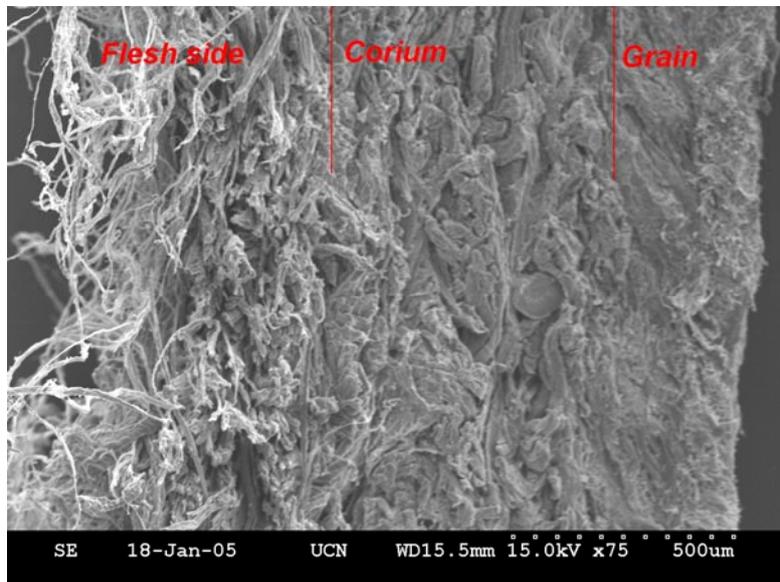
fig. 37 SE micrograph of a foetal calf leather

Dermis multilayered structure here depicted is evident: the corium layer is an entangled mass of thick bundles and the grain, is composed of a network of thin fibres.

Besides structural heterogeneity, ECM composition presents gradient throughout the thickness. The elastic network is an example, as it is confirmed by the optical micrograph of a foetal calf cross section stained with orcein red shown below (fig. 38).
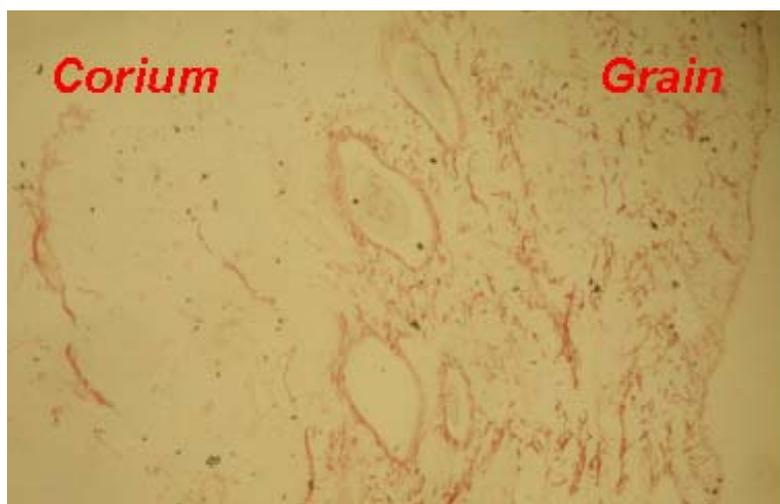
fig. 38 Foetal hystochemical stain for elastin network

As it is shown, the elastin is not spread all over the leather thickness, but it is present in the grain side and all around the hair follicules. Since the elastin content in skin is modest

and owing to its weak mechanical behaviour [21] it is unlike to affect the static properties of both leather and skin at finite strain.

In fig. 39 starting modulus is plotted against dermal elastin content. It seems that exists a correlation between the two parameter, i.e. a tenfold increase of the elastin content produces almost a fourfold increase of the starting modulus.
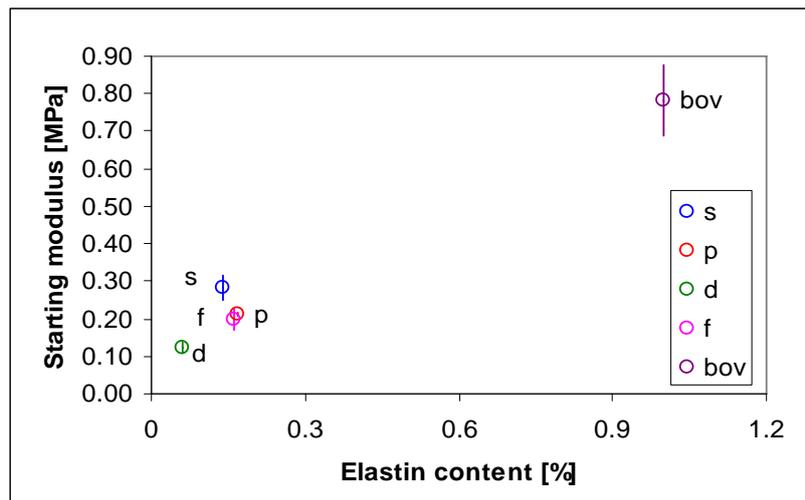
fig. 39 Starting moduls – elastin content plot

As state earlier, it is unlike that the elastic network is the only responsible for the early tissue mechanical response. Bending stiffness of mature collagen fibre bundles, as well as interaction between the ground substance and the fibre network could play non negligible effects. During the foetal stage, however, collagen bundles are thinner and fibrillar in nature as confirmed in the following two electron micrographs.
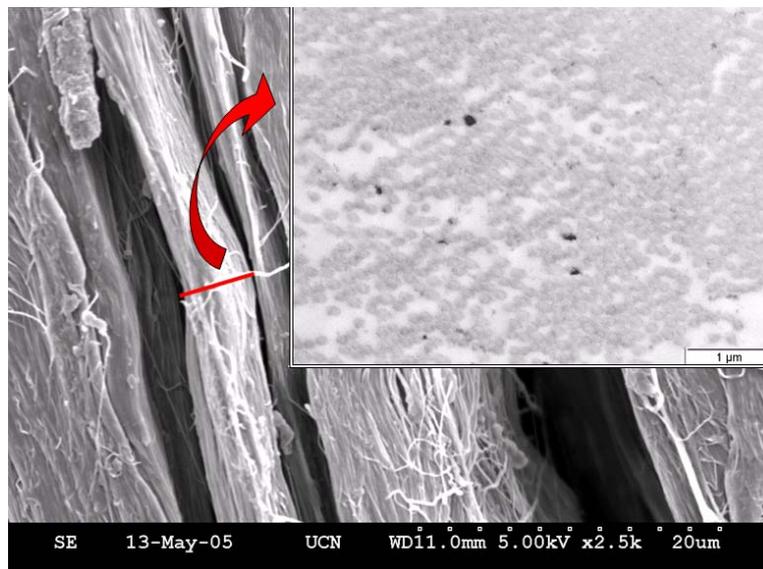
fig. 40 SE micrograph of foetal calf leather. Top right: TE micrograph of a foetal collagen fibre bundle

It is possible to assume then, that the bundle bending stiffness is negligible, or, at least, it roughly induces comparable effects for all the foetal skin tested. Thus the relative influence of the elastic network on early mechanical response is higher and this assumption could explain the correlation between elastin content and starting modulus in the foetal stage. The role of ECM macromolecules on the macroscopic mechanical properties of a connective tissue is, however, not thoroughly recognized. It is believed that non collagenous proteins have non negligible roles at low strain as well as on the tissue viscoelasticity, while collagen bundles determine the tissue mechanical response at large strain.

Loose connective tissues can indeed be modelled as a composite material where collagen fibres are embedded in a matrix which is made viscoelastic by the presence of a wide range of proteins, sugars and proteoglycans. In the past decades, the attempts for studying connective tissue viscoelasticity and relationship between mechanical properties and structure have often involved selective enzymatic digestion of matrix components [22, 23, 24]. One of the largest issues that has to be taken into account in biological (native) tissues testing, is the great variability among specimens. In particular, mechanical properties are affected by large errors especially when finite deformation are applied. This variability could mask the effects of enzymatic treatments making them virtually impossible to discern. Thus the potency of such enzymatic treatments still remains questionable. However, the experimental set up previously described has the advantage of avoiding the poor reproducibility of the biological tissue mechanical properties since it involves very small oscillating deformation. Moreover, rheological experiments give a complete description of the viscoelastic properties.

As previously stated, the structure and the composition of grain and corium differs significantly. G' and G" spectra of both corium and grain suggest that these materials possess viscoelastic properties closely related to polymeric gels where G" is lower than G' and both of them are roughly constant with frequency. However grain seems somehow stiffer than corium (fig. 4). This is a consequence of the closely packed structure of grain which is composed of short and thin collagen whiskers entrapped in the three dimensional elastin crosslinked network, rather than the loose mass of entangled bundles of the corium. This observation is in agreement with the grain and corium $\tan\delta$ plot. Even though $\tan\delta$ does not convey any physical magnitude, it is a measure of the ratio of energy lost to energy stored in oscillatory deformations. At low frequency (< 0.1 Hz) corium loss tangent

is higher than grain tanδ. In this particular frequency range some macromolecular movements are activated which allow relative gliding of loosely packed collagen fibrils.

The load bearing collagen network resists dynamic deformations only if its (characteristic) relaxation time is longer than the reciprocal of the applied frequency.

Removal of fibril associated proteins and proteoglycan cause the elastic modulus to be reduced by half at low frequency. According to the model of Puxkandl *et al.* [25] such macromolecules branch off the fibrils and intertwine with other macromolecules attached on adjacent fibrils. Such branching introduces physical crosslinks which transfer load from fibril to fibril, thus stiffening the whole network. If the deformation frequency is sufficiently low, fibrils have time to disentangle the physical constraints and can move with each other. The experimental results previously reported are in agreement with the findings of Kronick and Sachs [26] and show that fibril motion is sensitive to matrix composition and it has been found to be enhanced when interfibrillar proteins are removed by trypsin. The enzymatic effect vanishes at higher frequency. Under this condition the large collagen fibrils have little time to reorient and are forced to move in concert. The presence of non fibrillar macromolecules does not seem to affect this motion. Moreover trypsin treatment is more efficient than the Chondroitinase one, since the former is expected to chop the proteoglycan off the fibril via core protein cleavage, while the Chondroitinase releases just the GAG sidechains, yet preserving the core protein and interfibrillar proteins.

Elastic fibres form a three dimensional crosslinked network spread all over grain thickness. Elastin seems to affect profoundly the viscoelastic behaviour of skin, even though it comprises about 1-2% of skin wet weight. Elastic network holds the collagen fibrils wrapping them around [24] and relative movement of collagen bundles results thus hindered. The digestion of the elastic network creates additional freedom for the collagen fibres to glide past each other, which is related to a drop in G' and G" (fig. 9). The effects of elastase treatment are even more evident on the skin relaxation behaviour. Control samples do not show any relaxation in the time window explored, while the treated samples relax. The plateaux modulus of treated samples is lower than the control one, which is consistent with the results provided by the oscillatory experiments. Dynamic measurements at a frequency ω are indeed equivalent to a transient one at $t \approx \frac{1}{\omega}$.

Dynamic modulus spectrum is approximately the mirror image of relaxation plot reflected in the modulus axis. On the other hand, the digestion of interfibrillar matter using trypsin do not affect the relaxation behaviour whatsoever. As depicted in fig. 8 the relaxation plots of trypsin treated and control samples are practically overlapped. As stated earlier, matrix

proteoglycans and interfibrillar proteins induce a stiffening effect on the collagens structure at low frequency. This effect arises from physical interaction (entanglements, hydrogen bonds and other non-covalent bonds) of fibril attached macromolecules. These results suggest that interfibrillar proteins affect low frequency storage modulus, but are not able to drive an elastic recoil of a distorted network. Once the interfibrillar reticulum is irreversibly disentangled, it cannot exert its stiffening effect on low frequency mechanical properties, which is consistent with the results provided by the dynamic traction tests (see below). The different plateaux value should be ascribed to differences in sample structure rather to the enzymatic treatment itself. Probably the sample which displays a higher plateaux value comprises a larger amount of elastin and/or papillary dermis. However elastin does not differ in terms of relative amount in the different dermal strata, but its assembly is very different in both layers as well. In papillary dermis, the elastin forms a thin branched network which wraps the thin collagen fibres around. This network is mainly composed of microfibrils, containing the rather stiff protein fibrillin [27]. Larger elastic fibres with a predominantly highly crosslinked amorphous core transverse the reticular dermis (fig. 41).
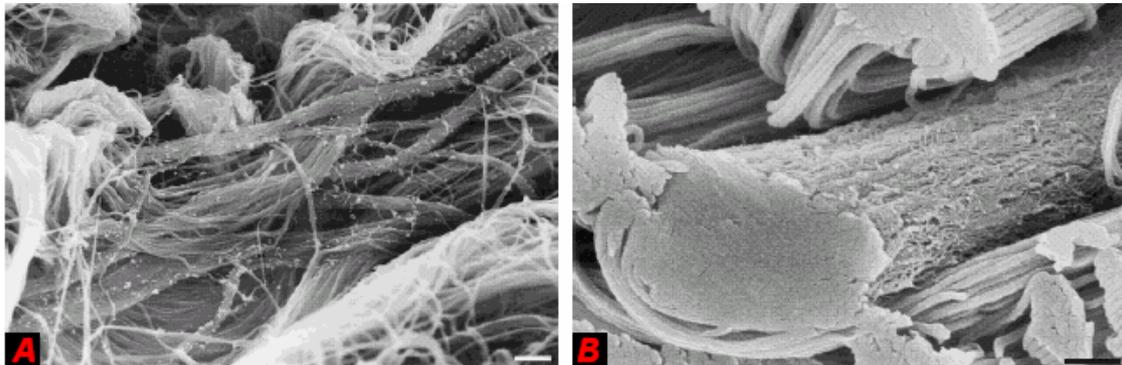
fig. 41 Different assemblies of elastin in papillary dermis, by the DEJ (A) and reticular dermis (B). Modified from Keane *et al.* [27].

This particular difference in the assembly of elastin in the dermis could explain the stiffening effect that elastin network exerts on papillary dermis and its efficiency in constraining individual collagen fibres to move past each other and allowing elastic recoil.

The role of ECM macromolecules on the mechanical response at low frequency, large cyclic deformation could be quite different from the one depicted in the oscillatory low strain test. Collagen rich soft tissues exhibit preconditioning when subjected to cyclic deformations. Preconditioning has been recognized as a viscoelastic property and it basically is a gradual adaptation of the tissue to its applied load. During cyclic (large) deformation, irreversible rearrangements of the tissue microstructure occur. However preconditioning does not involve conformational changes of the ECM alone. At large strain

the inner structure is severely damaged and the extent of damage presumably depends on the maximum stress previously experienced by the specimen, which is a phenomenon known in rubber elasticity as *strain softening*. The preconditioning effect is prominent during the first two cycles then it becomes less evident, as it is clearly visible in the bar diagrams of fig. 15 and fig. 19. These results suggest that the internal structure is severely altered even after the first cycle. Intrinsic modifications could involve rupture and unravelling of proteoglycan and interfibrillar reticulum, uncrimping and gliding of collagen fibres. No more changes occur unless a new higher value of stress is attained. The role of interfibrillar proteins in regulating tissue preconditioninig is confirmed with the following observations. Trypsin treated samples display a lower starting modulus (E_i) compared to the control one and this is constituent with the oscillatory experiments in the low frequency range (fig. 7). Proteoglycans and interfibrillar macromolecules form a branched three dimensional network which enhances the load transfer between adjacent collagen fibres, thus stiffening the whole structure. However, after the first cycle, the interfibrillar reticulum is considerably broken down ceasing to exert its mechanical action. Another feature of trypsin treated samples is that they have a considerably higher recoil modulus (E_b) compared to control samples, even though elastin should not be degraded with trypsin treatment. Such result could, at a first glance, be partially misleading if compared to that reported so far, concerning small amplitude oscillatory shear, which indicates that elastin profoundly affects the stress relaxation of skin. At finite strain the recoil mechanism however, could be different. According to Oxlund *et al.* [24] there is not any evidence of direct chemical linking between collagen fibres and elastin. However, Keane and coworkers [28] demonstrated that colloagen type VI forms a branched network which colocalize and it is often mistaken with elastin microfibrils. This observation probably suggests synergic effect of elastin network and branching of interfibrillar proteins which holds the collagen reticulum together, which is consistent with the results provided by Cleary and Gibson [29]. The sharp increase of E_b experienced by trypsin treated samples could be explained in terms of two concomitant factors: damaging of the elastic network caused by the large deformation (probably disentanglement of elastin and collagen); cutting off the elastin-interfibrillar proteins interactions (collagen type can indeed be digested with serine proteases, as trypsin is [31]. The hypothesis of reduced elastic recoil of trypsin treated samples is consistent with the experimental evidence of the increase of permanent set value and energy loss (hysteresis value) compared to untreated samples.

Surprisingly, elastin digestion causes the skin to exhibit an higher starting modulus (in the first loading ramp) and an incredibly higher stiffness in the linear region, and of course an higher peak stress (see fig. 26). Even though it has been previously stated that elastic network governs the mechanical response at small strains, the initial higher modulus in samples devoid of elastin could be explained by the originally crimped and entangled structure of collagen bundles. After enzymatic treatment, collagen bundles are no longer constrained by the three dimensional reticulum of elastin and can uncrimp and align towards the applied load, even at very low stress values. This is hypothesis is consistent with the experimental observation of decreased extensibility of elastase treated samples at constant stress. The deformation of samples at constant stress of 1 kPa with intact elastin is 3.5 ± 0.2%, while it falls down to 1.9 ± 0.4% after enzymatic treatment. These results are consistent with data provided by Oxlund *et al.* [24] and Lee *et al* [12]. After the first cycle the collagen network is severely distorted and has almost completely lost its ability to recover from the superimposed deformation, as shown by the trend of permanent set and recoil modulus (see fig. 24 and fig. 25). Despite the altered mechanical properties displayed by elastase treated samples, the biochemical Fastin® assay still detects a significant presence of elastin. This probably suggests that mechanical disruption becomes evident prior to significant elution of the elastin protein into the digestate. The low elution of elastin has to be ascribed to the high content of tetrafunctional isodesmosine and desmosine crosslinks. The elastin network must thus be cleaved at several positions before it could be solubilized.

As stated earlier, elastin content does not seem to influence dermal ultimate mechanical properties as well as linear modulus. The latter, strictly depends on the stretching of collagen fibre bundles. In particular, it is known that collagen crosslinking density influences collagen fibre stiffness. Calorimetric analyses provide useful informations concerning the amount and nature of the crosslinks present in the tested tissues. Covalent crosslinks, indeed, not only provide the tissue with mechanical strength, but also confer thermal stability. As a consequence of that, thermal analyses are an indirect method for the quantification of crosslink density.

Collagen thermal denaturation occurs around 60° - 70°C, where DSC thermograms exhibits an edothermic peak. In the temperature range mentioned above, the thermal energy is sufficiently to allow the collagen triple helix – random coil transition.
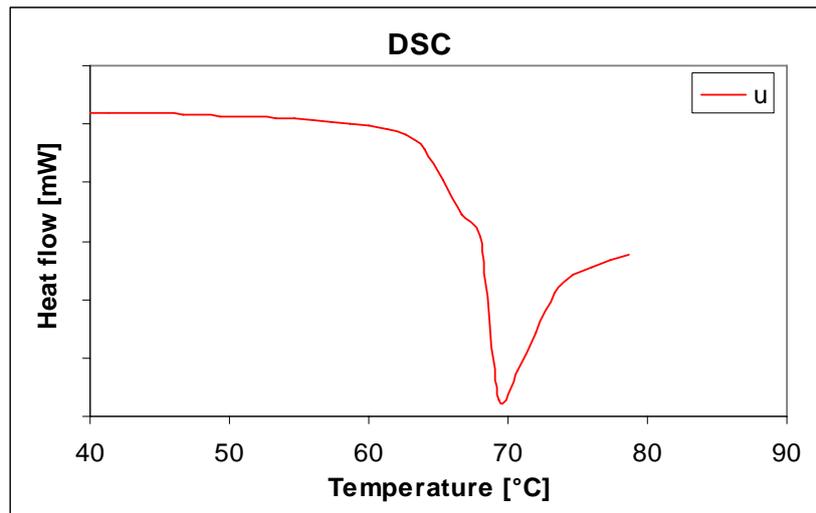
fig. 42 Sample U magnification of the DSC thermogram

In particular, it is supposed that the mechanism of uncoupling of the three α-chains starts in a particular region of the triple helix, called the *thermally labile domain* [30]. This domain is identified in a hydroxyproline free sequence, 65 residues long, nearby the C terminus.

According to the "polymer-in-a-box" model, Miles *et al.* [32] have explained the mechanism of collagen thermal denaturation and the influence of hydration on the thermal stability of collagen. This model assumes that the collagen triple helix is bound in a box, which is the volume available between this molecule and the surrounding molecules.
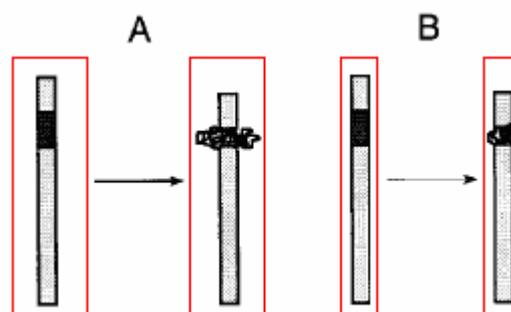
fig. 43 Schematic of the polymer-in-a-box model. From Miles *et al.* [32] modified.

As shown in the schematic model depicted in fig. 43, reducing lateral dimension of the box, by dehydration, will reduce the configurational entropy of activation of the uncoupling of the thermally labile domain and thereby will increase the Gibbs free energy of activation and consequently will stabilize the whole structure. Such a model explains why individual collagen molecules and collagen fibres swollen in acidic solution posses lower denaturation temperature: in both cases the box dimensions are larger compared to the collagen ones and the box itself is no more a constrain for the lateral expansion of the

thermally labile domain. For the same reason, collagen molecules in highly packed structures, such as tendons and ligaments, are very stable. It should be noted that, in fibrils, the thermally labile domain is situated in the gap zone where it has enough space to expand laterally on thermal activation. It is therefore probable that thermal labile domain of the molecule in solution in the same region of the molecule in the fibre and is the region responsible for the collagen instability.

The collagen denaturation peak reported in fig. 42 is strongly asymmetric and non-regularly shaped. A shoulder is usually present 3 – 5°C before the main peak, especially for immature tissues. Such shoulder degenerates in adjacent and smaller peak in few specimens. These observations can suggest that collagen is present in foetal skin in ordered structures, such as fibres and fibre bundles and in oligomers like dimers, trimers, and so on. As said earlier, accordingly to the polymer in a box model, collagen triple helices inside fibrils and fibres, are more stable than triple helices in a soluble form. It has to be noted that collagen in fibres is bound to surrounding molecules by chemical crosslinks, which can induce an additive stabilizing effect. Such an effect is not accounted in the polymer in a box model, even if it is still unclear whether there is a relationship between box lateral dimension and degree of crosslink or not. Soluble collagen does not possess such crosslinks and then can denature more easily involving a lower amount of thermal energy. If the concentration of "soluble" collagen is sufficiently high, the endothermic peak pattern become "bimodal" with the two peaks representing the two different populations of collagens. As an example, sample C is characterized by a relatively low linear modulus value and shrinkage temperature as well (see fig. 29, blue line). This leads to assume that this sample represents an immature tissue, and this is confirmed by the DSC diagram in which the two different population of collagen are present. DSC thermogram of bovine skin supports this hypothesis: denaturation peaks are in this case more regularly shaped.

Hydrothermal isometric tension can provide useful information on the type of crosslinks present in the dermis by measuring their thermal stability. During the HIT test the stress source is mainly collagen triple helix unwinding. During the shrinkage, individual collagen molecules transfer the stress to the surrounding molecules via chemical covalent crosslinks. In natural tissues, a broad spectrum of crosslinks exists. Each type of crosslink is characterized by a certain thermal stability. For this reason heat labile crosslinks can break down as the temperature increases causing the dentured network to relax. Changes

in stress signal are thus the result of two competitive factors: denaturation of triple helices and break down of the dentatured network.

The HIT plot of adult tissue differs significantly from the foetal one. The latter presents a maximum which suggests that foetal collagen molecules are mainly crosslinked with heat labile crosslinks.

Interesting results can be gathered overlapping the HIT curve with the DSC thermogram.
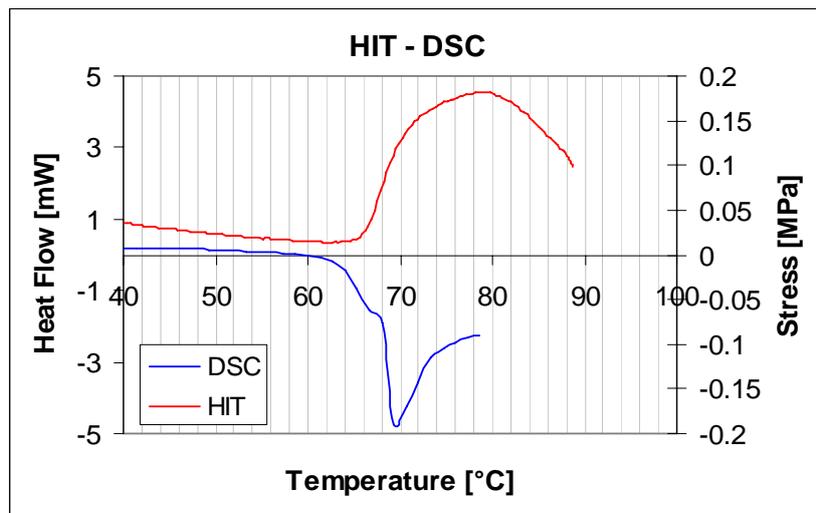
fig. 44 Sample U HIT – DSC profiles comparison

As far as foetal tissues are concerned, it seems that DSC equipment starts to record collagen denaturation slightly earlier than the HIT. This observation is consistent with the hypothesis of the presence of two different populations of collagen molecules in the foetal tissue, i.e. the soluble one which is not constrained by chemical crosslinks, denatures at relatively low temperatures, but since it is not linked to the surrounding molecules, it does not transfer any load and then the HIT does not record any signal. This is represented in the DSC thermogram by an early shoulder. The stress starts to increase significantly when the DSC thermogram becomes steeper. At this point the DSC equipment has to supply higher thermal power in order to denature the crosslinked collagen and up to this point the dominating factor is the uncoiling of crosslinked collagen. After that relaxation phenomena become to be more significant. DSC peak, then, represents the temperature at which thermally labile crosslinks start to break and in correspondence to the peak the HIT exhibits a slight change in slope which reflects that relaxation phenomena begins to occur. After this rupture, collagen molecules are unconstrained and less energy is required for

their uncoiling. This is shown in the DSC profile by a late shoulder after the peak; and in the HIT curve by a shallower curve. HIT profile of mature skin is strongly different.
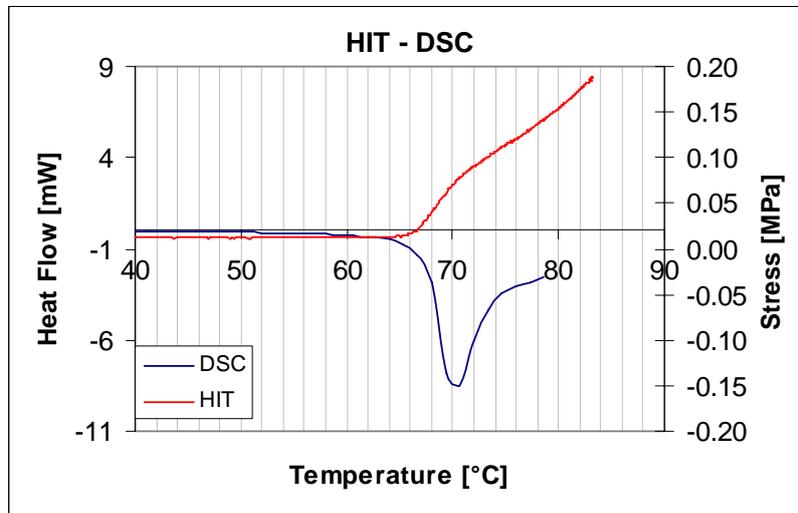
fig. 45 Bovine skin HIT – DSC profiles comparison

Sample shrinkage roughly starts at the same temperature recorded by the DSC which accounts for protein denaturation. Moreover, the DSC profile is more symmetric and regularly shaped, suggesting that mature skin is practically devoided of heat labile crosslinks. Nevertheless a late shoulder is present. In this case, the presence of such shoulder ought to be ascribed to protection mechanism secured by the existence of heat stable crosslinks which prevent the triple helices to unwind.

Starting from these observations a linear modulus dependence on the shrinkage temperature has been found, as shown in fig. 46
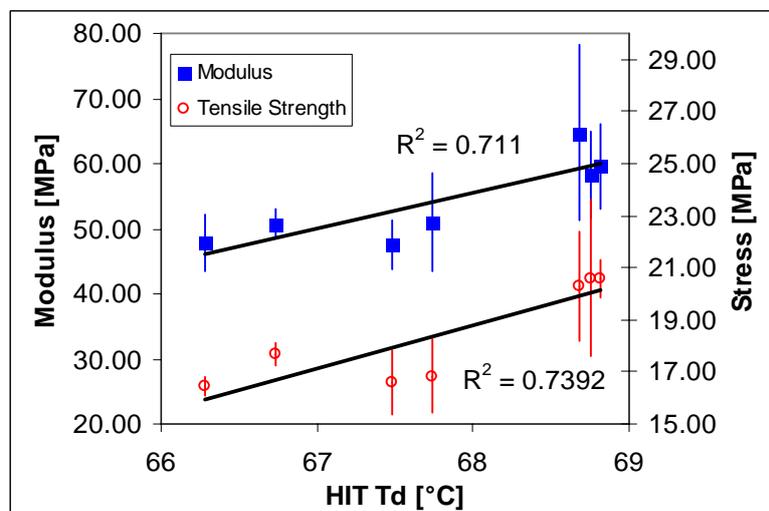
fig. 46 Modulus (solid squares) and Tensile Strength (hollow circles) vs shrinkage temperature

Foetal skins with higher shrinkage temperature posses higher crosslinking density. These crosslinks induce a stiffening effect on the collagen bundles stretching. In fig. 46, the values of the linear modulus have been reported as a function of the shrinkage temperature rather than the DSC onset temperature, since the latter is affected by the denaturation of no-load bearing collagen molecules.

In order to evaluate the activation energy involved in the relaxation process, a Stepwise HIT has been done. According to Le Lous *et al.* [33], stress relaxation in a denatured polymeric network could be described by equation 1

$$\frac{\sigma(t)}{\sigma(t_0)} = \frac{N_t}{N_0} = e^{-kt} \qquad \text{-1-}$$

provided that isothermal condition has been achieved. In particular $\sigma(t)$ is the stress at time t while $\sigma(t_0)$ denotes the stress value when the isotherm is achieved N_t is the total number of load bearing polymeric chains remaining per unit volume at time t and N_0 is the initial number of load bearing polymeric chains. k is the rate constant which is age dependent. It is here assumed that the rate constant k should vary according to an Arrhenius equation:

$$k = A e^{-\frac{E_a}{RT}} \qquad \text{-2-}$$

where A is a pre-exponential constant, R the gas constant and the temperature T is expressed in Kelvin. The half time of stress decay defined by the following equation:

$$\frac{\sigma(t_{1/2})}{\sigma(t_0)} = \frac{1}{2} = e^{-kt_{1/2}} \qquad \text{-3-}$$

hence

$$\ln(t_{1/2}) = C + \frac{E_a}{RT} \qquad \text{-4-}$$

being $C = \ln(0.693/A)$. E_a is the slope of the regression line of the $\ln(t_{1/2})$ versus T^{-1} plot. Regression lines and E_a values are reported below.
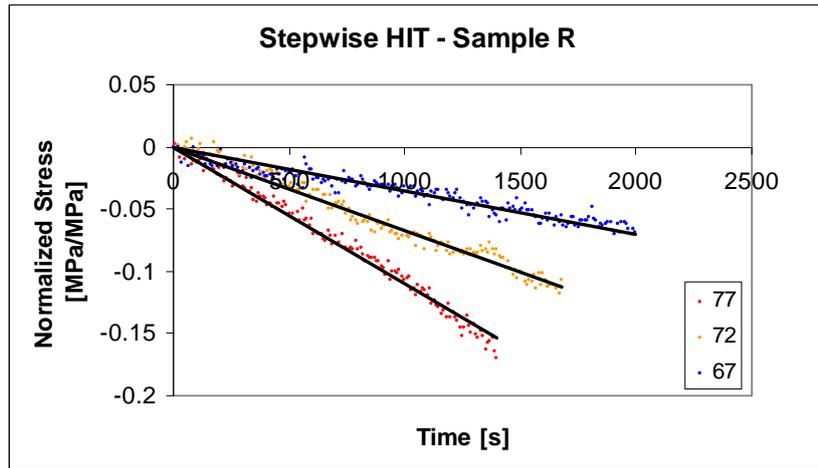
fig. 47 Sample R Stepwise HIT regression lines

	Activation Energy [kcal/mol]	
	AVG	ST. DEV
R step HIT	22.43	3.79

tab. 9 Sample R activation energy values

The E_a value here reported is consistent with the results of previous works [35] and is comparable to the activation energy involved in peptide bond hydrolysis. However the half time of stress decay and the activation energy evaluated for the $NaBH_4$ treated tissues are much higher as shown in fig. 48 and in tab. 10.
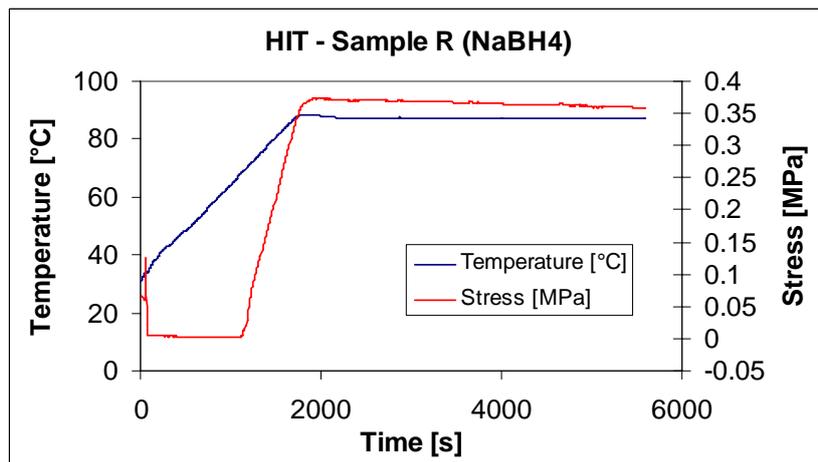
fig. 48 Sample R ($NaBH_4$ treated) HIT profile

	k		half time	
	AVG.	ST. DEV.	AVG.	ST. DEV.
R ($NaBH_4$)	0.000010	0.000001	70000	7000

tab. 10 Sample R ($NaBH_4$ treated) HIT results

This suggests that the primary structure of the denatured collagen network, i.e. the α-chains, it is unlikely to undergo peptide bond hydrolysis. Tissue thermal stability has to be ascribed to the presence of stable crosslinks.

5. Conclusions

This chapter addresses problems in the biomechanics of several collagen rich, load bearing tissues, which are of particular interest in fields of biological and clinical research. Dermis has been chosen as preferential tissue to study since its loose three dimensional and complex structure would serve as a more general model for connective tissue rather than tendon, with highly polarized fibres, and osmosis-supported cartilage. An experimental campaign has been designed in order to get insight into dermal composition, spatial arrangement of the micro-constituents and macroscopic mechanical properties. This design could be interpreted as a step towards a challenging "long-range" project of relating the tissue composition and structure to macroscopic properties.

Morphological analyses revealed that dermal cross section displays heterogeneities in terms of composition and spatial assembly of the macromolecules. Full split skin cannot be modelled as a homogeneous layer, "through-the-thickness" structural and compositional gradients must be taken into account.

Selective enzymatic digestion of matrix components is a well recognized technique for assessing relative influence of certain proteins on the macroscopic behaviour of the tissue. The effects of selected macromolecular components of the interfibrillar matrix on the elastic and viscous behaviour of the dermis have here been evaluated. Collagen fibre bundles mainly regulate tissue mechanical response at large strain. Elastin and iterfibrillar proteins induce mechanical constrains to relative motion of collagen molecules. In particular proteoglycans and interfibrillar proteins confer the tissue with stiffness at low frequency and small deformation, while elastin profoundly affect skin elastic recoil. However these macromolecules exert their mechanical action synergically.

The comparison between thermal and mechanical tests performed on both foetal an adult tissues constitutes a reliable developmental model for the study of tissue maturation and ageing.

6. References

1. Thacker J.G., Stalnecker M.C., Allaire P.E., Edgerton M.T., Rodeheaver G.T., Edlich R.F.: "Practical applications of skin biomechanics". *Clinics in Plastic Surgery* **4**, 167 - 171, 1977.

2. Harris R.I., Wallace A.L., Harper G.D., Goldberg J.A., Sonnabend D.H., Walsh W.R.: "Structural properties of the intact and the reconstructed coracoclavicular ligament complex". *The American Journal of Sports Medicin*e **28**, 103 - 108, 2000.

3. Woo S.L., Abramowitch S.D., Kilger R., Liang R.: "Biomechanics of knee ligaments: injury, healing, and repair". *Journal of Biomechanics* **39**, 1-20, 2006.

4. van Andel C.J., Pistecky P.V., Borst C.: "Mechanical properties of porcine and human arteries: implications for coronary anastomotic connectors". *The Annals of Thoracic Surgery* **76**, 58 - 64, 2003.

5. Khan S.N., Cammisa F.P. Jr, Sandhu H.S., Diwan A.D., Girardi F.P., Lane J.M.: "The biology of bone grafting". *The Journal of the American Academy of Orthopaedic Surgeons* **13**, 77 - 86, 2005.

6. Alastrue V., Calvo B., Pena E., Doblare M.: "Biomechanical modeling of refractive corneal surgery". *Journal Biomechanical Engineering* **128**, 150 - 160, 2006.

7. Hierner R., Degreef H., Vranckx J.J., Garmyn M., Massage P., van Brussel M.: "Skin grafting and wound healing-the *"dermato-plastic team approach"*". *Clinics in Dermatology* **23**, 343 - 352, 2005.

8. Silver F.H., Freeman J.W., DeVore D.: "Viscoelastic properties of human skin and processed dermis". *Skin Research and Technology* **7**, 18 - 23, 2001.

9. Yamauchi M., Woodley D.T., Mechanic G.L.: "Aging and cross-linking of skin collagen". *Biochemical and biophysical research communications* **152**, 898 - 903, 1988.

10. Debelle L., Tamburro A.M.: "Elastin: molecular description and function". *The international journal of biochemistry & cell biology* **31**, 261 - 272, 1999.

11. Le Lous M., Flandin F., Herbage D., Allain J.-C. : Influence of collagen denaturation on the chemorheological properties of skin, assessed by differential scanning calorimetry and hydrothermal isometric tension measurement. *Biochimica et Biophysica Acta* **717**, 295 – 300, 1982.

12. Lee T.C., Midura R.J., Hascall V.C., Vesely I.: "The effect of elastin damage on the mechanics of the aortic valve". *Journal of Biomechanics* **34**, 203 - 210, 2001.

13. Meyer, W.: "Histologic analogies of bovine hide, pig skin and the human integument". In Abstractband, 3. Freiberger Kollagensymposium, September 2004.

14. Jamall I.S., Finelli V.N., Que Hee S.S.: A simple method to determine nanogram levels of 4-hydroxyproline in biological tissues. *Analytical Biochemistry* **112**, 70-75, 1981

15. Billiar K.L., Sacks M.S.: A method to quantify the fiber kinematics of planar tissues under biaxial stretch. *Journal of Biomechanics* **30**, 753-756, 1997.

16. Hepworth D.G, Steven-Fountain A., Bruce D.M., Vincent J.F.V.: Affine versus non-affine deformation in soft biological tissues, measured by the reorientation and stretching of collagen fibres through the thickness of compressed porcine skin. *Journal of Biomechanics* **34**, 341-346, 2001.

17. Boote C., Sturrock E.J., Attenburrow G.E., Meek K.M.: Pseudo-affine behaviour of collagen fibres during the uniaxial deformation of leather. *Journal of Materials Science* **37**, 3651-3656, 2002.

18. Wright D.M., Attenburrow G.E.: The set and mechanical behaviour of partially processed leather dried under strain. *Journal of Materials Science* **35**, 1353 – 1357, 2000.

19. Covington A.D., Song L.: Crosslinking – What crosslinking. *Leather International* October 2003.

20. Osaki S.: Distribution Map of Collagen Fiber Orientation in a Whole Calf Skin. *The Anatomical Record* **254**, 147 – 152, 1999.

21. Fung Y.C.: Biomechanics: Mechanical properties of living tissues. *Ed. Springer* Chapter **7**, 242-320, 1993.

22. Oxlund H., Andreassen T.T.: "The roles of hyaluronic acid, collagen and elastin in the mechanical properties of connective tissues". *Journal of Anatomy* **131**, 611 - 620, 1980.

23. Viidik A., Danielson C.C., Oxlund H.: "On fundamental and phenomenological models, structure and mechanical properties of collagen, elastin and glycosaminoglycan complexes". *Biorheology* **19**, 437-451, 1982.

24. Oxlund H., Manschot J., Viidik A.: "The role of elastin in the mechanical properties of skin". *Journal of Biomechanics* **21**, 213 - 218, 1988.

25. Puxkandl R., Zizak I., Paris O., Keckes J., Tesch W., Bernstorff S., Purslow P., Fratzl P.: "Viscoelastic properties of collagen: synchrotron radiation investigations and structural model". *Philosophical transactions of the Royal Society of London* **357**, 191 - 197, 2002.

26. Kronick P.L., Sacks M.S.: "Matrix macromolecules that affect the viscoelasticity of calfskin". *Journal of Biomechanical Engineering* **116**, 140-145, 1994.

27. Keene D.R., Marinkovich M.P., Sakai L.Y.: "Immunodissection of the connective tissue matrix in human skin". *Microscoscopy Research and Technique* **38**, 394 - 406, 1997.

28. Keene D.R., Engvall E., Glanville R.W.: "Ultrastructure of type VI collagen in human skin and cartilage suggests an anchoring function for this filamentous network". *The Journal of Cell Biology* **107**, 1995-2006, 1988.

29. Cleary E.G., Gibson M.A.: "Elastin-associated microfibrils and microfibrillar proteins". *International review of connective tissue research* **10**, 97-209, 1983.

30. Miles C.A., Bailey A.J.: Thermal Denaturation of Collagen Revisited. *Proceedings of the Indian Academy of Sciences*: Chemical Sciences. **111**, 71-80, 1999.

31. Lamandé S.R., Sigalas E., Pan T.C., Chu M.L., Dziadek M., Timpl R., Bateman J.F.: "The role of the alpha3(VI) chain in collagen VI assembly. Expression of an alpha3(VI) chain lacking N-terminal modules N10-N7 restores collagen VI assembly, secretion, and matrix deposition in an alpha3(VI)-deficient cell line". *The Journal of biological chemistry* **273**, 7423 - 7430, 1998.

32. Miles C.A., Ghelashvili M.: Polimer-in-a-Box Mechanism for the Thermal Stabilization of Collagen Molecules in Fibres. *Biophysical Journal* **76**, 3243-3252, 1999.

33. Le Lous M., Allain J.-C., Cohen-Solal L., Maroteaux P. : The Rate Of Collagen Maturation in Rat and Human Skin. *Connective Tissue Research* **9**, 253-262, 1982.

34. Allain J.C., Le Lous M., Bazin S., Bailey A.J., Delaunay A. : Isometric Tension Developed During Heating of Collagenous Tissues. *Biochimica et Biophysica Acta*. **533**, 147-155, 1978.

35. Naimark, W. A., Waldman S. D., Anderson R. J., Suzuki B., Pereira C. A., Lee J. M.: Thermomechanical analysis of collagen crosslinking in the developing lamb pericardium. *Biorheology* **35**, 1-16, 1998.

Annex I - Preparation of leather from the salt foetal skin

Type of original material: Salted Friesian foetal skin

Process	Product	°C	%	Run	Remarks
Soak	Water	20	600	Run overnight	Sample collection
Flesh	Remove excess adipose tissue from the flesh side of the hide				
Lime	Water	20	200	1h	
	Na_2S		3		
	$Ca(OH)_2$		2	1h	
Wash	Water	20		10min and drain	
Delime	NH_4Cl	20	3.0	12h (in 20%water float)	pH= 8.5-9.0
Bate	Enzymes	37	0.1	1h and drain	
Wash	Water	20	200	10 min and drain	
Pickle	Water	20	100		
	NaCl		20		Diluted 1:5
	H_2SO_4		1	24h	Diluted 1:5 Sample collection
Chrome Tan	Chrome powder	30	8	Run overnight	
	MgO	45	0.4	4h	pH= 3.7
	Drain , Horse overnight				
Neutralise	Water	25	200	30 min and drain	
	Water	40	100	1h and drain	pH= 6.2
	$NaHCO_3$		1.5		Diluted 1:5
Fatliquor	Water	50	50		
	Sulphated oil		5	2h	Diluited 1:4
	Sulphited oil		5		
	HCOOH	50		2h	pH= 3.5
	Drain, toggle dry with no tension				
	Condition				
	Buff flesh side				

Chapter 3
Mathematical modelling of partially processed bovine dermis

1. Introduction

Soft biological connective tissues are composed of several microconstituents, each of them accomplishes specific biological and biomechanical functions. As for every solid with a microstructure there exists a correlation between the internal structure of connective tissues and their macroscopic mechanical behaviour. In the last few decades there has been a growing interest towards the study and the determination of soft tissue constitutive equations. These formulations provide a deeper insight into the biomechanics of soft tissues in both physiological and pathological conditions, they are of paramount importance in various clinical application such as tissue transplantations, plastic surgery and wound healing. Moreover, constitutive relations are necessary for the solution of problems in continuum mechanics since without them the set of equations which describes the problem is not closed.

Many different constitutive equations have been proposed for various tissues. Basically there exist two different approaches to formulate constitutive equations. One is practically devoid of structural considerations and aims at fitting experimental data reasonably well. This phenomenological approach has been widely used but presents several drawbacks which will be discussed below. Alternatively constitutive relations for biological tissues can be formulated by taking into account their microstructure directly.

The phenomenological approach allows to predict gross mechanical experiments without requiring detailed structural information. However phenomenological models, like *all* constitutive models, must obey to *a priori* restrictions. They have to be frame indifferent, tensorially correct, account for material symmetries and kinematic constraints. The main problem related to phenomenological models is that they describe the behaviour of a material under condition of interest, not the material itself.

The microstructural approach is more attractive in principle since it aims at determining the constitutive relation in terms of physically meaningful material parameters that represent the actual composition of the material. A proper structural approach must account for the internal load carrying mechanism of the individual constituents of the tissue, and this then increases its predictive capability compared with a phenomenological

approach. The microstructural relations are, however, mathematically complex and require precise quantification of the tissue inner structure. Insight into the structural organization of the complex three dimensional network have been obtained by application of polarized light microscopy [1], high angle x-ray scattering [2], microwave absorption [3] end electron microscopy [4]. Thus far, however, these microstructural relations do not capture gross mechanical behaviour of soft tissues better than phenomenological ones.

The goal of this chapter is to formulate a constitutive model able to describe the macroscopic mechanical behaviour of (partially processed) bovine reticular dermis. Due to complexity of both the behaviour of the tissue and its microstructure, here a compromise is proposed between structural accuracy and mathematical simplicity, thus avoiding the necessity of detailed modelling of the complex spatial assembly of dermal microconstituents.

A common way to understand the constitutive relationship between stress and strain of a material subjected to uniaxial tension is the comparison of the stress-strain curves provided by the theoretical model and the ones obtained from experiments. An efficient model should predict the mechanical response of independent deformation states, while involving the same set of material parameters. In other words, a model can predict the stress-strain response of a certain material in uniaxial tension, with a very good agreement with the experimental data, but the same model, with the same material constants, could fail to do so when applied to an other independent mechanical test, such as confined compression.

Here we consider the description of the macroscopic mechanical behaviour by means of continuum mechanics hypotheses, finite hyperelasticity and the theory of mixtures which has been applied successfully in the modelling of fibre reinforced composite materials.

2. Experimental details

Two adult bovine skins have been partially processed at the British School of Leather Technology (BSLT - University of Northampton, UK). In particular the skins have been subjected to a conventional tanning process up to the wet blue step (i.e. not dyeing, fatliquoring, retanning or finishing). A portion of the butt area, defined by the official sampling ISO2419 standard, has been cut from both skins and subsequently split approximately at the papillary-reticular junction with a revolving band knife splitting machine (Rizzo, Italy). The terms **grain** and **corium** will be used as synonyms of papillary layer and reticular dermis respectively in the remainder. The two split layers have been overlapped and punched with a dumbbell shaped socket puncher, in order to obtain matching pairs of grain and corium specimens.

Six corium-grain matching pair samples have been taken from one skin. In particular, three pairs have been cut alongside backbone direction, the remaining three pairs have been cut across the backbone direction. These samples have been used in simple tension experiments.

Three corium-grain matching pair samples have been taken from the second skin, cut in the direction parallel to the backbone. These samples have been used in the videoextensimetry analysis.

Tension testing

Specimens data are summarised in tab. 1.

Layer	Direction (respect to the backbone)	Number of samples	Thickness [mm]
Papillary	Parallel	3	0.82 ± 0.02
Reticular	Parallel	3	1.71 ± 0.07
Papillary	Perpendicular	3	0.86 ± 0.03
Reticular	Perpendicular	3	1.77 ± 0.10

tab. 1 Data of the specimens used in the simple tension test

The specimens have been tested at the Department of Material and Production Engineering (DIMP - University of Naples Federico II, Italy). The uniaxial testing has been carried out using an Instron dynamometer equipped with a 100N load cell (accuracy class 0.5). The crosshead speed has been set at 10 mm/min. The upper load limit threshold did

not cause the specimens to break. Statistical analysis has been performed using Excel (Microsoft)

Video extensometry

Specimens data are summarised in tab. 2.

Layer	Direction (respect to the backbone)	Number of samples	Thickness [mm]
Papillary	Parallel	3	0.79 ± 0.03
Reticular	Parallel	3	1.53 ± 0.04

tab. 2 Data of the specimen used in the videoextensometry testing

Tension tests have been carried out as described above. Optical strain measurement has been performed with two digital cameras (JAI Corporation model CV-A50) equipped with AF zoom-Nikkor lenses (Nikon). The camera set up has been arranged in order to collect videos of both the width and the thickness of the tested specimens as depicted in figure 1.
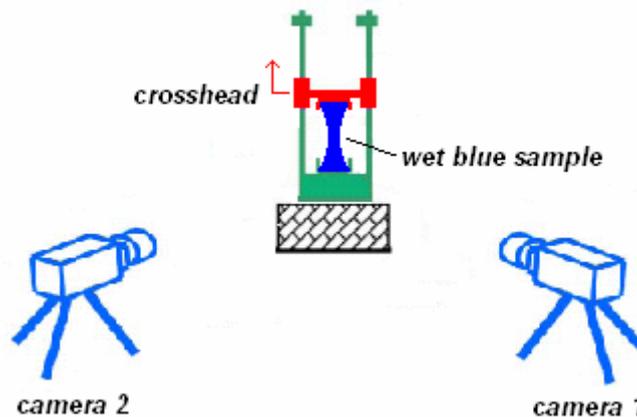

fig. 1 Video extensometry set up

Camera 1 has been committed to monitor longitudinal stretch and transverse stretch, while camera 2 has been used to asses thickness variations.

Eleven circular visual markers, of approximately 1.5 mm diameter, have been carefully drawn on the front face of the sample with water-proof ink. The thickness has been marked with a 5 mm height rectangle placed approximately on the middle of the specimen. The position and the designation of the markers is reported in the schematic below.
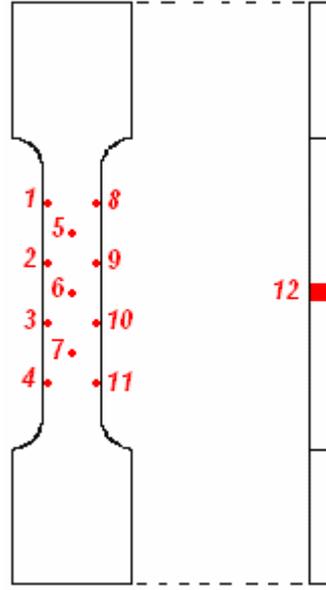
fig. 2 Visual markers designation

Each camera recorded 16 bit digital video, 500 x 160 image size. Video capturing has been performed at a 25 frames per second rate using the ImaQ tool of the Labview software (National Instruments, USA). A custom designed program acquires both the images and the load cell signal. This ensures a perfect frame-load value matching. Camera 1 magnification has been set in order to track deformations up to 40%. With this particular set up, the pixel size is 0.1 x 0.1 mm^2, while camera 2 magnification has been set in order to have a pixel size of approximately 0.05 x 0.05 mm^2. The image processing and marker tracking have been performed with WCIF Image J software (National Institutes of Health, USA). Basically the software tracks pixel movement of visual-marker centres. The following quantities have been used in order to assess the average values of axial deformation:

$$\varepsilon_{ij} = \frac{l_{ij}(t) - l_{ij}^0}{l_{ij}^0}$$

where ε_{ij} is the deformation of the portion of the sample delimited by the markers i and j. l_{ij}^0 is the length of the segment ij in the reference undeformed configuration and $l_{ij}(t)$ is the current length, where the ij pairs can be 1-2, 2-3, 3-4, 5-6, 6-7, 8-9, 9-10, 10-11.

Transverse deformation is defined by

$$\varepsilon_{ij}^t = \frac{l_{ij}^t(t) - l_{ij}^{t0}}{l_{ij}^{t0}}$$

where ε_{ij}^t is the deformation of the portion of the sample delimited by the markers i and j. l_{ij}^{t0} is the length of the segment ij in the reference undeformed configuration and $l_{ij}^t(t)$ is the current length. In this case, the ij pairs are 1-8, 2-9, 3-10, 4-11.

Axial and transverse stretch are defined respectively by

$\lambda_{ij} = \varepsilon_{ij} + 1$ with ij = 1-2; 2-3; 3-4; 5-6; 6-7; 8-9; 9-10; 10-11

$\lambda_{ij}^t = \varepsilon_{ij}^t + 1$ with ij = 1-8, 2-9, 3-10, 4-11

3. Experimental results

The stress-strain plot for the tested split is shown in fig. 3.
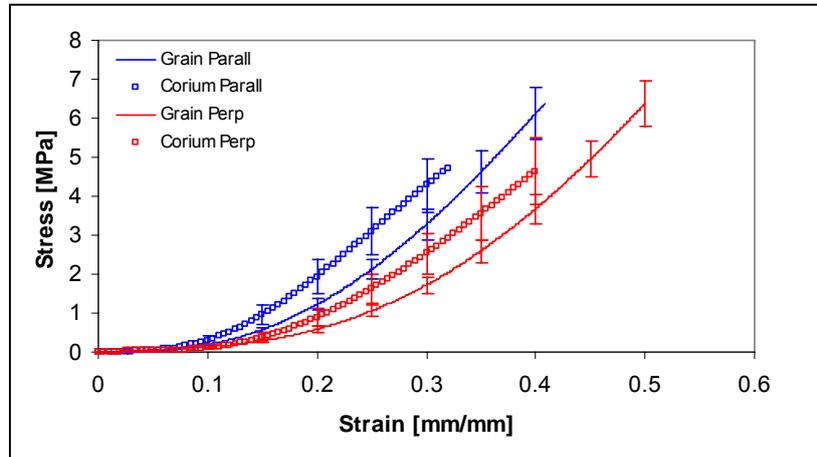
fig. 3 Stress-strain plots of grain and corium samples

The stress and strain diagrams display the characteristic *J shaped curve* of soft connective tissues. As stated in the previous chapter, it is possible to discern three different regions in a *J* shaped curve: the starting low-modulus region, a toe region with increasing modulus and a final linear region with higher and nearly constant modulus. It is here assumed that the toe region extent can be conveniently quantified by the intercept of the linear region on the strain axis. This latter value will be referred to, in the remainder, as "toe intercept".

The slope value of the linear region, the strain interval in which the slope has been evaluated and the toe-intercept value are reported in tab. 3.

Sample designation	Modulus [MPa]	Strain interval	Toe Intercept
Grain (parallel)	30.93 ± 2.59	0.35 – 0.40	0.202 ± 0.006
Corium (parallel)	23.38 ± 1.82	0.25 – 0.30	0.118 ± 0.020
Grain (perpendicular)	28.42 ± 2.38	0.45 – 0.50	0.276 ± 0.003
Corim (perpendicular)	21.63 ± 3.30	0.35 - 0.40	0.187 ± 0.012

tab. 3 Mechanical properties of grain and corium samples

Grain samples have a significantly higher linear modulus ($p<0.05$) than corium samples, irrespective of the direction of the applied load. Within the same layer, whether papillary or reticular, the value of the linear modulus is not affected by the direction of the applied load ($p>0.05$). Grain and corium samples, parallel to the backbone have a significantly less extended toe region ($p<0.05$) than their respective counterparts in the orthogonal direction.

Videoextensometry – Reticular dermis

A typical marker tracking experiment provided by Image J, produces a time (i.e. frame) – axial displacement plot like the one depicted in fig. 4.
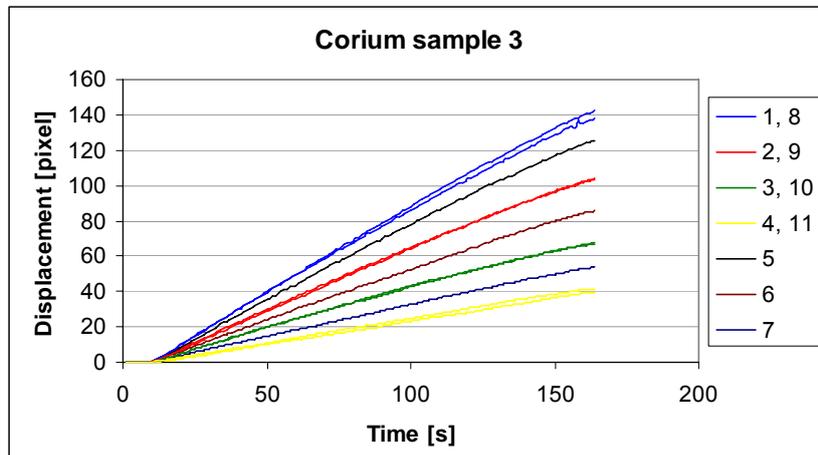

fig. 4 Marker tracking

Usually a limited mismatch of the axial displacement of markers 1-8 and 4-11 is observed. Moreover, these markers are closer to the specimen clamps and probably are affected by their constraining effect. Thus only the ε_{2-3}, ε_{5-6}, ε_{6-7} and ε_{9-10} stretches have been chosen in order to evaluate the average axial stretching, while the transverse stretch is the average of ε_{2-9}^{t} and ε_{3-10}^{t}.

All the displacement-time curves intercept the time axis at the same value (fig. 5).
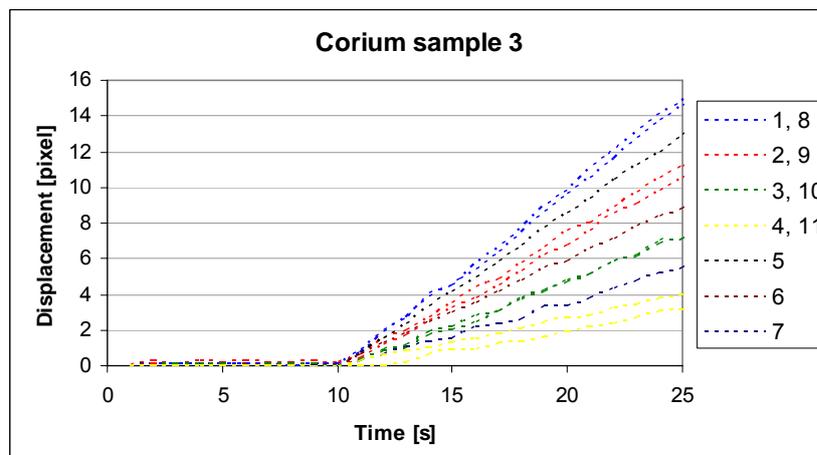
fig. 5 Marker tracking. Magnification of fig. 4

This value of time has been chosen as reference time in which the reference length l_{ij}^0 is evaluated.
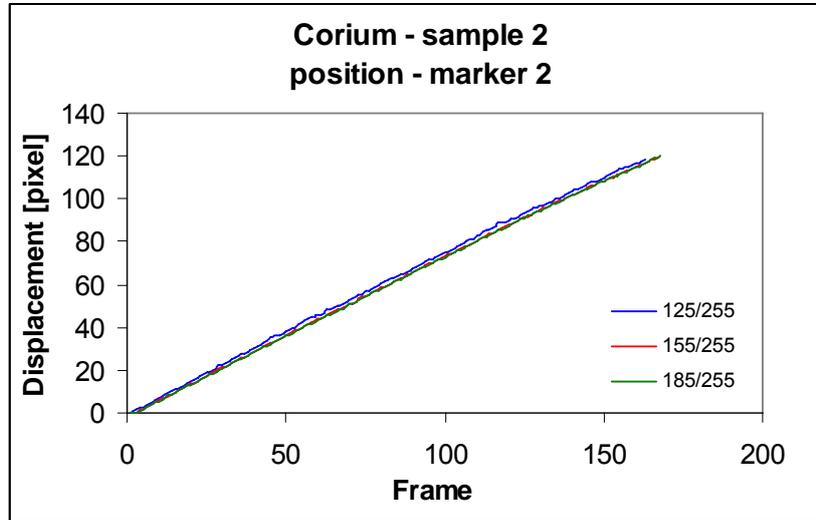
fig. 6 Effect of marker size on marker traking process

The image analysis software can perform marker tracking of binary (black and white) images. Basically binary conversion of a greyscale image consists in setting a grey threshold level: all the pixels whose grey intensity (a value in the [0, 255] interval) is above the threshold are turned to black, while all the other pixels, having a lower grey intensity, are blanked. This conversion could induce an additional error since the thresholding process alters the pixel size of the markers. In order to asses the influence of marker size on the position tracking, video images have been processed at different contrast level (contrast thresholding). More in detail, the displacement of marker 2 (see fig. 2) for three different values of the contrast threshold (125/255, 155/255 and 185/255) is reported in fig. 6. The area of the marker was approximately 21, 33 and 49 pixels respectively. Particle tracking seems to be stable enough, in particular for higher value of the threshold level (the curves 155/255 and 185/255 are practically overlapped). The threshold value has been chosen in the range 150/255 - 185/255 for all the samples tested. Since particle tracking is almost irrespective of the marker size and shape, it has been assumed that the error, on the marker displacement, is of the order of one pixel.

Transverse versus longitudinal stretch diagrams are reported in fig. 7.
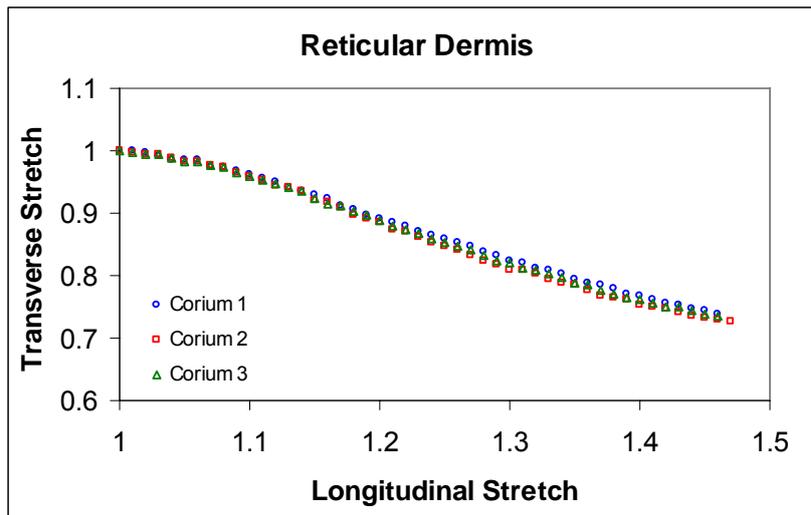
fig. 7 Reticular dermis. Transverse vs longitudinal stretch plot

Assuming then that the error of the software in the marker tracking process is of the order of one pixel, the maximum percentage error on the longitudinal stretch and transverse stretch has been found to be 5.23 and 6.55 respectively. The assessment of the contraction in the direction of the thickness has been performed in manual mode. Unfortunately the error associated with this operation is very high, owing to the small thickness of the specimens tested. Assuming that in the worst case the error associated with this manual operation is 2 pixels per edge (4 pixels error over a thickness of 30-35 pixels), it has been estimated an average contraction of 10-12% at axial deformation of 45%.

Videoextensometry – Papillary dermis

Eleven circular markers (approximately 1.5 mm diameter) have been drawn on the upper surface of each grain specimen. The pattern of the markers is the same as depicted in fig. 2. Longitudinal and transverse deformation are defined as previously stated.

The evaluation of the axial and transverse deformation of papillary dermis, however, did not follow the outline described for the case of reticular dermis. The deformation of a sample of papillary dermis subjected to uniaxial load is not homogeneous. An out-of-plane deformation is always present, which causes the cross section to curl (see fig. 8).
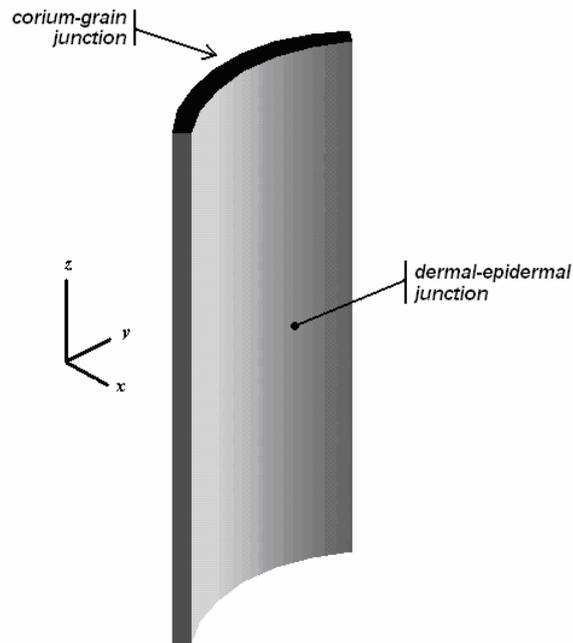
fig. 8 Schematic of the cross section curling of grain samples

In order to acquire data on the three-dimensional deformation, the images captured by Camera 1 (see fig. 1) have been used to determine the longitudinal stretch (in the same manner as described for the reticular dermis) and the distance **AC** (fig. 9). The images captured by Camera 2 have been used to evaluate the length of the projection of the **AB** segment on the xz plane (fig. 9). Owing to the presence of dynamometer clamps, only the middle third of the specimen shows an extensive cross section curling. As a consequence of that, image analyses and length computations have been performed in the central portion of the specimen.
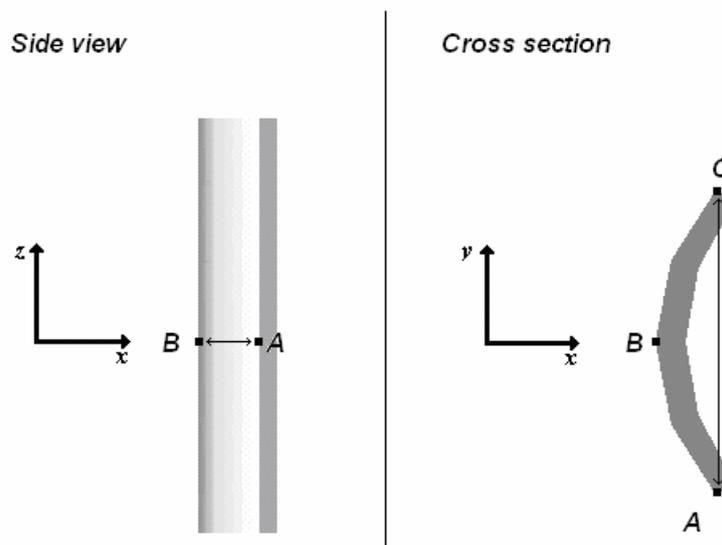

fig. 9 Assessment of transverse deformation

It is assumed that the arc **ABC** is conveniently interpolated by a parabolic arc. The transverse stretch is defined as the length of such parabolic arc divided by specimen width in the undeformed configuration. In particular, the image processing software has provided distance **AC** and **AB** in terms of pixels. Arc length has been evaluated by means of the well know equation

$$l_{ABC} = \int_A^B \sqrt{1 + \left(\frac{dg}{dy}\right)^2}\, dy$$

where $x = g(y)$ is the Cartesian equation of the parabolic arc.

Papillary layer transverse stretch versus longitudinal stretch diagram is reported in fig. 10
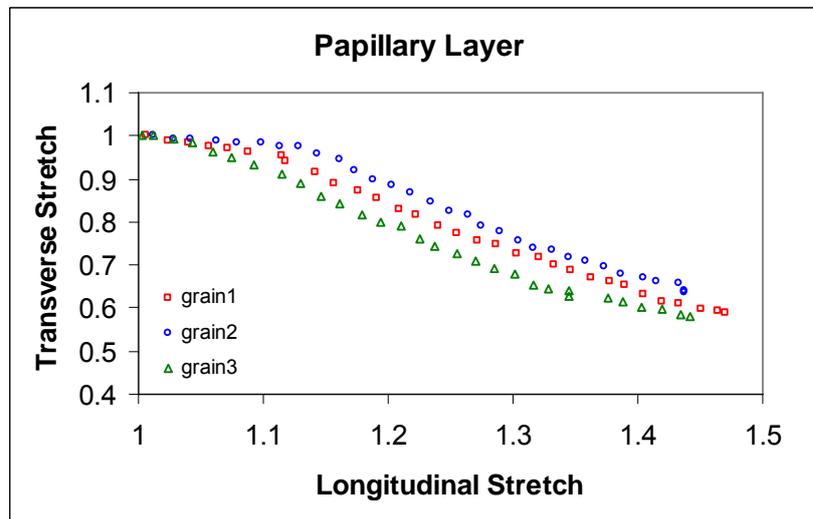
fig. 10 Papillary dermis. Transverse vs longitudinal stretch plot

Several source of errors could affect the evaluation of both transverse and longitudinal stretch. Spatial evolution of the **AB** segment, has been evaluated in manual mode. The assumption of a (constant) "worst-case" error of two pixels per edge, clearly leads to a broad uncertainty in the overall arc length determination, especially in the early steps of deformation, i.e. the percentage incidence of the error is higher in the case of small segments. Moreover, owing to extensive cross section curling, the brightness on the sample surface is not constant. In particular, shades appear on sample edges at large deformations, causing the markers to become less visible. This problem could be partially solved by increasing the power of the light source, since a very intense white light can blank the markers out. The arc **ABC**, previously defined, could not be conveniently interpolated by a parabolic arc. The transverse versus longitudinal stretch curves plotted in fig. 10 has to be interpreted as qualitative trend and it should be borne in mind that a large

error is associated with the curves. A quantitative evaluation of the uncertainty is, however, virtually impossible to achieve.

4. Mathematical model

4.1 Continuum Mechanical Framework

Fibre reinforced composites, or composites, are a class of materials composed of a matrix material and one or more families of fibres. They are heterogeneous and have strong directional properties and their mechanical responses are regarded as anisotropic. Several biological tissues like tendons [5], ligaments [6], arteries [7], heart valves [8] have been modelled as composite materials. In particular the collagen fibres represent the load bearing reinforcement and are embedded in an isotropic viscous matrix constituted by water, soluble proteins, proteoglycans, interfibrillar proteins and elastin. As pointed out in the previous chapter, dermis possesses the same microconstituents and can indeed be considered and modelled as a composite.

The basics equations of finite deformation kinematics and hyperelasticity are introduced in this section. The reader is referred to the excellent texts of Holzapfel [9] and Bonet and Wood [10] for an exhaustive treatment about nonlinear continuum mechanics.

Let Ω_0 be a fixed reference configuration of the continuum body of interest. The one-to-one mapping $\chi : \Omega_0 \rightarrow R^3$ transforms a typical material point $\boldsymbol{X} \in \Omega_0$ in the reference configuration to a position $\boldsymbol{x} = \chi(\boldsymbol{X}) \in \Omega$ in the deformed configuration. Further, let

$$\boldsymbol{F}(\boldsymbol{X}) = \frac{\partial \chi(\boldsymbol{X})}{\partial \boldsymbol{X}} \qquad \text{-1-}$$

be the deformation gradient and

$$J(\boldsymbol{X}) = \det \boldsymbol{F}(\boldsymbol{X}) > 0 \qquad \text{-2-}$$

the local volume ratio. In order to compute the body deformation, the right Cauchy-Green tensor $\boldsymbol{C}$ and the left Cauchy-Green tensor $\boldsymbol{b}$ are important stretch measure in material and spatial coordinates, respectively. $\boldsymbol{C}$ and $\boldsymbol{b}$ are defined as follows:

$$\boldsymbol{C} = \boldsymbol{F}^T \boldsymbol{F}$$
$$\boldsymbol{b} = \boldsymbol{F}\boldsymbol{F}^T \qquad \text{-3-}$$

Rather than dealing directly with the deformation gradient $\boldsymbol{F}$, it is here reported the multiplicative decomposition of $\boldsymbol{F}$ into a *volume changing* (*spherical* or *dilatational*) and *volume preserving* (*unimodular* or *distortional*) parts [11]

$$\boldsymbol{F} = (J^{1/3}\boldsymbol{I})\overline{\boldsymbol{F}} \qquad \text{-4-}$$

where $(J^{1/3}\boldsymbol{I})$ is the spherical part and $\overline{\boldsymbol{F}}$, so that $\det \overline{\boldsymbol{F}} = 1$ is the distortional part. As a consequence of that, the modified counter parts of $\boldsymbol{C}$ and $\boldsymbol{b}$ (associated with $\overline{\boldsymbol{F}}$) are

$$C = F^T F = J^{2/3} \overline{C} \quad \overline{C} = \overline{F}^T \overline{F}$$
$$b = F F^T = J^{2/3} \overline{b} \quad \overline{b} = \overline{F} \overline{F}^T$$

-5-

In order to describe the hyperelastic stress response of the isotropic matrix of the composite, we postulate the existence of a *Helmholtz free energy function* Ψ (also referred to as *strain energy function*) defined per unit reference volume, so that

$$S = 2 \frac{\partial \Psi(C)}{\partial C}$$

-6-

being S the second Piola-Kirchhoff stress tensor. A decoupled form of the strain energy function is here adopted:

$$\Psi(C) = \Psi_{vol}(J) + \Psi(\overline{C})$$

-7-

where the function $\Psi_{vol}(J)$ is a purely volumetric contribution and $\Psi(\overline{C})$ is purely isochoric. A fundamental requirement for strain energy functions is that they must be objective during rigid body motions, i.e. independent of the observer. If a scalar valued tensor function is an invariant under a rotation it may be expressed in terms of the principal invariants of its arguments, in this case C or b [see 9 and references therein], thus

$$\Psi = \Psi(I_1(C), I_2(C), I_3(C)) = \Psi_{vol}(J) + \Psi_{iso}(I_1(\overline{C}), I_2(\overline{C}))$$

-8-

Assuming that the only source of anisotropy of the solid arises from the presence of fibres and that the matrix and the fibres undergo the same (i.e. affine) deformation, then the stress at a material point depends not only on the deformation gradient F but also on the fibres direction. The direction of a fibre, or of a family of parallel fibres, is defined by the unit vector $\mathbf{a_0}$. The deformation gradient maps the fibre element $\mathbf{a_0}$ in the reference configuration, in an element which in the current configuration has direction $\mathbf{a}$ and length $\lambda |\mathbf{a}|$, according to

$$\lambda \mathbf{a}(\mathbf{x}, t) = F(\mathbf{X}, t) \mathbf{a_0}(\mathbf{X}) \quad \Rightarrow \quad \lambda^2 = \mathbf{a_0} \cdot F^T F \mathbf{a_0} = \mathbf{a_0} \cdot C \mathbf{a_0}$$

-9-

Because of the directional dependence on the fibre deformation, the strain energy function depends explicitly on both the right Cauchy-Green tensor and structural tensors which take into account fibres direction in the material configuration.

Assuming that dermis could be conveniently modelled as a composite reinforced with two family of fibres, it is required that the strain energy function has the form of

$$\Psi = \Psi_{vol}(J) + \Psi_{iso}(\overline{C}, A_0, G_0)$$

-10-

where A_0 and G_0 are two symmetric second-order tensors which characterize the structure of the tissue, and are function of the direction of the two families of fibres $\mathbf{a_0}$ and $\mathbf{g_0}$. Since the sense of both $\mathbf{a_0}$ and $\mathbf{g_0}$ is immaterial, Ψ is taken as an even function of $\mathbf{a_0}$ and $\mathbf{g_0}$

$$\boldsymbol{A_0} = \mathbf{a_0} \otimes \mathbf{a_0}$$
$$\boldsymbol{G_0} = \mathbf{g_0} \otimes \mathbf{g_0}$$

-11-

where the symbol $\otimes$ indicates the dyadic product. Such strain energy function must be unchanged if the fibre reinforced composite in the reference configuration undergoes a rigid rotation. This requirement is satisfied if Ψ is a function of the set of invariants [12]

$$I_1(\boldsymbol{C}) \quad I_2(\boldsymbol{C}) \quad I_3(\boldsymbol{C})$$
$$I_4(\boldsymbol{C,A_0}) = \mathbf{a_0} \cdot \boldsymbol{C}\mathbf{a_0} = \lambda_{\mathbf{a_0}}^2 \quad I_5(\boldsymbol{C,A_0}) = \mathbf{a_0} \cdot \boldsymbol{C^2}\mathbf{a_0}$$
$$I_6(\boldsymbol{C,G_0}) = \mathbf{g_0} \cdot \boldsymbol{C}\mathbf{g_0} = \lambda_{\mathbf{g_0}}^2 \quad I_7(\boldsymbol{C,G_0}) = \mathbf{g_0} \cdot \boldsymbol{C^2}\mathbf{g_0}$$
$$I_8(\boldsymbol{C,A_0,G_0}) = (\mathbf{a_0} \cdot \mathbf{g_0})\mathbf{a_0} \cdot \boldsymbol{C}\mathbf{g_0} \quad I_9(\boldsymbol{A_0,G_0}) = (\mathbf{a_0} \cdot \mathbf{g_0})^2$$

-12-

The invariants $I_4, \ldots, I_9$ are associated with the anisotropy generated by the two families of fibres. In particular I_4 and I_5 characterize the family of fibres in direction $\mathbf{a_0}$, and I_6 $,I_7$ refer to the family of fibres in direction $\mathbf{g_0}$. Both of them have a precise physical meaning since they are the square of the stretch λ in the fibre direction. The invariants I_5, I_7, I_8 and I_9 will be neglected and not considered in the following modelling.

4.2 Anisotropic hyperelastic model

The anisotropic and hyperelastic model reported here is based on the structural constitutive model developed by Driessen and coworkers [13] for cardiovascular tissues.

Here, bovine reticular dermis is modelled as a compressible fibre reinforced composite. The isotropic matrix is modelled as a specific case of the Blatz-Ko material class, whose Cauchy stress tensor σ_m is

$$\sigma_m = \frac{\mu}{J} \left[-I_3^{-\beta} \mathbf{I} + \boldsymbol{b} \right]$$

-13-

where μ and β are material constants, $\mathbf{b}$ is the second order left Cauchy-Green deformation tensor, $\mathbf{I}$ is the identity tensor and $I_3 = J^2$ is the third scalar invariant of $\mathbf{b}$.

according to Ionescu et al. [14] the elastic response of collagen fibres has been considered exponential in the toe region and linear subsequently. The fibre (Cauchy) stress σ_f is given by

$$\sigma_f = \begin{cases} 0 & \lambda_f < 1 \\ k_1(e^{k2(\lambda_f^2 - 1)} - 1) & 1 < \lambda_f < \lambda_{lock} \\ k_3 \lambda_f + k_4 & \lambda_f > \lambda_{lock} \end{cases}$$

-14-

where λ_f is the fibre stretch and k_1, k_2, k_3, k_4, and λ_{lock} are material constants. However, just three constants are independent since k_2 and k_4, are determined by the condition that collagen stress and its first derivative must be continuous at λ_{lock}, which means

$$k_2 \mid \quad 2k_1 k_2 \lambda_{lock} e^{k2(\lambda_f^2-1)} - k_3 = 0$$

$$k_4 = k_1(e^{k2(\lambda_f^2-1)} - 1) - k_3 \lambda_{lock}$$

-15-

The fibres strain energy function has been designed in order to simulate fibres uncrimping and disentanglement. Fibres do not withstand compressive loads, thus their contribution to the total stress is null if $\lambda_f < 1$. Up to a certain stretch value, defined by λ_{lock}, the elastic response is exponential. This feature has been observed experimentally and is physically reasonable: the higher is the total macroscopic stretch, the more fibres are uncrimped and stretched.

The continuum assumption is reasonable since physiologic fibre diameters are several orders of magnitude smaller that the macroscopic dimensions of interests. Applying the rule of mixtures, the total stress exerted by the composite can be written as

$$\boldsymbol{\sigma} = \boldsymbol{\sigma}_m + \varphi_f(\boldsymbol{\sigma}_f - \mathbf{e}_f \cdot \boldsymbol{\sigma}_m \mathbf{e}_f)\mathbf{e}_f \otimes \mathbf{e}_f$$

-16-

being φ_f the fibre volume fraction and $\mathbf{e}_f$ is the fibre direction in the deformed configuration.

Partially processed reticular dermis is not a true composite, since it is practically devoid of ground substance and it is mainly constituted by collagen fibres, elastin and water. Apparently the hypothesis of the theory of mixtures should be inappropriate for this specific case. However, we assume that partially processed reticular dermis can be idealized as composed of non-interacting families of planar distributed fibres and a homogeneous matrix. The matrix does not need to be an embedding material *per se*, it should rather be considered as a collection of structural constituents, with an isotropic gross mechanical behaviour, which take into account all the transverse interactions between adjacent planes of collagen fibres.

Equation 16 stated that in the fibre direction, fibre stress σ_f and matrix stress σ_m both contribute to the total stress, weighted with fractions φ_f and $(1 - \varphi_f)$ respectively:

$$\mathbf{e}_f \cdot \boldsymbol{\sigma}\mathbf{e}_f = \mathbf{e}_f \cdot [\boldsymbol{\sigma}_m + \varphi_f(\boldsymbol{\sigma}_f - \mathbf{e}_f \cdot \boldsymbol{\sigma}_m \mathbf{e}_f)\mathbf{e}_f \otimes \mathbf{e}_f]\mathbf{e}_f =$$

$$= \mathbf{e}_f \cdot \boldsymbol{\sigma}_m \mathbf{e}_f + \varphi_f(\boldsymbol{\sigma}_f - \mathbf{e}_f \cdot \boldsymbol{\sigma}_m \mathbf{e}_f) = (1 - \varphi_f)\mathbf{e}_f \cdot \boldsymbol{\sigma}_m \mathbf{e}_f + \varphi_f \boldsymbol{\sigma}_f$$

-17-

On the other hand, following Driessen *et al.* [13], it is assumed that fibres do not affect the transversal properties of the composite. It is then required that the stress in any direction **a** orthogonal to $\mathbf{e}_f$ is equal to the matrix stress:

$$\boldsymbol{a} \cdot \sigma \boldsymbol{a} = \boldsymbol{a} \cdot [\sigma_m + \varphi_f(\sigma_f - \boldsymbol{e}_f \cdot \sigma_m \boldsymbol{e}_f)\boldsymbol{e}_f \otimes \boldsymbol{e}_f]\boldsymbol{a} = \boldsymbol{a} \cdot \sigma_m \boldsymbol{a} \qquad \text{-18-}$$

Equations 10 and 16 can be extended to account for N fibre directions. Assuming that there is no interaction between fibre layers,

$$\sigma = \sigma_m + \sum_{i=1}^{N} \varphi_f^i (\sigma_f^i - \boldsymbol{e}_f^i \cdot \sigma_m \boldsymbol{e}_f^i)\boldsymbol{e}_f^i \otimes \boldsymbol{e}_f^i \qquad \text{-19-}$$

Assuming that the fibre stress is irrespective of fibre direction then $\sigma_f^i = \sigma_f$. In order to design a fibre architecture which closely resembles that of the native tissue, we need to define fibre direction with respect to a local coordinate system. Considering the system defined in fig. 8, with the z axis along the direction of the applied load, then the fibre direction in the undeformed configuration is

$$\boldsymbol{e}_f^0 = \left\{ \begin{array}{c} 0 \\ \sin\vartheta \\ \cos\vartheta \end{array} \right\}$$
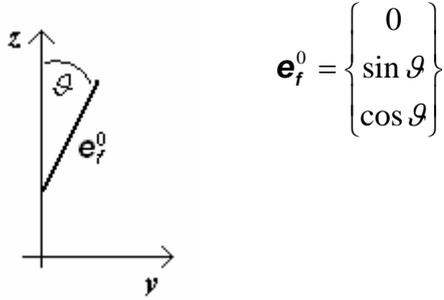
According to the experimental results provided by Boote and coworkers [2], we assume that fibre volume fraction follows a normal distribution:

$$\varphi_f^i(\vartheta) = A e^{-\frac{(\vartheta - \mu^i)^2}{2\sigma^{i^2}}} \qquad \text{-20-}$$

where μ^i and σ^i are the mean value and the standard deviation of the i-th family of fibres and the parameter A is defined such that the total fibre volume fraction φ_{tot} is given as:

$$A = \frac{\varphi_{tot}}{\displaystyle\int_{-\pi/2}^{\pi/2} \sum_{i=1}^{N} e^{-\frac{(\vartheta - \mu^i)^2}{2\sigma^{i^2}}} \, d\vartheta} \qquad \text{-21-}$$

In order to compare the model predictions with the experimental data provided by the video extensomety test, we follow a semi-inverse method. In particular we assume that the motion, in Cartesian coordinates is given by:

$$\left\{ \begin{array}{l} x = \lambda_1 X \\ y = \lambda_2 Y \\ z = \lambda Z \end{array} \right. \qquad \text{-22-}$$

where the uppercase letters represent the material coordinates, while the lowercase letters are the spatial coordinates. λ_i are the (constant) principal stretches. From the motion 22 the deformation gradient becomes

$$\boldsymbol{F} = \begin{bmatrix} \lambda_1 & 0 & 0 \\ 0 & \lambda_2 & 0 \\ 0 & 0 & \lambda \end{bmatrix}$$

-23-

The matrix components of the deformation gradient are constant, thus the deformation is homogeneous. As with all semi-inverse methods, the stress that is necessary to engender the motion 22 can be calculated once the constant entries in 23 are determined. In order to do so, we must superimpose that they satisfy the equilibrium equation and, of course, the boundary conditions. In the case of negligible body forces and static problems, the balance of linear momentum reduces to

$$\text{div}(\boldsymbol{\sigma}) = \boldsymbol{0}$$

-24-

Since the deformation is homogeneous, the equations 24 are trivially satisfied. Stress components are then determined by solving the following non-linear set of equations

$$\begin{cases} \sigma_{11} = 0 = \lambda_1^2 - I_3^{-\beta} \\ \\ \sigma_{22} = 0 = \dfrac{\mu}{J}(\lambda_2^2 - I_3^{-\beta}) + \varphi_f[\sigma_f - \dfrac{\mu}{J\lambda_f^2}(\lambda_2^4 \sin^2 \vartheta + \lambda^4 \cos^2 \vartheta - I_3^{-\beta})]\dfrac{\lambda_2^2}{\lambda_f^2}\sin^2 \vartheta \\ \\ \sigma_{33} = \dfrac{\mu}{J}(\lambda^2 - I_3^{-\beta}) + \varphi_f[\sigma_f - \dfrac{\mu}{J\lambda_f^2}(\lambda_2^4 \sin^2 \vartheta + \lambda^4 \cos^2 \vartheta - I_3^{-\beta})]\dfrac{\lambda^2}{\lambda_f^2}\cos^2 \vartheta \end{cases}$$

-25-

φ_f is provided by integrating 21 in the $\left[-\dfrac{\pi}{2}, \dfrac{\pi}{2}\right]$ range.

A parametric study has been performed in order to evaluate how the numerical model responds to changes to material and structural parameters. The "base case" around which a single parameter is varied (while holding the other parameters fixed) involves the following set of constant:

$$\begin{aligned} & \mu = 1 \quad \beta = 1 \quad \varphi = 0.75 \\ & k_1 = 0.1 \quad k_3 = 10 \quad \lambda_{lock} = 1.1 \\ & \vartheta = \frac{\pi}{6} \quad \sigma_{\vartheta} = \frac{\pi}{12} \end{aligned}$$

-26-

The stress strain response predicted by the model with this particular set of parameters displays the characteristic *J* shaped curve of soft collagenous tissues.

The increase of matrix shear modulus produces a general increase in the mechanical properties of the whole composite (fig. 11).
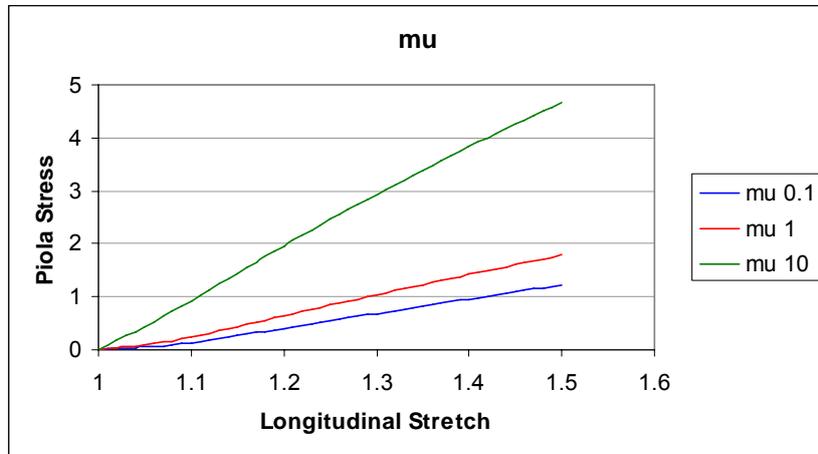

fig. 11 Stress-stretch plot. Effect of the matrix.

In general, a stiffer matrix increases the composite modulus at low strain, i.e. before the fibres are recruited and stretched. Of course, a very stiff matrix (respect to the fibre modulus) overwhelms the reinforcing effect caused by the fibres.

Transverse stretch of the composite is the result of two concomitant processes: matrix contraction and fibre recruitment. Stiffer matrices strongly affect the latter process: a rigid matrix hinders fibres reorientation thus causing a much lower transverse contraction (fig. 12).
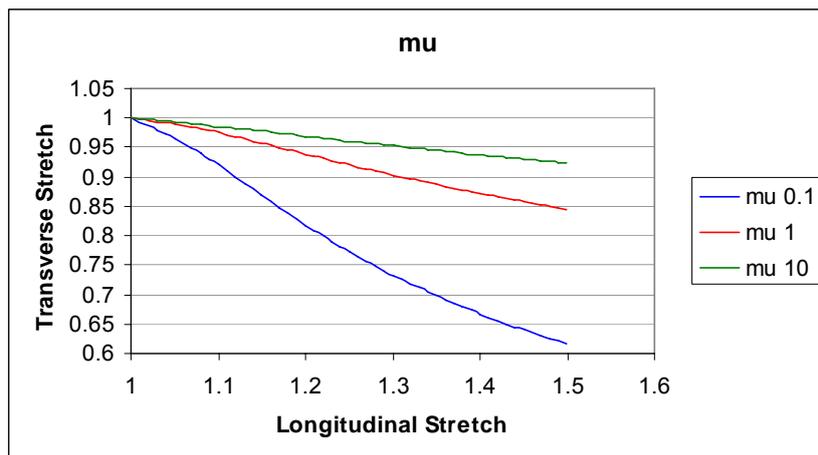
fig. 12 Transverse vs longitudinal stretch plot. Effect of the matrix.

Since the matrix has been modelled as a compressible material, the determinant of the deformation gradient is not constant and equal to one, but varies along with the deformation. Of course $J>1$ means a volumetric dilation, while $J<1$ indicates a contraction.
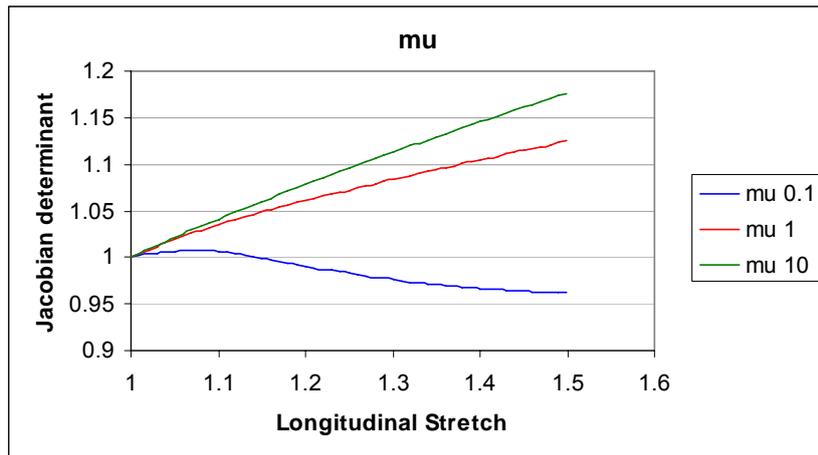
fig. 13 *J* vs longitudinal stetch plot. Effect of matrix.

The *J* – longitudinal stretch plot displays a minimum in the case of compliant matrices (m = 0.1) (fig. 13). An increase of λ_l is always observed whenever *J* have a local maximum, as depicted in the following diagram.
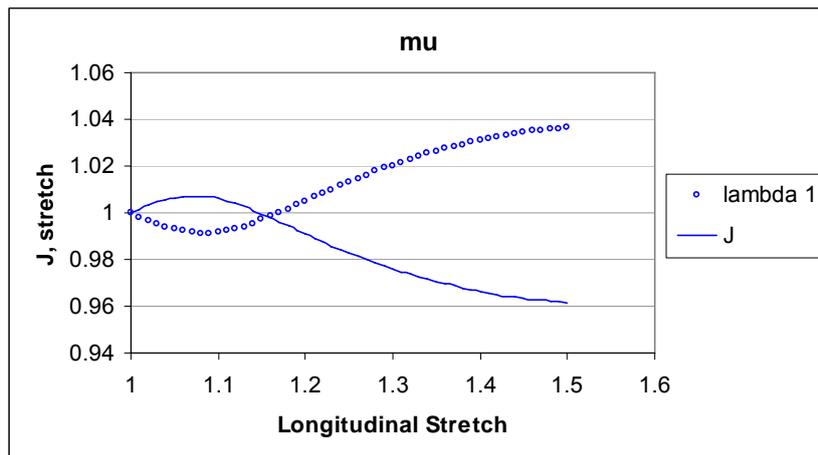

fig. 14 Thickness stretch and jacobian determinant vs longitudinal stretch.

The thickness of the composite starts to increase beyond a certain value of the axial stretch. However this specific prediction has never been confirmed by the experimental evidence.

The evolution of the angle of fibres direction in the deformed and reference configuration is reported in fig. 15.
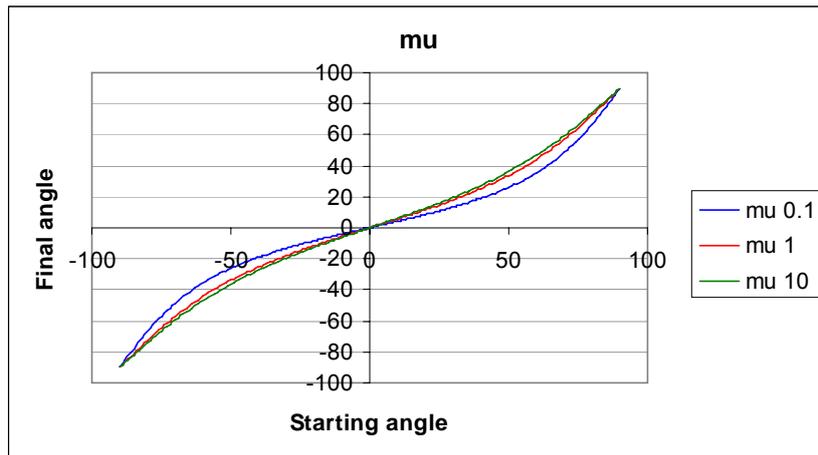
fig. 15 Evolution of fibre direction. Effect of the matrix.

Fibres oriented at a certain angle Θ in the reference configuration (horizontal axis in the figure) are rotated to a direction defined by an angle $\theta < \Theta$ in the current configuration. Also in this case, stiffer matrices hinder such movement, causing little fibre rearrangement.

The parameter β is intrinsically linked to matrix compressibility. It exerts little effect on both stress-strain response and fibre recruitment, as depicted in the following figures.
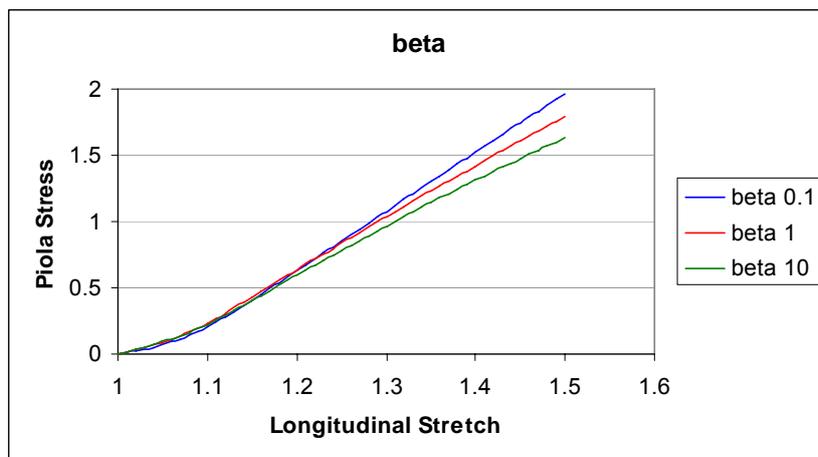
fig. 16 Stress-stretch plot. Effect of β.
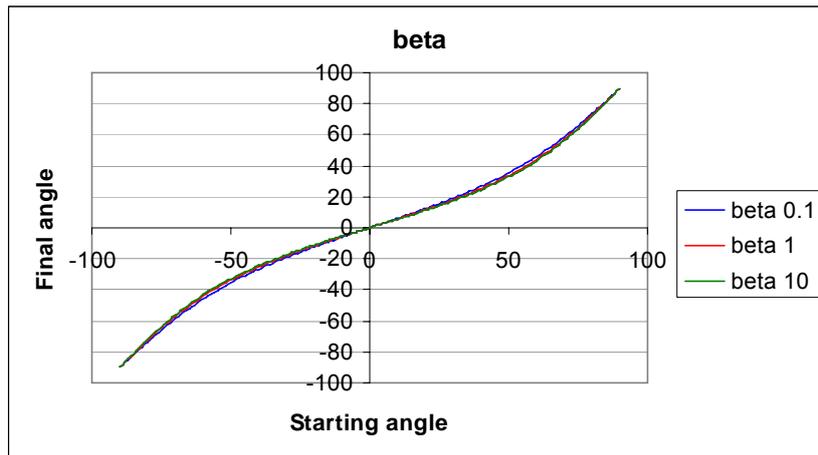
fig. 17 Evolution of fibre direction. Effect of β.

A very high value of β ($\beta = 10$) causes the material to be nearly incompressible. In this case, as expected $J \approx 1$.
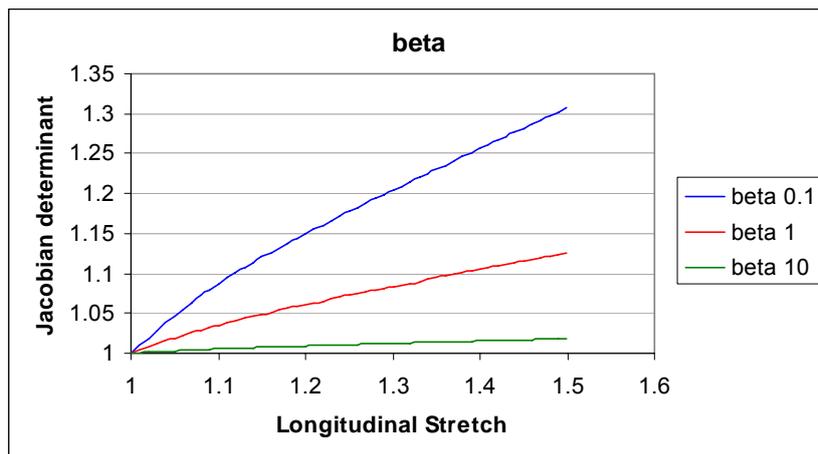

fig. 18 J vs longitudinal stetch plot. Effect of β.

The effect of β on transverse contraction is clearly shown in the picture below.
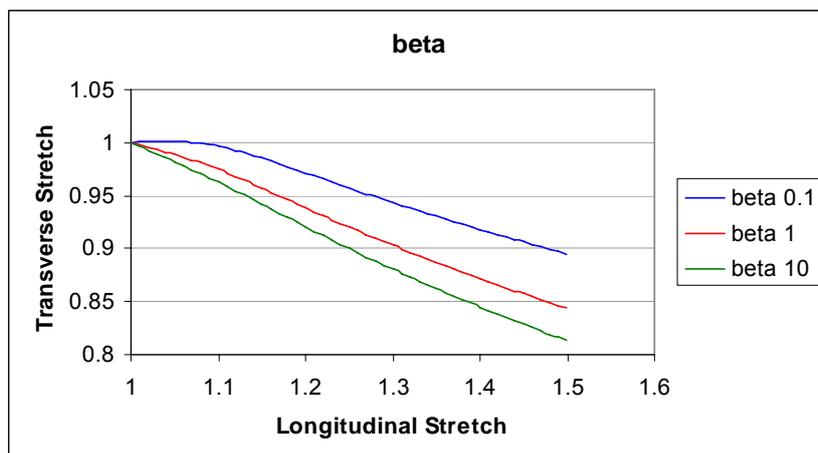
Composites with highly compressible matrices (β = 0.1) undergo volumetric dilation, up to a 10% of longitudinal deformation, without transverse contraction. Matrix transverse contraction becomes more significant for large β values.

The parameter k_1 and k_3 have been introduced in order to model fibre mechanical properties. An increase of the k_1 value enhances the early stress response of the fibres (fig. 20).
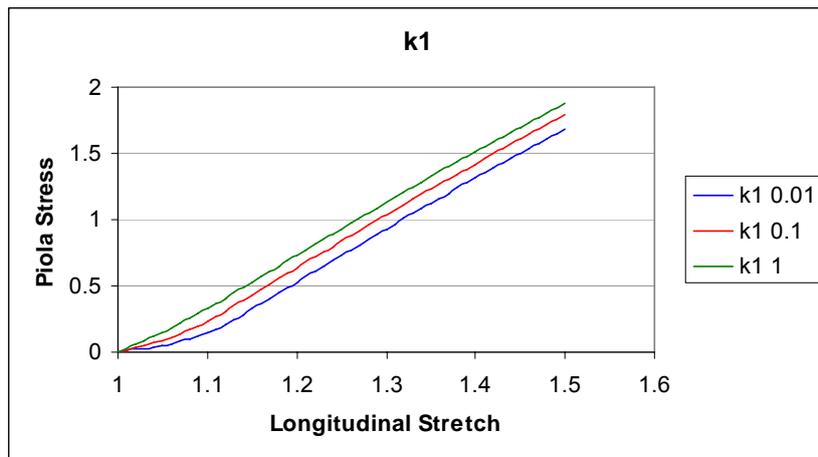

fig. 20 Stress-stretch plot. Effect of k_1.

Fibres having small k_1 display a lag in exerting their mechanical action, i.e. become active for larger value of λ. The slope of the linear region is of course the same, for the three values of k_1 since it is mainly determined by k_3 as depicted in fig. 21.
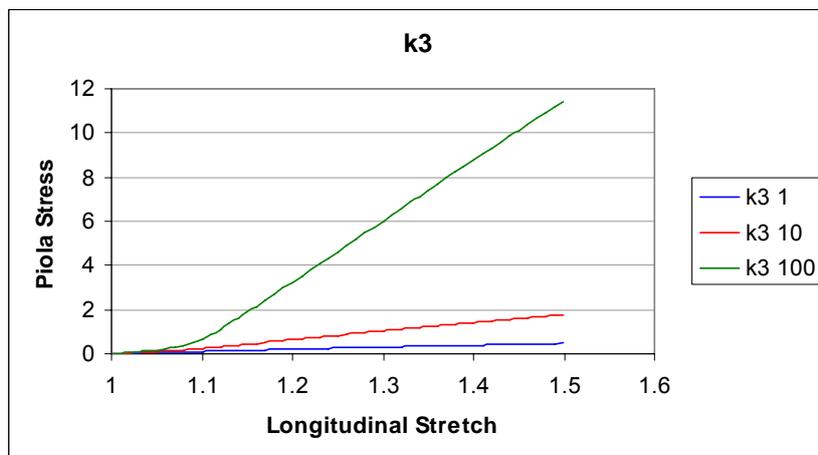

fig. 21 Stress-stretch plot. Effect of k_3.

The increase of the k_3 value produces dramatic effects on the composite transverse contraction
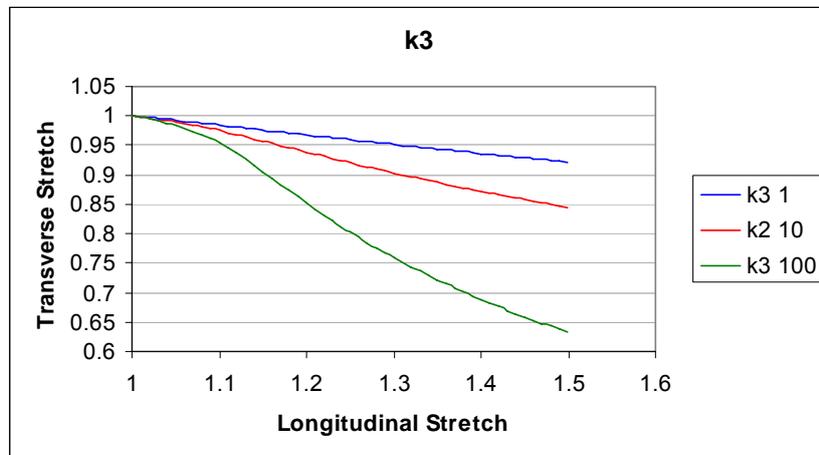

fig. 22 Transverse vs longitudinal stretch plot. Effect of k_3.

The jacobian determinant is strongly affected by variation of fibre stiffness as well. In particular J displays a maximum for large k_3 values.
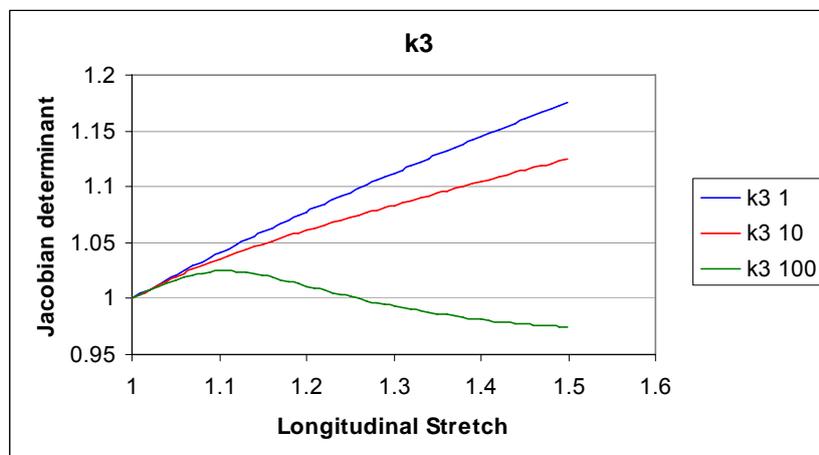

fig. 23 J vs longitudinal stetch plot. Effect of k_3.

Fibre volume fraction weighs the relative contribution of the matrix and fibres properties on the overall mechanical response of the composite. Thus an increase of fibre volume fraction produces analogous effects as a simultaneous increase of fibre mechanical properties and a decrease of matrix properties, as depicted in fig. 24.
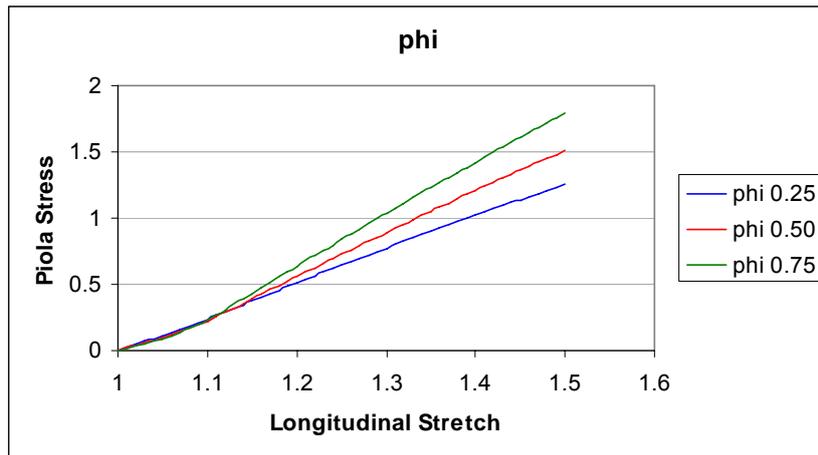
fig. 24 Stress-stretch plot. Effect of the fibre volume fraction.

The effect of fibre volume fraction on the fibre recruitment process is almost negligible, as reported in fig. 25.
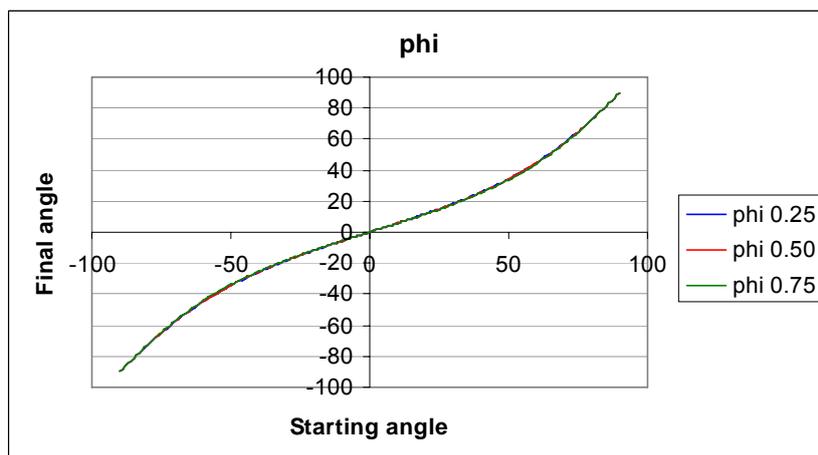

fig. 25 Evolution of fibre direction. Effect of the fibre volume fraction.

Fibre volume fraction does not affect the composite transverse stretch as well (fig. 26).
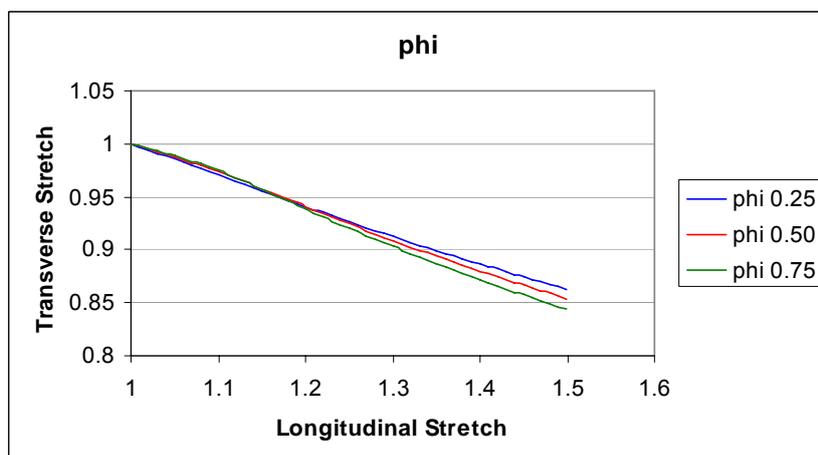
fig. 26 Transverse vs longitudinal stretch plot. Effect of the fibre volume fraction.

105

In conclusion, the numerical model presented so far accounts for very intriguing features: continuous distribution of fibres, transverse stress correction, matrix compressibility. In order to predict reticular dermis mechanical properties, an adequate set of material properties must be chosen. An optimization procedure of the parameters has been written in MATLAB. The procedure minimizes the following function:

$$R = \sum_i [(P_i - y_{1i})^2 + (\lambda_{2i} - y_{2i})^2]$$

where P_i and λ_{2i} are the predicted Piola stress and transverse stretch respectively, and y_1 and y_2 are the experimental Piola stress and transverse stretch respectively. In other words, the procedure minimizes the sum of the summed square residuals of both uniaxial stretching data and transverse contraction data. The function which has to be optimized is non linear and possesses 10 parameters, which make it very sensitive to the starting set of trial parameters. In order to reduce the set of parameters, it is assumed that the structural constants (Θ, σ_θ and ϕ_f) can be determined experimentally. Assuming that collagen fibres are distributed around the $\theta = 0°$ with an angular dispersion σ_θ of 45° and have a volume fraction of 80%, the optimization process provides the following set of material constants:

$$\mu = 0.93\,\text{MPa} \quad \beta = 2.51$$
$$k_1 = 0.035\,\text{MPa} \quad k_3 = 63.12$$
$$\lambda_{\text{lock}} = 1.12$$

The result of the mathematical model with this material constants is in good agreement with the experimental data as depicted in fig. 27 and fig. 28.
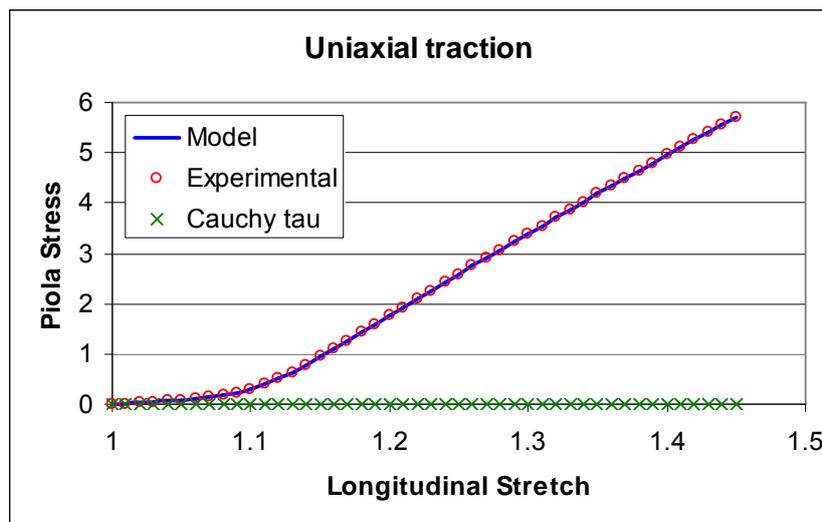

**fig. 27** Stress - stretch plot. Experimental and theoretical data
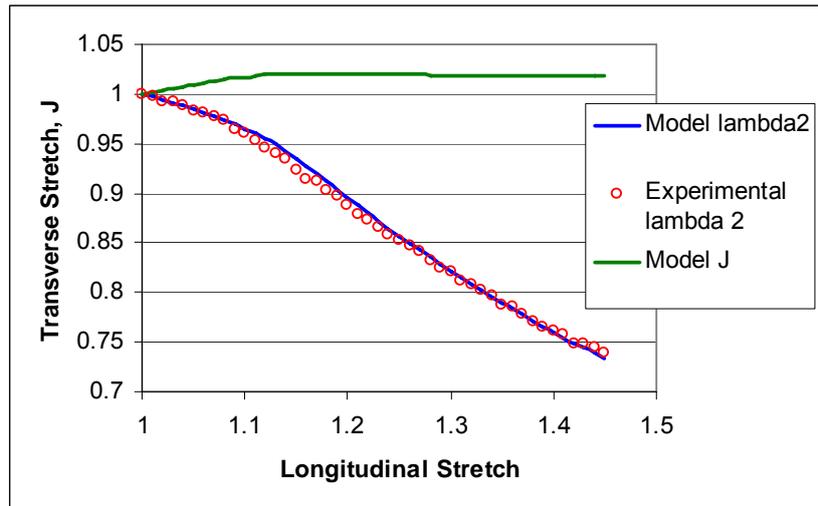
fig. 28 Transverse -longitudinal stretch. Experimental and theoretical data.
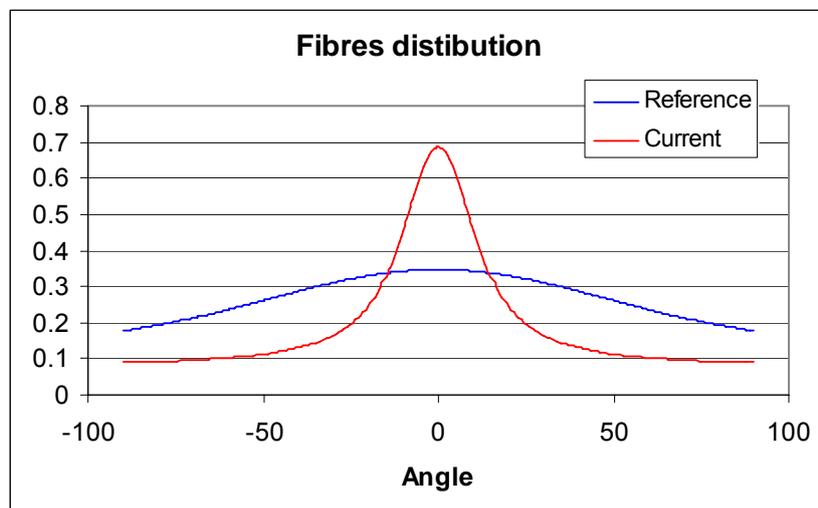

fig. 29 Theoretical fibre distribution in both reference and deformed configuration

Boote and coworkers [2], however, using high angle X-ray diffraction, were able to unravel collagen fibre distribution within wet blue leather. They discovered that fibre distribution of leather samples, taken from the butt area, is not symmetric, following a preferential direction of alignment which is oriented at 30° with respect to the backbone direction. Such result is consistent with the work of Osaki [3] who demonstrated by microwave method that in undeformed leather there is a position dependent preferred fibre run. Starting from these observations we have assumed that bovine reticular dermis could be schematized as a textile in which fibres have a preferential direction of running oriented at 20° with respect to the backbone direction with an angular dispersion σ_θ of 30°. A network of randomly (σ_θ=180°) aligned fibres is overlapped to the first family of fibres, which is a feature in agreement with the X-ray intensity distribution provided by the data of

Boote. The optimization process for the new fibre distribution provides the following set of material constants and curve fit:

$$\mu = 0.83 \, \text{MPa} \quad \beta = 2.45$$
$$k_1 = 0.007 \, \text{MPa} \quad k_3 = 62.98$$
$$\lambda_{\text{lock}} = 1.11$$
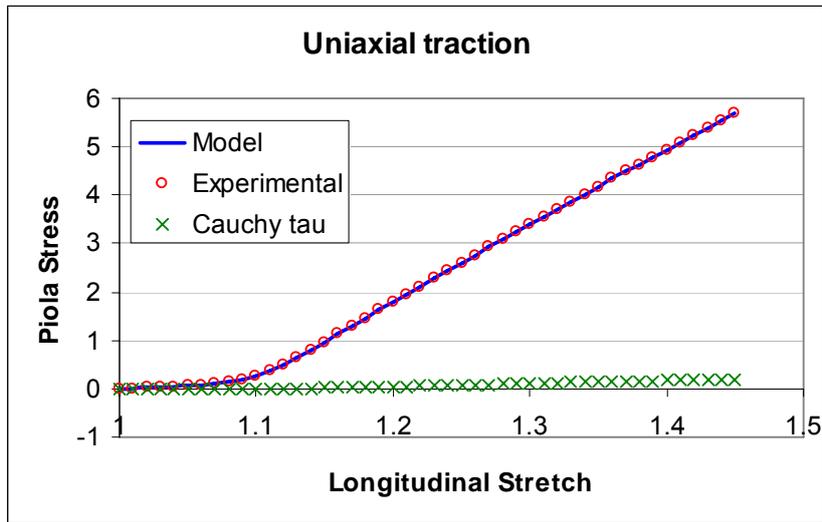
**fig. 30** Stress - stretch plot. Experimental and theoretical data
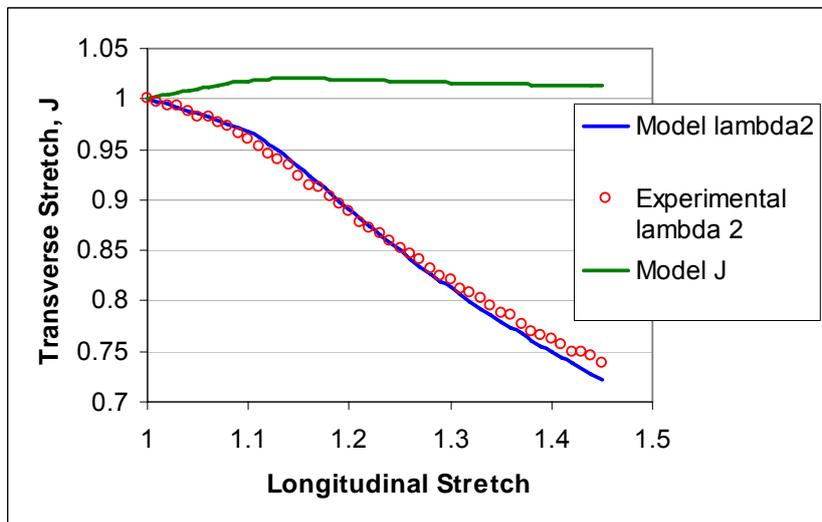
fig. 31 Transverse -longitudinal stretch. Experimental and theoretical data.
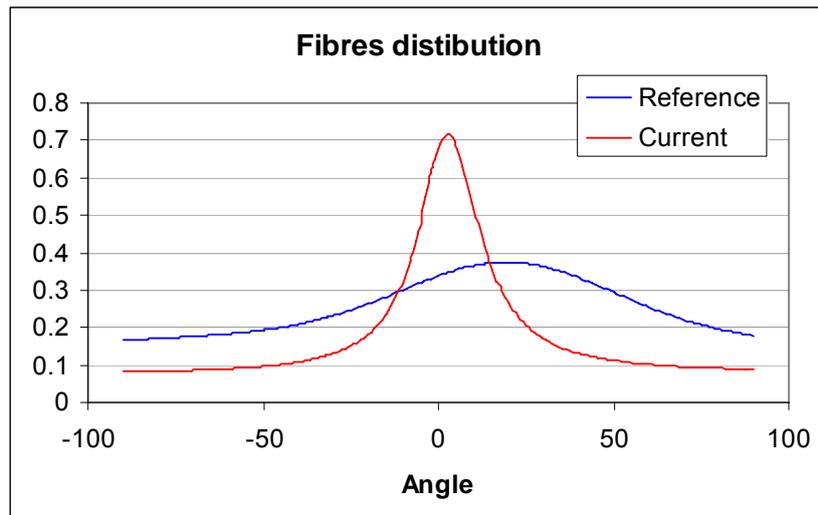
**fig. 32** Fibre distribution in both reference and deformed configuration

The results of the mathematical model are still in good agreement with experimental data. However it has to be pointed out that the model has been solved following a semi-inverse method. In the case of non symmetric distribution of collagen fibres, the deformation can no longer be assumed homogeneous: fibres having a large pitch undergo to a more extensive recruitment than fibres whose direction is closer to the sample longitudinal axis. Assuming a two-dimensional case, the correct solution of the problem should require a more general motion, e.g. of the form:

$$\begin{cases} x = f(X,Y)X \\ y = g(X,Y)Y \\ \quad z = \lambda Z \end{cases}$$ -29-

where the unknown functions f and g have to be determined by solving the set of non-linear partial differential equations provided by the equilibrium equations 25. However, since the shear stress engendered by the asymmetric fibre distribution is very small (less than 2% of the maximum value attained by the longitudianl Cauchy stress), it is reasonable to assume that the prediction provided by solving the numerical model with the semi inverse method, are still comparable with the data of the uniaxial test.

A limit of this model is that it predicts a swelling in the thickness direction for certain values of the material constants. This has been shown above (fig. 13, fig. 23) as a maximum in the J - longitudinal stretch diagrams. However the experimental data provided by videoextensomety tests have not confirmed such prediction. This feature of this model has also been observed by Gasser and others [15] who developed an anisotropic hyperelastic model for arterial layers. They also reported finite element computations of

uniaxial tension test, on an arterial wall, in which an extensive swelling in thickness direction was evident in their simulation.
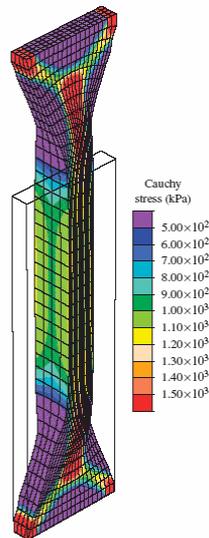
fig. 33 Finite element computation of a uniaxial tension test on a arterial strip. Note the extensive increase of thickness. Modified from [15].

They ascribed the origin of this phenomenon to fibre rotation which causes matrix to be squeezed out. However, fibres have not been modelled as elements having finite dimension, they just act as immaterial reinforcement along a specific direction. It is unlike that such an entity can actually squeeze the matrix out. We would rather stipulate that the increase in thickness is due to a boundary effect. Since the boundary is unloaded, the overall stress on a composite element at the boundary must be zero. However the fibre can just carry to load along its direction. All other loads which do not lay along the fibre direction have to be balanced by the matrix.
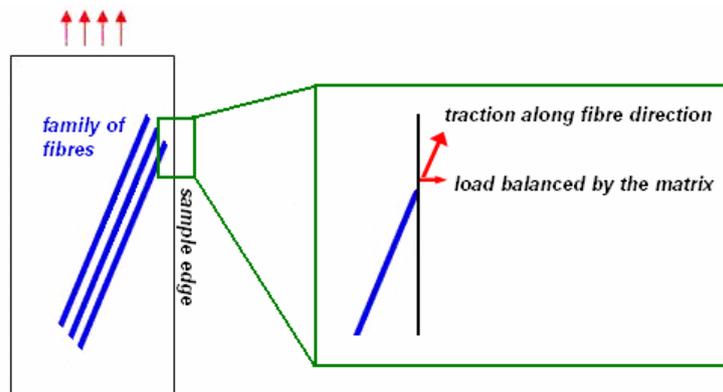

fig. 34 Schematic of the uniaxial test. Equilibrium at the edge of the specimen.

The matrix turns out to be compressed, which is a condition that ensures the equilibrium at the boundary. This phenomenon is even more evident in the case of very stiff fibres and/or compliant matrices (see fig. 13 and fig. 23).

In order to avoid this problem, the model should take into account the actual fibre-matrix interface and the ability of the fibres to withstand load in the transverse direction. Following the work of Gasser and others, fibre strain energy function, in the i-th direction, can be written in the form

$$\psi_f^i = \frac{k_1}{2k_2}\left[e^{\left\{k_2\left[kI_1+(1-3k)I_4^i-1\right]^2\right\}} - 1\right]$$
-30-

Fibre stress is then not only a function of I_4 and thus of the fibre stretch, but also depends on I_1, whose effect is weighted by a factor k. The fibre can then exert a mechanical response even if it is not stretched along its direction. However, Gasser and coworkers gave a different interpretation based on geometrical considerations of the parameter k: it is a dispersion parameter which characterizes the distribution of fibres around an "average" value. In fact, in the case of $k=0 \Rightarrow \psi_i = \psi_i(I_4^i)$ which coincides with the i-th family of fibres having a single direction of run. On the other hand $k = \frac{1}{3} \Rightarrow \psi_i = \psi_i(I_1)$ which corresponds to an isotropic distribution. In this case the composite is schematized as a mixture of two isotropic materials. The model, on the basis of this hypotheses, predicts an overall isotropic mechanical response (see below).

A parametric study of the Gasser's model has been performed in order to assess the effect of the parameter k on the predicted mechanical properties. The constitutive equation is based on this assumptions: the matrix is a compressible Blatz-Ko material; there are only two families of fibres oriented along two symmetric directions; fibre strain energy function have the specific form of equation 30.

The base case is defined by the following set of material parameters:

$$\mu = 1 \quad \beta = 1 \quad \varphi = 0.75$$

$$k_1 = 1 \quad k_2 = 1 \quad \vartheta = \frac{\pi}{6}$$

the parameter k has been varied in the [0, 0.3] interval with 0.1 increments. Of course, an increment in k is equivalent to a decrease in the anisotropic contribution caused by the effect of I_4 on the composite strain energy function. In the limit of $k \to \frac{1}{3}$, the model predicts an isotropic behaviour of the composite. This is shown in the stretch-stress plot (fig. 35) where the effects of fibre recruitment and fibre stretching almost vanish for $k=0.3$.
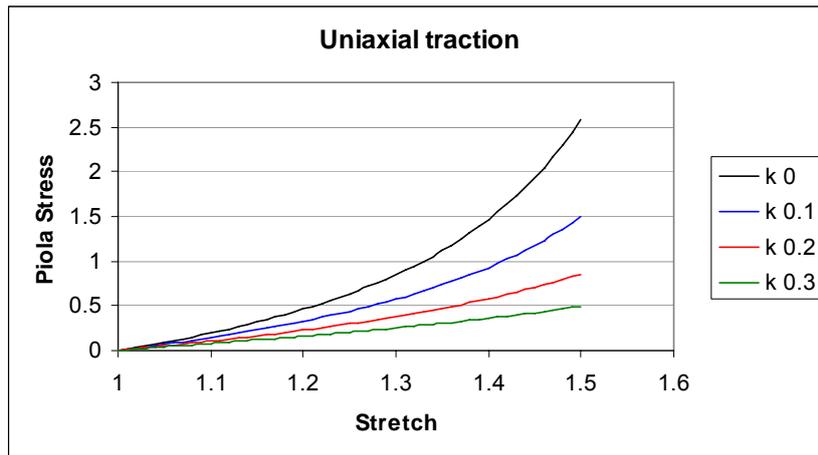
fig. 35 Stretch-stress diagram. Effect of k.

An increase of k has the beneficial effect of a more realistic prediction of the volumetric changes during uniaxial test. The increase in swelling which has been previously documented is strongly reduced in the case of k=0.3, as depicted in fig. 36.
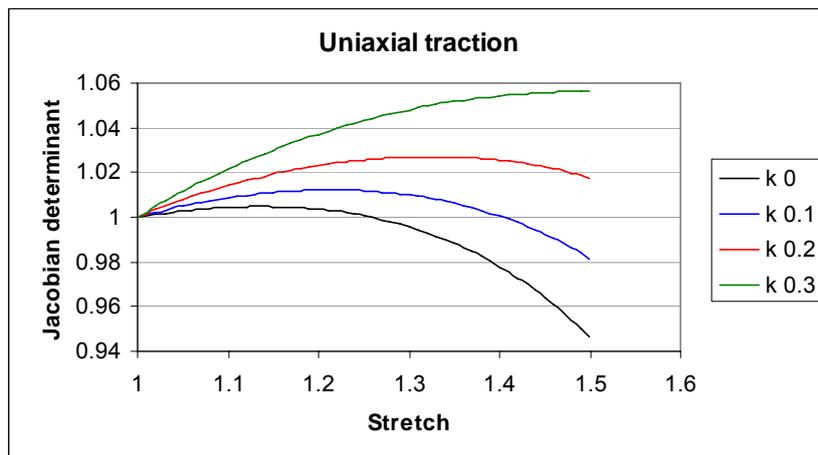
fig. 36 J - stretch diagram. Effect of k.

However the problem related to thickness swelling has not been completely cancelled. The maximum displayed by the J-stretch plot is shifted toward higher stretch as k increases. Higher values of k are then desirable in order to avoid thickness increase, on the other hand, large k value entails a loss of information on the anisotropy of the material.

5. Conclusions

The aim of this chapter was to present a constitutive model for bovine dermis. An experimental characterization of partially processed bovine dermis has been undertaken. Stress – strain response and the local mechanisms of deformation have been studied with the help of videoexensometric technique. In particular, novel deformation mechanisms of papillary dermis have been outlined. The peculiar deformation pathway could arise from the heterogeneous arrangement of collagen fibres within the papillary stratum. We focused our attention on the development of a mathematical model for reticular dermis, owing to the peculiar non homogeneous deformation of papillary dermis and the lack of accuracy of experimental data. The solution of a three dimensional problem with non homogeneous deformation, brings in additional numerical complexity. This requires more sophisticated numerical tools (like the finite element method) rather than semi-inverse method, in order to provide a more accurate prediction.

The model we have presented possesses some interesting features like:

- it is a structural model
- predicts mechanical response at finite deformation
- accounts for a (modest) fibre-matrix interaction in transverse direction
- accounts for a continuous distribution of collagen fibres.

The model has 8 material parameters (provided that fibre distribution is symmetric). However structural parameters (i.e. Θ, σ_θ and ϕ_f) could be determined with independent experiments. Thus only 5 constants have been varied to demonstrate the ability of the model to capture the mechanical response of reticular dermis. The results provided by the model are in good agreement with the experimental data, i.e. both the stress strain curve in uniaxial tension and the transverse contraction in the same test. However the numerical model fails to predict the actual deformation along the thickness direction. In particular, it has been shown that, for a certain set of material constants, the model predicts an increase in thickness with axial deformation. It is likely that this behaviour arises from the fibre strain energy function rather than matrix squeezing caused by fibre recruitment. A different form of the fibre strain energy function has been considered, which introduces an isotropic contribution to the overall composite mechanical response. Such strain energy function seems to hide the problem related to thickness increase but even with this correction the problem is not completely eliminated. It is the opinion of the author that a

different volume averaging procedure, other than the rule of mixtures, would help in solving such a problem.

In summary the constitutive model can be considered as a starting attempt for developing a three dimensional hyperelastic constitutive model, able to capture the mechanical response of a full thickness dermis.

6. References

1. Billiar K.L, Sacks M.S.: "A method to quantify the fiber kinematics of planar tissues under biaxial stretch". *Journal of Biomechanics* **30**, 753 - 756, 1997.

2. Boote C., Sturrock E.J., Attenburrow G.E., Meek K.M.:"Psuedo-affine behaviour of collagen fibres during the uniaxial deformation of leather". *Journal of Material Science* **37**, 3651 - 3656, 2002.

3. Osaki S.: "Distribution map of collagen fiber orientation in a whole calf skin". The Anatomical Record 254, 147 - 152, 1999.

4. Raspanti M., Manelli A., Franchi M., Ruggeri A.: "The 3D structure of crimps in the rat Achilles tendon". *Matrix Biology* **24**, 503 - 507, 2005.

5. Lewis G., Shaw K.M.: "Modeling the tensile behavior of human Achilles tendon". *Biomedical materials and engineering* **7**, 231 - 244, 1997.

6. Hirokawa S, Tsuruno R.:"Hyper-elastic model analysis of anterior cruciate ligament". *Medical Engineering and Physics* **19**, 637 - 651, 1997.

7. Holzapfel G.A., Gasser T.C. and Ogden R.W.: "A new constitutive framework for arterial wall mechanics and a comparative study of material models". *Journal of Elasticity* **61**, 1 - 48, 2000.

8. Driessen N.J., Boerboom R.A., Huyghe J.M., Bouten C.V., Baaijens F.P.: "Computational analyses of mechanically induced collagen fiber remodeling in the aortic heart valve". *Journal Biomechanical Engineering* **125**, 549 - 557, 2003.

9. Holzapfel G.A.: "Nonlinear Solid Mechanics: A Continuum Approach for Engineering". *Wiley*, 2000.

10. Bonet J., Wood R.D.: "Nonlinear Continuum Mechanics for Finite Element Analysis". *Cambridge University Press*, 1997.

11. Flory P.J.: "Thermodynamic relations for high elastic materials". *Transactions of the Faraday Society* **57**, 829 – 838, 1961.

12. Spencer A.J.M.: "Theory of invariants" in: A.C. Eringen, (Ed.), Continuum Physics, Vol. 1, *Academic Press*, 1971.

13. Driessen N.J., Bouten C.V., Baaijens F.P.:" A structural constitutive model for collagenous cardiovascular tissues incorporating the angular fiber distribution". *Journal of Biomechanical Engineering* **127**, 494 - 503, 2005.

14. Ionescu I., Guilkey J., Berzins M., Kirby R.M., Weiss J.: "Computational simulation of penetrating trauma in biological soft tissues using the material point method". *Studies in health technology and informatics* **111**, 213-218, 2005.

15. Gasser T.C, Ogden R.W, Holzapfel G.A.: "Hyperelastic modelling of arterial layers with distributed collagen fibre orientations". *Journal of the Royal Society. Interface* **3**, 15-35, 2006.

Chapter 4

Mathematical model for the viscoelastic behaviour of dermis

1. Introduction

The experimental evidence indicates that the mechanical response of soft collagen rich biological tissues is nonlinear, anisotropic and viscoelastic. Tissues display viscoelasticiy is several ways, creep, stress relaxation preconditioning and strain softening. In particular the microconstituents of biological tissues are subjected to rearrangements during cyclic loading and the extent of such movements is more severe during the first cycles of loading-unloading. Of course all these constitutive features, both elastic and viscoelastic, are strictly related to the microstructure of the tissue of interest. An efficient structural constitutive model should capture the above mentioned characteristics.

A mathematical model based on the continuum mechanics framework, which captures both the non linear and anisotropic mechanical response of reticular dermis, has been presented in the previous chapter. However, in order to get a more complete description of the dermal mechanical properties, viscoelasticity must be taken into account.

As pointed out in the previous chapter, the anisotropic and non linear behaviour of soft tissues has been modelled using a wide variety of phenomenological or structural approaches. However modelling the time dependent behaviour brings in an additional level of numerical complexity, since the introduction of viscoelasticity necessarily involves additional material constants and/or functions. The determination of such parameters and functions often requires experimental fitting of a large numbers of time-dependent functions.

Even though viscoelasticity is strongly tissue-dependent, it can be generally classified in three broad areas. Since tissues are highly hydrated, viscoelasticity arises from viscous fluid flow through network fibres as the tissue is deformed. Additionally, individual ECM constituents intrinsically display time-dependent behaviour (like collagen bundles and elastic fibres) which contributes to the viscoelasticity of the whole tissue. Finally, as it has been pointed out in Chapter 2, collagen rich tissues possess many physical crosslink and entanglements which are transient, in the sense that they can be disrupted and eventually reformed during cyclic deformations.

Several theories have been developed for modelling viscoelasticity of soft tissues. Multyphasic and poroelastic models have been developed in order to predict the mechanical response of tissues in which the dissipation is mainly determined by fluid flow [1]. The Quasi-Linear Viscoelasticity (QLV) is a hereditary integral formulation, characterized by an instantaneous elastic response and a relaxation function that governs the fading memory of the current state [2]. The state variable approach postulates a Helmholtz free-energy function which defines the thermodynamic state by an (observable) external variable (the deformation gradient or a deformation tensor, for example) and a set of additional internal variables which describes the dissipation mechanism of the material and have to be specified for the problem of interest. The set of equations representing the internal variable model must be complemented by a kinetic relation which describes the evolution of the internal variables and thus of the dissipation mechanism. Internal variables models can be recast as rheological network models in which a discrete number of elastic and viscous elements are arranged in parallel and/or in series. It must be pointed out that the use of the term rheological network does not have any microstructural meaning such as interconnecting matrix macromolecules or fibres, it rather refers to a set of law which govern the temporal evolution of the non-equilibrium stresses.

The goal of the present chapter is the description of an anisotropic hyperviscoelastic constitutive model for dermis based on the internal variables constitutive framework proposed by Holzapfel [3, 4]. The model has been obtained by postulating a particular anisotropic Helmholtz free-energy function which schematizes the tissue as a composite material with two families of fibres. All the compounds, both the matrix and the fibres, are considered to have a viscoelastic behaviour.

2. Constitutive framework

2.1. Basic kinematics of finite viscoelastic deformations

The basic kinematics is governed by the same equations presented in Chapter 3 for finite elastic deformations. In particular, a multiplicative decomposition of the deformation gradient into a volume changing (dilational) and isochoric (distortional) parts is assumed. As previously stated, in order to describe the viscoelastic behaviour, a set of internal variables is introduced [3]. These additional variables are second order tensorial functions which describe the internal irreversible dissipative effects which occur as the viscoelastic material is deformed. Internal variables depend on the deformation history and are related to a strain measure and characterize the non equilibrium state of the deformation process. However, when the system tends toward a state of thermodynamic equilibrium all the internal variables must vanish.

2.2. Decoupled volumetric-isochoric stress response

The anisotropic elastic behaviour of dermis could be conveniently described within the framework of hyperelasticity using a strain energy function, which is a scalar valued function of the tensor variables $\boldsymbol{C}$ (right Cauchy-Green deformation tensor), $\boldsymbol{A}_0$ and $\boldsymbol{G}_0$ (structural tensors describing fibres arrangement). In order to describe the history of deformation a set of m internal (second order) tensorial variables, denoted by Γ_1, …, Γ_m, is introduced. The experimental evidence suggests that the deformation mechanism of soft biological tissues is almost isochoric. Starting from this observation, a decoupled representation of the free energy function is proposed which describes separately volumetric and isochoric contributions.

$$\Psi(\boldsymbol{C}, \boldsymbol{A_0}, \boldsymbol{G_0}, \Gamma_1, ..., \Gamma_m) = \Psi_{vol}^{\infty}(J) + \Psi_{iso}(\overline{\boldsymbol{C}}, \boldsymbol{A_0}, \boldsymbol{G_0}, \overline{\Gamma}_1, ..., \overline{\Gamma}_m) \qquad \text{-1-}$$

The second order tensorial variables Γ_α are function of the distorsional part of the modified Cauchy-Green deformation tensor $\overline{\boldsymbol{C}}$. In equation 1 it is assumed that viscoelasticity arises from purely isotropic deformations. All volume changing deformations are forced to be reversible. Hence the superscript ∞ refers to functions which describe the equilibrium elastic response. In addition, the isochoric free energy term Ψ_{iso} is decoupled into an equilibrium part (describing the isochoric elastic response at $t \to \infty$) and into configuration free energies responsible for the thermodynamic non-equilibrium state of the material. In symbol

$$\Psi_{iso}(\overline{\boldsymbol{C}},\boldsymbol{A_0},\boldsymbol{G_0},\overline{\Gamma}_1,...,\overline{\Gamma}_m) = \Psi_{iso}^{\infty}(\overline{\boldsymbol{C}},\boldsymbol{A_0},\boldsymbol{G_0}) + \sum_{\alpha=1}^{m}\gamma_{iso\alpha}(\overline{\boldsymbol{C}},\boldsymbol{A_0},\boldsymbol{G_0},\overline{\Gamma}_\alpha) \qquad \text{-2-}$$

The m scalar valued functions γ_{iso} represent the dissipative internal rearrangements which occur in the material during deformation. As mentioned in Chapter 3, a fundamental requirement for strain energy functions is that they must material frame indifferent. Thus Ψ_{iso}^{∞} can be expressed as a function of the seven modified scalar invariants $\overline{I}_a = J^{-2/3}I_a$, a= 1,2,4,…,8. Equation 2 becomes

$$\Psi_{iso} = \Psi_{iso}^{\infty}(\overline{I}_1,\overline{I}_2,\overline{I}_4,...,\overline{I}_8) + \sum_{\alpha=1}^{m}\gamma_{iso\alpha}(\overline{\boldsymbol{C}},\boldsymbol{A_0},\boldsymbol{G_0},\overline{\Gamma}_\alpha) \qquad \text{-3-}$$

For numerical purposes, however, the invariants $\overline{I}_5,\overline{I}_7,\overline{I}_8$ will be neglected and no longer considered.

According to Holzapfel [3], the second Piola-Kirchhoff stress tensor can be written as

$$\boldsymbol{S} = \frac{\Psi(\boldsymbol{C},\boldsymbol{A_0},\boldsymbol{G_0},\Gamma_1,...,\Gamma_m)}{\partial \boldsymbol{C}} = \boldsymbol{S}_{vol}^{\infty} + \boldsymbol{S}_{iso} \qquad \text{-4-}$$

The stress quantities are defined as follows

$$\boldsymbol{S}_{vol}^{\infty} = J^{-2/3}p\boldsymbol{C}^{-1}$$

$$\boldsymbol{S}_{iso} = \boldsymbol{S}_{iso}^{\infty} + \sum_{\alpha=1}^{m}\boldsymbol{Q}_\alpha \qquad \text{-5-}$$

which describe the volumetric and isochoric contributions. The scalar p is the hydrostatic pressure. The additive decomposition of the isochoric stress tensor in equilibrium and non-equilibrium parts, follows the equation

$$\boldsymbol{S}_{iso}^{\infty} = J^{-2/3}\mathbb{P}:\hat{\boldsymbol{S}}^{\infty}, \quad \hat{\boldsymbol{S}}^{\infty} = 2\sum_{a=1,2,4,6}\frac{\Psi_{iso}^{\infty}(\overline{I}_1,\overline{I}_2,\overline{I}_4,\overline{I}_6)}{\partial \overline{I}_a}\cdot\frac{\partial \overline{I}_a}{\partial \overline{\boldsymbol{C}}} \qquad \text{-6-}$$

$$\boldsymbol{Q}_\alpha = J^{-2/3}\mathbb{P}:\hat{\boldsymbol{Q}}_\alpha, \quad \hat{\boldsymbol{Q}}_\alpha = 2\frac{\partial\gamma_{iso\alpha}(\overline{\boldsymbol{C}},\boldsymbol{A_0},\boldsymbol{G_0},\overline{\Gamma}_\alpha)}{\partial \overline{\boldsymbol{C}}} \quad \alpha=1,2,...,m \qquad \text{-7-}$$

The fourth order tensor $\mathbb{P}= \mathbb{I} -\frac{1}{3}\boldsymbol{C^{-1}}\otimes\boldsymbol{C}$ defines a projection tensor which gives rise to the deviatoric operator in the material description. The non equilibrium part $\boldsymbol{Q}$ characterizes the current distance from equilibrium. At equilibrium the tensors $\boldsymbol{Q}$ vanish and finite elasticity is thus recovered.

2.3. Evolution equations and their solutions

The evolution of viscoelastic processes is governed by a set of differential equations. In other words, these differential equations specify how the isochoric non-equilibrium stress

evolves. The evolution equations must have a physical basis and have to provide a good approximation to the experimental evidence. A suitable choice seems to be a non-linear three-dimensional generalization of the Maxwell model. For each internal variable it has the form of

$$\dot{\boldsymbol{Q}}_{\alpha a} + \frac{\boldsymbol{Q}_{\alpha a}}{\tau_{\alpha a}} = \beta_{\alpha a}^{\infty} \dot{\boldsymbol{S}}_{isoa}^{\infty} \quad \alpha = 1,2,...m \quad a = 1,2,4,6 \qquad \text{-8-}$$

with starting condition $\boldsymbol{Q}_{\alpha a}^{0^+} = (J^{-2/3} \mathbb{P} : \hat{\boldsymbol{Q}}_{\alpha a})\big|_{t=0^+}$. However, assuming a stress free reference configuration, the starting condition becomes $\boldsymbol{Q}_{\alpha a}\big|_{t=0^+} = \boldsymbol{O}$. The $m+4$ material parameters β are related to the $m+4$ relaxation times τ. Equation 8 is valid in the hypothesis of small strain rates. Closed form solution of equation 8 is

$$\boldsymbol{Q}_{\alpha a} = e^{-\frac{T}{\tau_{\alpha a}}} \boldsymbol{Q}_{\alpha a}^{0^+} + \int_{t=0^+}^{t=T} e^{-\frac{T-t}{\tau_{\alpha a}}} \beta_{\alpha a}^{\infty} \dot{\boldsymbol{S}}_{isoa}^{\infty}(t) \mathrm{d}t \qquad \text{-9-}$$

We now seek for an algorithm which solves the convolution integral 9. An efficient procedure is the update algorithm proposed by Taylor [5] and recently reviewed by Holzapfel and Gasser [6].

Let $[t_n, t_{n+1}]$ be a subset of the closed interval $[0^+, T]$. Assuming that all kinematic quantities are know at t_n and t_{n+1}, and that stress $\boldsymbol{S}_n$ at t_n is determined through the associated constitutive equation. Thus $\boldsymbol{S}_n$ serves as starting database for the computation of all the remaining quantities

$$\boldsymbol{S}_{n+1} = \left(\boldsymbol{S}_{vol}^{\infty} + \boldsymbol{S}_{iso}^{\infty} + \sum_{\alpha=1}^{m} \boldsymbol{Q}_{\alpha} \right)_{n+1} \qquad \text{-10-}$$

The first two terms $\boldsymbol{S}_{vol\,n+1}^{\infty}$ and $\boldsymbol{S}_{iso\,n+1}^{\infty}$ are easily evaluated from equations 5.1 and 6 once the strain at t_n is known. The non equilibrium stress is evaluated from the convolution integral 9. Using the mid point rule, i.e. the time variable t in the $[t_n, t_{n+1}]$ interval is approximated by $\dfrac{t_{n+1} + t_n}{2}$, the non equilibrium stress at $t = t_{n+1}$ is given by

$$\boldsymbol{Q}_{\alpha\,n+1} = \mathscr{H}_{\alpha\,n} + \sum_{a=1,2,4,6} (\boldsymbol{Q}_{\alpha a})_{n+1} \quad \alpha = 1,2,...m \qquad \text{-11-}$$

which is usually referred as recurrence update formula for the non equilibrium stress. The tensor function $\mathscr{H}$ is the history term and has the following form

$$\mathscr{H} = \sum_{a=1,2,4,6} e^{-\frac{\Delta t}{2\tau_{\alpha a}}} [e^{-\frac{\Delta t}{2\tau_{\alpha a}}} (\boldsymbol{Q}_{\alpha})_n - \beta_{\alpha a}^{\infty} (\boldsymbol{S}_{isoa}^{\infty})_n] \qquad \text{-12-}$$

It is completely characterized by $\boldsymbol{Q}_{\alpha\,n}$ and $\boldsymbol{S}_{iso\,n}^{\infty}$ which have been determined in the previous step and serve as starting data base for the computation of the dynamic quantities at t_{n+1}. In equations 11 and 12 the following definition has been used

$$\left(\boldsymbol{Q}_{\alpha}\right)_{n+1} = \beta_{\alpha a}^{\infty} e^{-\frac{\Delta t}{2\tau_{\alpha a}}} \left(\boldsymbol{S}_{isoa}^{\infty}\right)_{n+1}$$

-13-

3. Numerical examples

In contrast to the classical models based on the phenomenological approaches the proposed three dimensional model has been developed on a structural approach. This leads to the main advantage that all the tensorial entries have a direct physical meaning. For connective tissues like skin, the tensors $\boldsymbol{S}_{vol}^{\infty}$ and $\boldsymbol{S}_{iso}^{\infty}$ describe the equilibrium stress exerted by the stable (but distorted) elastic and collagen networks. The tensors $\boldsymbol{Q}_{\alpha}$ in turn, are non equilibrium tensors and take into account configurational changes which occurs during deformation. In particular these tensors can be interpreted as descriptors of the (isotropic) proteoglycan reticulum brake down, and the loss of elastic recoil caused by collagen-elastin disentanglement. Moreover collagen fibres, which are the main responsible for the anisotropic mechanical response, exhibit their own viscoelasticity [2].

Three sets of results are presented here to demonstrate the features and performance of the model. First, the response of the model to uniaxial deformation is presented in order to demonstrate the effect of preconditioning on both stress-strain curves and transverse contraction. Secondly a parametric study has been performed focusing on the effects of key parameters that are related to the non equilibrium stress, namely τ and β and the deformation period T. Finally numerical solution of the model has been compared to the experimental results provided by cyclic tension tests performed on kid skin (see Chapter 2).

For all the three cases, the matrix is assumed to be an incompressible Mooney-Rivlin material whose (equilibrium) strain energy function is given by

$$\Psi_{iso}^{\infty}(\overline{I}_1,\overline{I}_2) = \frac{c_1}{2}(\overline{I}_1 - 3) + \frac{c_2}{2}(\overline{I}_2 - 3) \qquad \text{-14-}$$

The energy stored by collagen fibres is governed by the exponential function suggested by Billiar and Sacks [7]

$$\Psi_{iso}^{\infty}(\overline{I}_4,\overline{I}_6) = \frac{k_1}{2k_2}[e^{(\overline{I}_4-1)^2} - 1] + \frac{k_1}{2k_2}[e^{(\overline{I}_6-1)^2} - 1] \qquad \text{-15-}$$

The viscoelastic response of the fibre reinforced composite is modelled by the use of a single relaxation process (α=1 in equation 2) with corresponding relaxation times τ_1, τ_2 and τ_4 and free energy factors β_1, β_2 and β_4.

The material constants used in these simulations are as follows:

$$c_1 = 0.01 \, \text{MPa} \quad c_2 = 0.001 \, \text{MPa}$$
$$k_1 = 0.01 \, \text{MPa} \quad k_2 = 10$$
$$\varphi_f = 0.15 \quad \vartheta = \frac{\pi}{9}$$
$$\tau_1 = \tau_2 = 10 \, \text{s} \quad \tau_4 = 1 \, \text{s}$$
$$\beta_1 = \beta_2 = 10 \quad \beta_4 = 10$$

unless otherwise stated.

The strain input is a triangular wave (3 periods of 0.1 Hz and 1.2 amplitude, unless otherwise stated).

3.1 Preconditioning

The simulation has been performed using a triangular wave stretch input (5 periods at 0.1 Hz). fig. 1 shows the stress strain response of the constitutive model to the periodic stretch input.
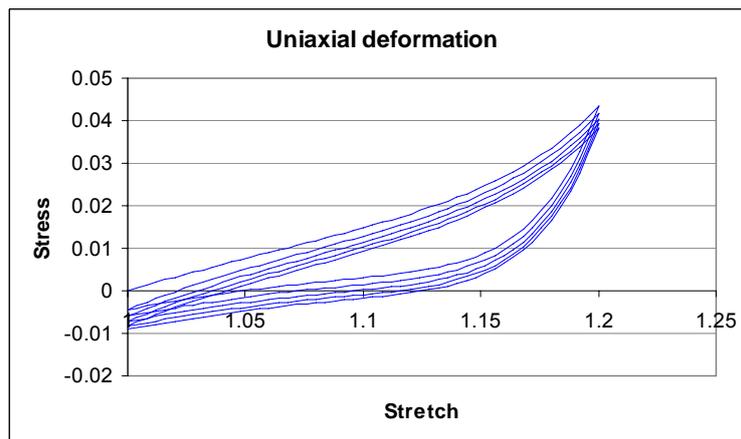
fig. 1 Response of the constitutive model to cyclic uniaxial deformation.

Viscoelasticity appears in the starting cycle as there is substantial hysteresis. The model response in subsequent cycles becomes increasingly more compliant and the amount of hysteresis significantly decreases, as well as the peak stress as depicted in the bar diagram of fig. 2, where the simulation has been extended to 10 cycles.

124
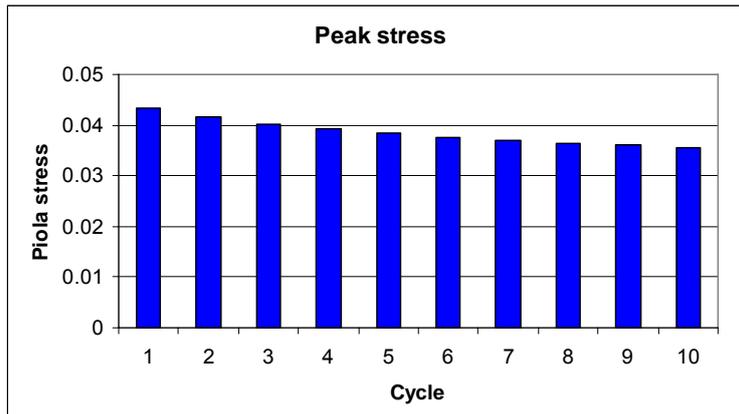
fig. 2 Peak stress decay with loading cycle

A feature of this model is that it is fully three dimensional. It is then possible to gain information concerning stress and deformations along the three material axes. In the transverse-longitudinal stretch plot the effect of preconditioning is less evident (fig. 3).
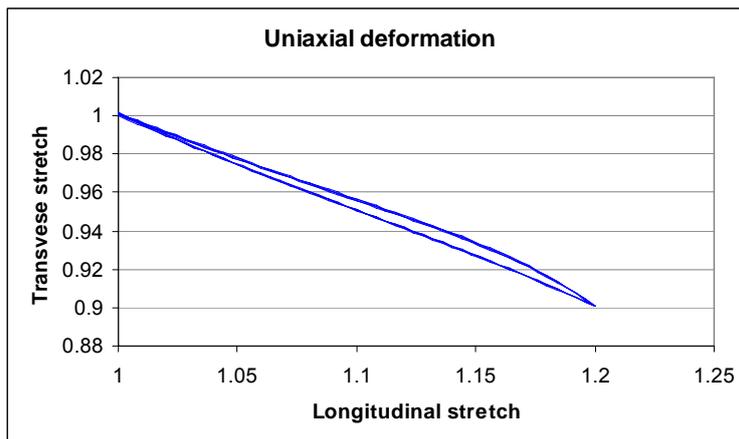

fig. 3 Transverse - longitudinal stretch diagram

A small hysteresis is present, whose extent remains constant during loading-unloading cycles.

3.2 Strain rate

The parametric study here reported pertains the parameters which are related to the non equilibrium stress, namely the material constants τ and β and the deformation period T, i.e. the frequency of the applied load $f = 1/T$. The effects of the elastic constants are not reported since they are assumed to produce analogous results as those provided by the parametric study performed in Chapter 3, which concerns a three dimensional anisotropic elastic model.

Fig. 4 shows how the model responds by varying the period of deformation T or, equivalently, the applied strain rate in a uniaxial tension testing. For graphical purposes the matrix relaxation times have been set equal to 50s.
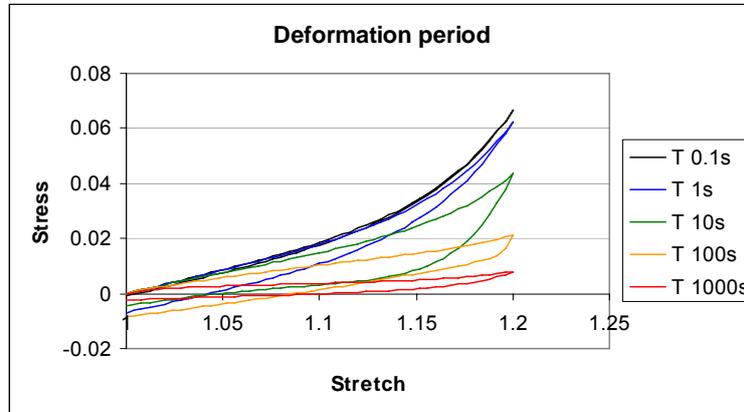

fig. 4 Stress-stretch plot. Effect of the deformation period.

The response of the model becomes purely elastic in the limit of high strain rates ($T <$ 1s). The longest period of deformation does not lead to a quasi-static simulation since an hysteresis loop is still present. The hysteresis value, which is a measure of the energy (per unit volume) dissipated in each cycle, increases when the simulation is performed at periods of deformation which are of the same order of magnitude of the characteristic relaxation times of the material. This is a feature of the rheological model chosen to describe the viscoelastic behaviour of the tissue. However it is desirable that the amount of hysteresis does not vary as much with the deformation period since soft biological tissues display a certain rate independence of hysteresis [2].

The effect of the matrix relaxation time is depicted in fig. 5. The decrease of τ_1 ($=\tau_2$) shifts downward the stress-stretch curves. Low values of τ_1 indeed cause the matrix to relax very quickly thus increasing the overall composite compliance, especially in the small strain regime.
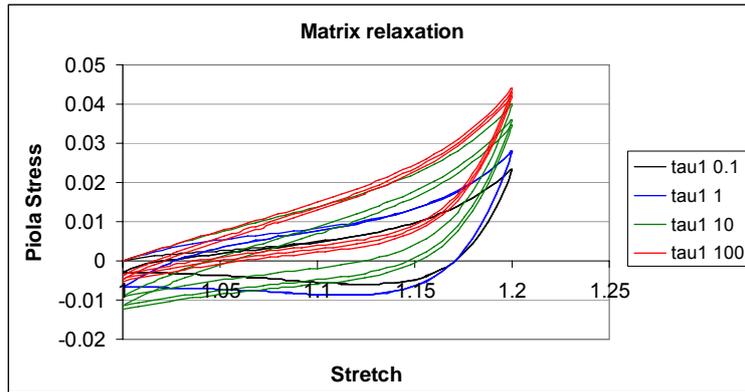
fig. 5 Stress-stretch plots. Effect of matrix relaxation time.

In all the cases, the completion of each load cycle does not lead to a stress free configuration: in order to restore a zero strain configuration, a compressive load is required. This means that the zero stress configuration does not coincide with the reference configuration, after the first cycle.

Even in the case of small τ a large hysteresis loop is evident. This effect probably arises from the viscoelastic behaviour of the collagen fibres. Moreover, the free energy factors have been set to large values, which cause the composite to be sensitive to the strain rate. Peak stress decay is virtually absent in the case of small τ values. It becomes more evident when the relaxation times approximate the period of the applied load, rather than for very larger τ values. The trend of the peak stress decay is depicted in the bar diagram below.
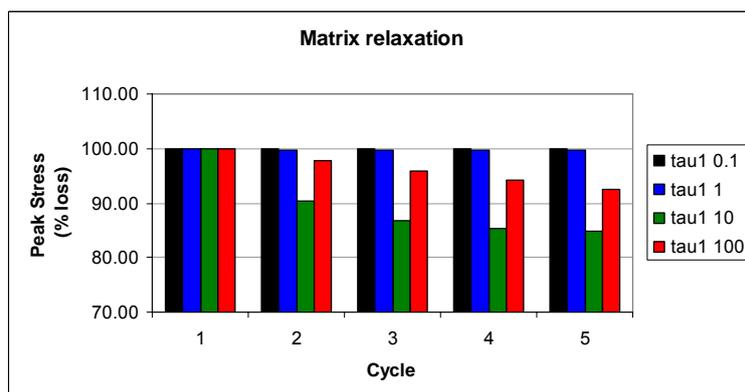

fig. 6 Percentage peak stress decay. Effect of matrix relaxation.

The stress loss is normalized with respect to the maximum value attained during the first loading ramp.

As previously stated, the free energy factors weigh the sensitivity of the constitutive model to the strain rate. In fact, equation 8 predicts a purely elastic behaviour by

127

setting β=0, while it models a viscous element for large values of β. The effects of varying the matrix free energy factor on the stress-stretch response is shown in fig. 1.
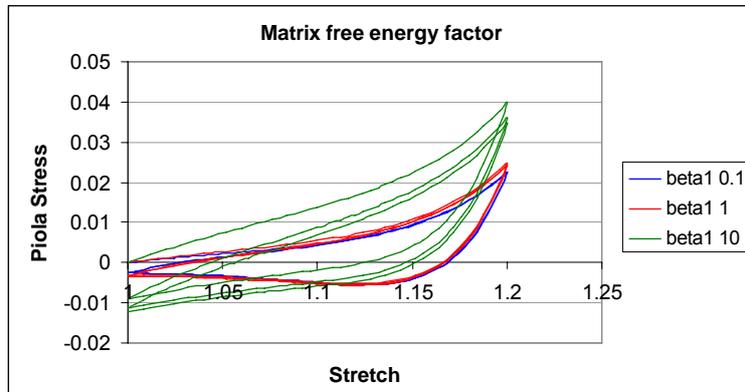

fig. 7 Stress-stretch plots. Effect of matrix free energy factor.

The increase of β stiffens the early mechanical response of the composite structure. The slope of the stress-stretch plot at large deformations, i.e. where the fibres begin to withstand load, is almost unchanged. Small values of the free energy factor (β<1) do not produce any dramatic change in both the hysteresis loop and peak stress loss, as depicted in fig. 8.
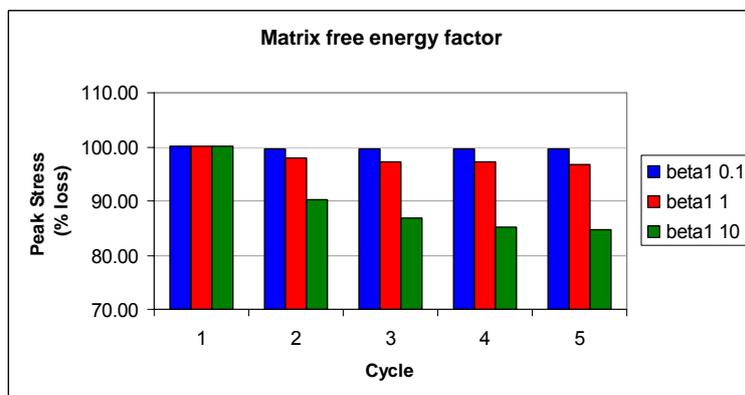

fig. 8 Percentage peak stress decay. Effect of matrix free energy factor.

The effects of varying the viscoelastic parameters of the fibrous reinforcement produces analogous results as those seen in the case of the matrix viscoelastic parameters. However the effects are located in the large strain regime. Thus changing fibres relaxation times has virtually no effects on the first early mechanical response. On the contrary, the stiffness of the composite at large deformations is significantly higher (fig. 9).
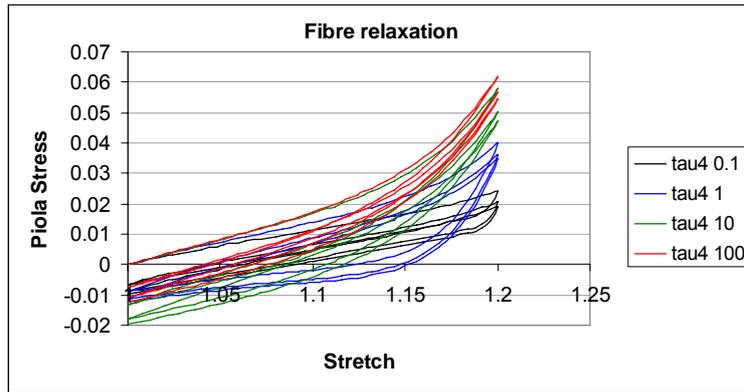
fig. 9 Stress-stretch plots. Effect of fibre relaxation time.

In a similar manner, small β values decrease the "viscous" contribution of the fibre to the total stress. On the other hand, large β values have an evident effect only at large deformations while the early mechanical response remains unchanged. In this case the viscoelastic behaviour is mainly caused by the matrix.
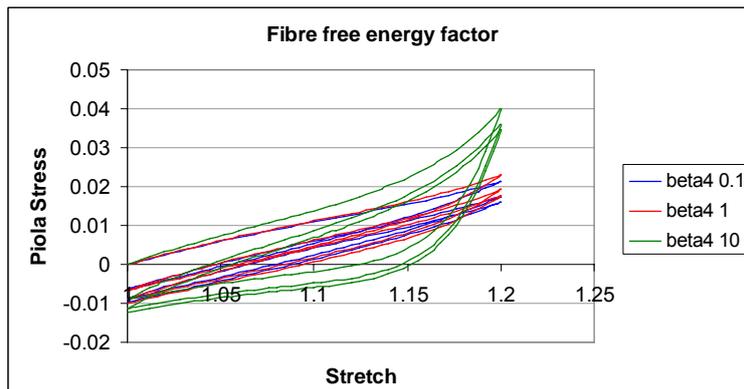

fig. 10 Stress-stretch plots. Effect of fibre free energy factor.

*3.3 Experimental data fitting*

The predictions of the model have been compared with data provided by testing native skin and trypsin treated skin. Details on the sample preparation and testing conditions is reported in Chapter 2. This comparison has been done in order to test the sensitivity of the model to the composition of the tissue. The set of material constants which best captures the actual mechanical response of native goat skin has been determined through a least square optimization performed with MATLAB software. The result of the optimization procedure, provides the following material parameters:

$$c_1 = 0.0078\,\text{MPa} \quad c_2 = 0\,\text{MPa}$$
$$k_1 = 0.0112\,\text{MPa} \quad k_2 = 17.62$$
$$\varphi_f = 0.15 \quad \vartheta = \frac{\pi}{9}$$
$$\tau_1 = 41.77\,\text{s} \quad \tau_4 = 2.44\,\text{s}$$
$$\beta_1 = 1.93 \quad \beta_4 = 0.96$$

The comparison between the experimental data and the model simulation is reported in the picture below.
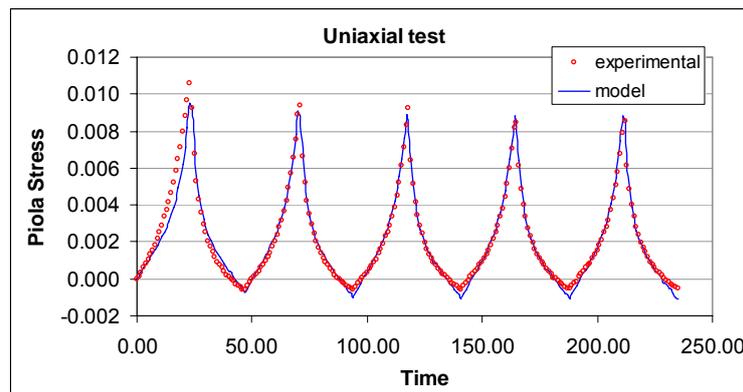
fig. 11 Stress - stretch plot. Goat skin untreated sample. Experimental and theoretical data

Time has been chosen as independent variable rather than the axial stretch for graphical purposes only. There is a good agreement between experimental data and model prediction. However the model overestimates tissue stiffness in compression. In the proximity of unloading-loading transition, the theoretical curve is always below the experimental one. This effect could be due to specimen instability. At large deformations, indeed, the tissue is irreversibly plasticized, which is evident from the residual permanent set after load removal. Since the length of the sample is much higher than the width and thickness, the sample is able to withstand compressive loads only up to a certain extent. Below this threshold value the sample buckles and the load cell records a small value of the compressive load. The model predicts instability of the fibres reinforcement, but not for the matrix, i.e. the matrix can withstand negative loads irrespective of any consideration of instability. This phenomenon is even more evident for trypsin treated goat skin samples. In this case the matrix has been severely damaged by the enzymatic treatment which causes the digestion of the interfibrillar matter. The removal of this material severely jeopardizes the ability of the tissue to elastically recover the initial configuration. This is clearly visible in the stress-strain plots with a steep load fall, immediately after load removal (see Chapter

2, fig. 14 and fig. 16 and related discussion). As a consequence of that, trypsin treated samples become instable sooner than the native untreated tissue.

To simulate this experiment, a new set of material constants has been evaluated through least square optimization using MATLAB software. The set of material constants which best approximate the mechanical response of trypsin treated goat skin samples is

$$c_1 = 0.0036\,\text{MPa} \quad c_2 = 0\,\text{MPa}$$
$$k_1 = 0.0077\,\text{MPa} \quad k_2 = 12.81$$

$$\varphi_f = 0.15 \quad \vartheta = \frac{\pi}{9}$$
$$\tau_1 = 35.3\,\text{s} \quad \tau_4 = 2.42\,\text{s}$$
$$\beta_1 = 2.38 \quad \beta_4 = 3.52$$

The prediction of the model with this particular set of material parameters produces the following diagram.
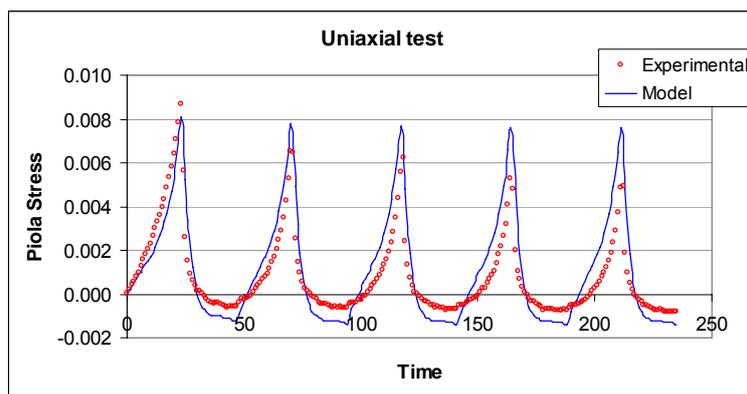
fig. 12 Stress - stretch plot. Goat skin trypsin treated sample Experimental and theoretical data.

The optimization procedure correctly supplies a lower starting modulus, as observed experimentally. As expected, the differences in the unloading-loading transition is even amplified in the comparison with trypsin treated samples. This model is not able to predict simultaneously sudden stress drop (after load removal) and large extent of matrix instability. In order to simulate the matrix instability phenomenon a solution could have been to increase the fibre volume fraction and/or decrement matrix elastic properties. The model can indeed predict fibres instability and this surely would have led to a better curve fitting, but with the major drawback of predicting non physical results concerning transverse contraction and thickness swelling, which is a feature already examined in Chapter 3.

4. Conclusions

An anisotropic viscoelastic constitutive model, of the state variable type, has been developed. It is applicable to soft tissues which display time-dependent mechanical behaviour, like skin, arteries, ligaments and tendons. The constitutive model has 12 constants, 4 related to long term equilibrium elastic response, 2 can be regarded as structural constants (fibre volume fraction and fibre direction), and the remaining 6 constants governs the non equilibrium stress. However not all the 12 parameters can be freely varied. Structural and elastic parameters have a microstructural basis and can be determined experimentally with independent tests. In this case such parameters are no longer empirical but reflect the underlying structure.

Regardless of any microstructural consideration, simulation of tissue deformation shows the ability of the model to predict viscoelastic mechanical behaviour of skin. Even though material constants have been used as fitting parameters, few constraints have been set up during best-fitting procedure. Matrix elastic constants cannot be orders of magnitude below fibre stiffness in order to avoid composite swelling in the thickness direction (see Section 4 of Chapter 3). Fibre volume fraction has been set equal to 30% which is a value provided by porosimetry testing performed on a bovine limed pelt, i.e. a dry collagenous reticulum almost devoid of cellular and interfibrillar component. Moreover it has been assumed the existence of just two families of fibres oriented at 20° with respect to the load axis. This of course could not be the actual case. As stated in Chapter 3 there exists an asymmetric continuous distribution of collagen fibres.

In summary, the anisotropic viscoelastic model successfully mimics skin mechanical behaviour at large deformation. However the model can be upgraded by introducing different relaxation times ($\alpha > 1$ in equation 2) and/or an altered viscous formulation. We believe that this model can produce even better results in the case of different motions such as confined compression and oscillatory shear, which do not cause specimen instability.

5. References

1. Mow V.C., Kuei S.C., Lai W.M., Armstrong C.G.: "Biphasic creep and stress relaxation of articular cartilage in compression: theory and experiments". *Journal of Biomechanical Engineering* **102**,73-84, 1980.

2. Fung Y.C.: Biomechanics: Mechanical properties of living tissues. *Ed. Springer* Chapter **7**, 242-320, 1993.

3. Holzapfel G.A.: "Nonlinear Solid Mechanics: A Continuum Approach for Engineering". *Wiley*, 2000.

4. Holzapfel G.A., Gasser T.C. and Stadler M.: "A structural model for viscoelastic behavior of arterial walls: Continuum formulation and finite element analysis". *European Journal of Mechanics A/Solids* **21**, 441-463, 2002.

5. Taylor R.L.: "FEAP - A Finite Element Analysis Program. Version 7.5, Theory Manual" University of California at Berkley Chapter **9**, 74-79, 2003.

6. Holzapfel G.A., Gasser T.C.: "A viscoelastic model for fiber-reinforced composites at finite strains: Continuum basis, computational aspects and applications". *Computer methods in applied mechanics and engineering* **190**, 4379–4403, 2001.

7. Billiar K.L. and Sacks M.S.: "Biaxial mechanical properties of the natural and glutaraldehyde treated aortic valve cusp — Part II: a structural constitutive model". *Journal of Biomechanical Engineering* **122**, 327–335, 2000.

Acknowledgements

This thesis would not have been possible without the generous contribution of many friends and colleagues.

I am sincerely and particularly indebted to my supervisor, professor Paolo A. Netti, for granting such a challenging project to me. I really hope I have not disappointed him. His sharp and detailed comments have constantly spurred my curiosity and have kept my thirst of knowledge alive. His outstanding and recognized expertise in the field made working for him a honour.

I am grateful to all my friends and colleagues at the Department of Materials and Production Engineering at the University of Naples. They have been ideal office and lab mates. Thanks to Dr. Carmen Palmiero, Dr Sabatino Fusco and Dr. Francesco Urciuolo for helping me with my experiments when they had certainly more interesting things to do.

I would like to thanks all my friends at the University of Northampton, Mrs Pat Potter, Mrs Tanya Hayes, Ms Sarah Lee, and all the very nice people I met at the British School of Leather Technology. I thank them for being friendly and patient with my annoying questions and requests.

I am grateful to prof. Tony Covington and prof. Geoffrey Attenburrow. With their amazing sharpness, technical dept and knowledge they provided me with valuable help and support.

A particular note of thankfulness to my friend Chris Barnard for teaching me the tricks of the trade of the arts of tanning. I hope I could partially repay his friendship by acknowledging him in this work.

I owe a special debt to Ms Mercedes Catalina, Dr Jeffry Guthrie-Strachan and his beautiful wife Dr Paula Antunes, for their immense support. They really helped me to feel like home and I will never forget them.

The person who had the greatest impact on my formation and consequently on this work is my fraternal friend Francesco Mollica. I do not think I will ever find enough words to thank him. He has been so generous, his knowledge so wide, his mind so sharp that anything I can say really does not do any fairness to his incommensurate support.

I thank my mother for tolerating me my bad mood when I was stressed and for putting in encouraging words when I felt down.

As I write these lines my mind goes to my girlfriend Anna Paola. Her absence when I was in England made me realize more than ever how much she means to me.